UNIVERSITÀ
DEGLI STUDI
DI PADOVA

Sede Amministrativa: Università degli Studi di Padova

Dipartimento di Fisica e Astronomia "Galileo Galilei"

SCUOLA DI DOTTORATO DI RICERCA IN: ASTRONOMIA
INDIRIZZO: UNICO
CICLO XXVII

# *HST* AND GROUND-BASED ANALYSIS OF MULTIPLE STELLAR POPULATIONS IN GLOBULAR CLUSTERS

**Direttore della scuola:** Ch.mo Prof. Giampaolo Piotto

**Supervisore:** Ch.mo Prof. Giampaolo Piotto
**Correlatore:** Dr. Antonino P. Milone

**Dottorando:** Domenico Nardiello

# *HST* AND GROUND-BASED ANALYSIS OF MULTIPLE STELLAR POPULATIONS IN GLOBULAR CLUSTERS

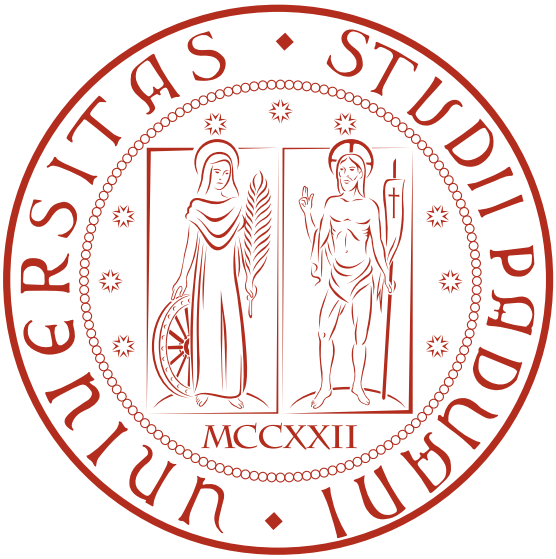


PHD THESIS

DIPARTIMENTO DI FISICA E ASTRONOMIA "G. GALILEI"
UNIVERSITÀ DEGLI STUDI DI PADOVA

**Direttore della scuola:** Ch.mo Prof. Giampaolo Piotto

**Supervisore:** Ch.mo Prof. Giampaolo Piotto
**Correlatore:** Dr. Antonino P. Milone

**Dottorando:** Domenico Nardiello

Domenico Nardiello: *HST and Ground-based analysis of multiple stellar populations in globular clusters*,
PhD Thesis, © July 2015

"Space is big. Really big. You just won't believe how vastly, hugely, mind-bogglingly big it is. I mean, you may think it's a long way down the street to the chemist, but that's just peanuts to space."

Douglas Adams, *The Hitchhiker's Guide to the Galaxy*

# Acknowledgments

I wish to warmly thank Antonino P. Milone, Giampaolo Piotto, Luigi, R. Bedin, Anna F. Marino, and Andrea Bellini without whom the results presented in this thesis would not have been possible.

Domenico

## ABSTRACT

In the last decades spectroscopic and photometric evidence has proven that globular clusters host multiple stellar populations characterized by different chemical abundances.

The aim of my thesis is to give a contribution in the analysis of multiple stellar populations in Galactic globular clusters, using observations collected both with ground-based telescopes and with the *Hubble Space Telescope*.

The first part of the thesis presents an overview regarding the topic of multiple stellar populations in Galactic globular clusters, from the first photometric and spectroscopic discoveries to the various theories developed to describe the formation and evolution of different stellar generations in a cluster.

Then a description of my work regarding multiple stellar populations in the globular clusters NGC 6121, NGC 6397, and NGC 6752 is given. Using ground-based FORS2@VLT observations of external regions of these three globular clusters, we identified multiple stellar populations in the main sequence of NGC 6121 and NGC 6752. This work has been possible thanks to high-precision photometry and appropriate combinations of colors and magnitudes. We presented the radial distribution of the two stellar populations hosted by each globular cluster, combining our result for the external regions with the fraction of first and second stellar generation measured in the central regions using *Hubble Space Telescope* data. Both for NGC 6121 and for NGC 6752, we found that the radial distribution of the number ratio of the blue main sequence to the red main sequence is almost flat inside $\sim$ 17 arcmin from the center of each cluster. Hydrodynamical and N-body simulations for the formation and evolution of multiple stellar populations predict that second generation stars form in the inner regions of the cluster and are initially more concentrated than first generation stars. The subsequent long-term dynamical evolution, driven by two-body relaxation, gradually erases the initial differences in the first and second generation spatial distributions; this is the reason why, for long relaxation-time systems (e.g. $\omega$ Cen), second generation stars are concentrated in the globular cluster in-

ner regions and retain some memory of the initial predicted spatial segregation. The relaxation-times of the globular clusters NGC 6121 and NGC 6752 are quite short (less then 1 Gyr), and therefore the two populations hosted by each cluster are today well-mixed, as demonstrated by their flat distribution.

In this work, we have also given an estimate of how much the second generation is enriched in helium with respect to the first generation, finding a mild ($\Delta Y \sim 0.02$) difference between the two sequences for both the clusters.

I am a Co-I of the *Hubble Space Telescope* Treasury programme "UV Legacy Survey of Galactic Globular Clusters: Shedding Light on Their Populations and Formation" (GO-13297, PI: G. Piotto). The second part of the thesis is based on this project. The aim of the *Hubble Space Telescope* treasury programme GO-13297 is the characterization and analysis of multiple stellar populations in a sample containing 56 globular clusters, using UV/blue and optical filters.

Using the *Hubble Space Telescope* treasury programme data, we analyzed the multiple stellar populations of the metal-rich globular cluster NGC 6352. The combination of UV/blue and optical observations has made possible to split and follow the two stellar populations across all the evolutionary sequences of all color-magnitude diagrams. We estimated the enrichment in helium of the second stellar generation, finding $\Delta Y \sim 0.03$. Moreover, we developed an innovative technique to put an upper limit on the relative age between the two stellar generations, with a careful discussion of the impact on relative age of all possible sources of uncertainty in the cluster parameters, such as the error on $\Delta Y$ or variations of metallicity and $\alpha$-enhancement. Considering all these uncertainties together, we found that the two stellar populations of NGC 6352 are coeval within $\sim 300$ Myr. This result will be useful to constraint theoretical models of formation and evolution of multiple stellar populations in globular clusters.

Finally, in the last part of the thesis, I summarize the results presented in this work and present a list of works that I would like to realize in future.

# RIASSUNTO

Negli ultimi decenni, prove spettroscopiche e fotometriche hanno dimostrato che gli ammassi globulari ospitano popolazioni stellari multiple caratterizzate da abbondanze chimiche differenti.

Lo scopo della mia tesi è dare un contributo nell'analisi delle popolazioni stellari multiple negli ammassi globulari della nostra Galassia, usando osservazioni acquisite sia con telescopi da terra che con l'*Hubble Space Telescope*.

La prima parte della tesi è una panoramica sul tema delle popolazioni stellari multiple negli ammassi globulari galattici, dalle prime scoperte fotometriche e spettroscopiche alle varie teorie sviluppate per descrivere la formazione ed l'evoluzione delle differenti generazioni stellari in un ammasso.

In seguito, viene data una descrizione del mio lavoro sulle popolazioni stellari multiple negli ammassi globulari NGC 6121, NGC 6397 e NGC 6752. Usando le osservazioni da terra effettuate con FORS2@VLT delle regioni esterne di questi tre ammassi globulari, abbiamo identificato popolazioni stellari multiple nella sequenza principale di NGC 6121 e NGC 6752. Questo lavoro è stato possible grazie a fotometria di alta precisione e combinazioni appropriate di colori e magnitudini. Abbiamo mostrato la distribuzione radiale delle due popolazioni stellari ospitate da ciascuno ammasso globulare, combinando il nostro risultato per le regioni esterne con la frazione di stelle di prima e seconda generazione misurate nelle regioni centrali con i dati dell'*Hubble Space Telescope*. Per entrambi gli ammassi NGC 6121 e NGC 6752, abbiamo trovato che la distribuzione radiale dei rapporti fra il numero di stelle nella sequenza principale blu e in quella rossa è abbastanza piatta entro $\sim$17 arcmin dal centro di ogni ammasso. Simulazioni idrodinamiche e a N-corpi riguardanti la formazione ed evoluzione delle popolazioni stellari multiple, predicono che le stelle di seconda generazione si formano nelle regioni interne dell'ammasso e sono inizialmente più concentrate rispetto alla prima generazione. La successiva evoluzione dinamica a lungo termine, guidata dal rilassamento a due corpi, cancella gradualmente le differenze iniziali tra le distribuzioni spaziali della prima e seconda generazio-

ne; questa è la ragione per cui, in sistemi caratterizzati da tempi di rilassamento lunghi (per esempio $\omega$ Cen), le stelle di seconda generazione sono concentrate nelle regioni interne e conservano la memoria della segregazione spaziale iniziale predetta. I tempi di rilassamento degli ammassi globulari NGC 6121 e NGC 6752 sono abbastanza corti (meno di 1 Gyr), e perciò le due popolazioni ospitate da ogni ammasso sono oggi ben mescolate, come dimostrato dalla loro distribuzione spaziale piatta.

In questo lavoro, diamo anche una stima di quanto la seconda generazione è arricchita in elio rispetto alla prima generazione, trovando una leggera differenza ($\Delta Y \sim 0.02$) tra le due sequenze per entrambi gli ammassi.

Io sono uno dei Co-I del programma Treasury dell'*Hubble Space Telescope* "UV Legacy Survey of Galactic Globular Clusters: Shedding Light on Their Populations and Formation" (GO-13297, PI: G. Piotto). La seconda parte della tesi è basata su questo progetto. Lo scopo del programma Treasury GO-13297 dell'*Hubble Space Telescope* è la caratterizzazione e analisi di popolazioni stellari multiple in un campione contenente 56 ammassi globulari, usando filtri UV/blu e ottici.

Sfruttando i dati del programma Treasury dell'*Hubble Space Telescope*, abbiamo analizzato le popolazioni stellari multiple dell'ammasso globulare, caratterizzato da alta metallicità, NGC 6352. La combinazione di osservazioni UV/blu e ottiche ha reso possibile individuare e seguire le due popolazioni stellari lungo tutte le sequenze evolutive dei diagrammi colore-magnitudine. Abbiamo stimato l'arricchimento in elio della seconda generazione, trovando $\Delta Y \sim 0.03$. Inoltre, abbiamo sviluppato una tecnica innovativa per porre un limite superiore sull'età relativa tra le due generazioni stellari, considerando attentamente l'impatto sull'età relativa di tutte le possibili sorgenti di incertezza nei parametri dell'ammasso, come l'errore su $\Delta Y$ o le variazioni di metallicità e $\alpha$-enhancement. Considerando tutte queste incertezze insieme, abbiamo trovato che le popolazioni stellari si NGC 6352 sono coeve entro $\sim 300$ Myr. Questo risultato sarà utile per vincolare i modelli teorici di formazione ed evoluzione di popolazioni stellari multiple negli ammassi globulari.

Infine, nell'ultima parte della tesi, riassumo i risultati presentati in questo lavoro e presento una lista di lavori che vorrei realizzare in futuro.

# CONTENTS

# 1

# MULTIPLE STELLAR POPULATIONS IN GLOBULAR CLUSTERS

Up to the end of XX century, astronomers thought they knew everything about the formation and evolution of globular clusters in the early Universe. The recent discoveries of multiple stellar populations has changed the way of seeing the globular cluster as "simple stellar population" formed in a single burst. In this Chapter, we describe how the discovery of multiple stellar populations has revitalized the interest of the astronomers on the globular clusters.

## 1.1 INTRODUCTION

Globular clusters (GCs) represent an ideal laboratory to understand stellar formation and evolution, and chemical enrichment in the primordial Universe, and, for this reason, these objects are a reference point in cosmologic and stellar evolution theories. With an age up to about 13.5 Gyr, only $\sim$ 300 Myr less than the present estimate for the age of the Universe, GCs are the oldest objects in the Milky Way that we can date. They are the principal component of galactic halos and bulges, and their stellar population properties are the basis of synthetic models, useful for interpreting the light from distant galaxies, for which it is not possible to resolve the stars.

Until not so long ago, astronomers considered GCs as the perfect example of "simple stellar population" (Renzini & Buzzoni 1986), i.e., a group of stars at the same distance, born from the same burst, and having the same chemical composition, although spectroscopic observations of individual stars hosted by a GC showed anomalies in the abundances of some elements (see discussion in Gratton, Sneden & Carretta 2004). While, on average, in many GCs the stars do not show metallicity variations, they often exhibit large anti-correlations between the abundances of C and N, Na and O, and Mg and Al. These anti-correlations

are due to the presence at the stellar surfaces of material which have undergone H burning at temperatures of a few ten millions K (Prantzos, Charbonnel & Iliadis 2007).

Moreover, in sixties, Sandage & Wildey (1967) and van den Bergh (1967) have already demonstrated that some GCs showed anomalous horizontal branch (HB) in their color-magnitude diagrams (CMDs). This problem, usually known as the *second parameter* problem, tell us that the HB morphology of some GCs is not only driven by the metallicity, but that at least another parameter affects the morphology of the HB.

With the end of the second millennium, we had the first real photometric confirmation of the presence of multiple stellar populations in GCs, in particular in the peculiar GC $\omega$ Centauri. However, for many years, it was a common perception that not all the Galactic GCs hosted more than one population, also thanks to some works, such as that by Richer et al. (2008). The spectacular CMD of NGC 6397 they obtained using data collected with the Advanced Camera for Surveys (ACS) of the *Hubble Space Telescope* (*HST*), reveals an extremely tight main sequence (MS) in the $m_{\rm F606W} - m_{F814W}$ color system, leading to the conclusion that this cluster contained a single stellar population (but this result will be refuted later by Milone et al. 2012a, as we will explain in the next sections).

In this Chapter we describe the birth and evolution of the idea of multiple stellar population (MSP), from the beginning, including the most striking discovery of multiple populations in the MS of $\omega$ Centauri, to the recent discoveries both with ground-based and *HST* data. We will briefly present the different theories developed to explain the formation and evolution of MSPs in GCs.

## 1.2 CHEMICAL EVIDENCE OF MULTIPLE STELLAR POPULATIONS

Excluding some exceptions, e.g. $\omega$ Centauri, M 2, M 22, M 54, Terzan 5, NGC 1851 and NGC 5824, all the Galactic GCs show negligible spread in metallicity distribution, i.e. all the stars in a GC have almost the same metallicity. In the case that a GC was formed by a single population, whose stars were born from the same medium, it is expected that all the stars have almost the same chemical properties. Indeed, the stars of all the Galactic GCs show peculiar chemical

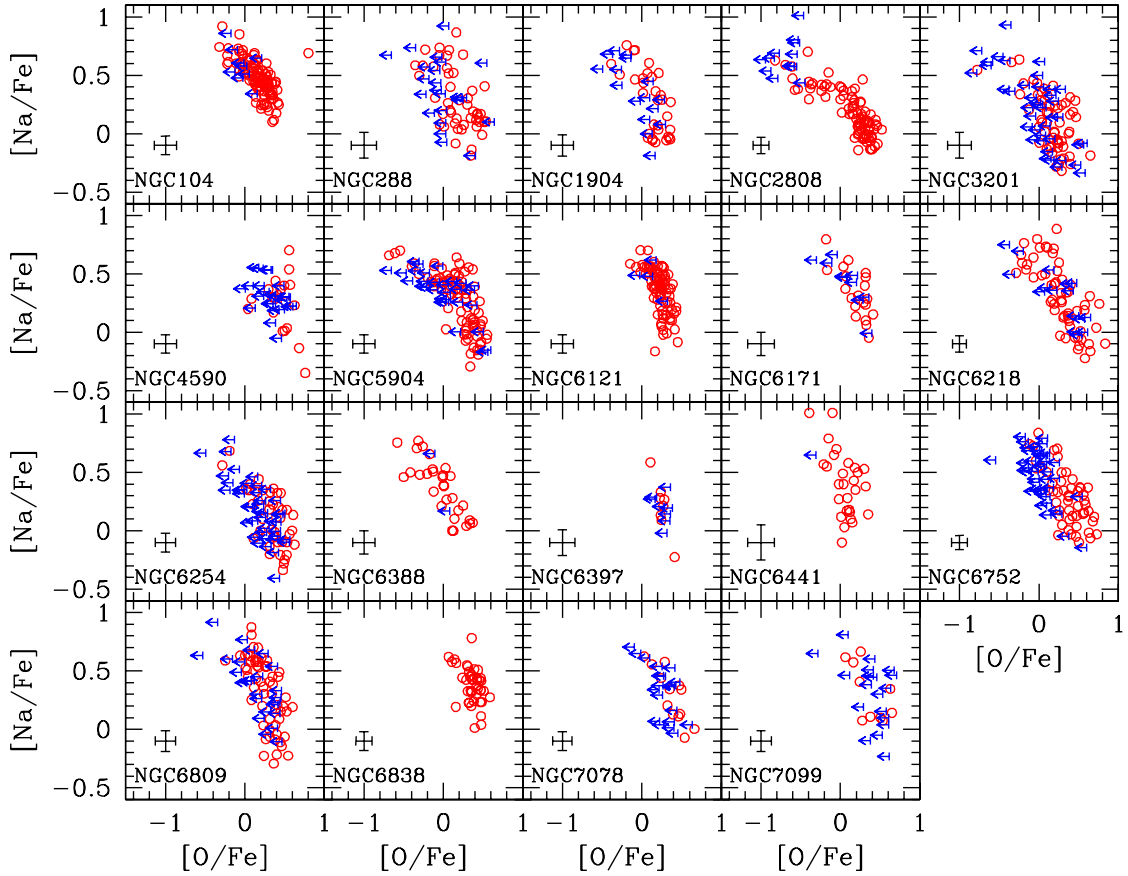


Figure 1: The Na-O anticorrelation patterns observed in 19 GCs by Carretta et al. (2009b)

abundance variations of some specific elements. This was already observed in 1970s and 1980s: many spectroscopic works showed the presence of red giant branch (RGB) stars having strong CN bands (Osborn 1971), in contrast with the stars of the field characterized by weak CN bands; moreover in some GCs a bi-modal distribution of CN strength and anti-correlations between CH and CN strengths was discovered (see for example Norris et al. 1981; Norris 1981; Smith & Norris 1982). Other spectroscopic observations brought to the discovery of other peculiar chemical anomalies, as, for example, the large spread in the sodium distribution among stars in M 3 and M 13 found by Cohen (1978). With the advent of high resolution spectra, other anomalies have surfaced, such as light element variations among the GC stars and well defined chemical pattern, such as the anti-correlations Na-O, C-N, and Mg-Al (see Gratton, Sneden & Carretta 2004; Gratton, Carretta & Bragaglia 2012 for a review).

These anti-correlations patterns are different for different GCs and could have different extensions, as shown in Fig. 1 for a sample of 19 GCs (Carretta et al. 2009b). The anti-correlations are the proof that in the stellar surfaces of a fraction of the GC stars is present material which have undergone H burning at temperature of a few ten millions K (Prantzos, Charbonnel & Iliadis 2007; less for the C-N anticorrelation).

While the variations of C and N are observed also in field giant stars and are expected from typical evolution of low mass stars (Sweigart & Mengel 1979), the variations of the other light elements are an exclusive peculiarity of the GCs stars. Moreover, the fact that anti-correlations Na-O have not only been observed for giant stars, but also in the unevolved or slightly evolved stars of some GCs, such NGC 6397, NGC 6752, or 47 Tuc (Gratton et al. 2001; Carretta et al. 2004, 2005; Lind et al. 2011), means that this chemical anomalies were already present in the material out of which the stars formed, because low mass stars are not hot enough to produce this material. Moreover, the fact that the total C+N+O abundance is constant within the errors for almost all the GCs, means that the material out of which the other stellar generations formed has been processed through the hot CNO cycle.

Another chemical peculiarity regarding multiple stellar generations is associated to the helium abundance. While the Na-poor, O-rich population is characterized by primordial helium abundance, the other populations are enhanced in helium. The explanation is simple: helium is the main product of H-burning, and is released in the medium, from which other stellar populations formed, by the stars that product also light-elements anomalies. Many photometric and spectroscopic works have confirmed the He variations (see, e.g., Villanova, Piotto & Gratton 2009; Dupree, Strader & Smith 2011; Pasquini et al. 2011; Milone et al. 2012d,a, 2013; Marino et al. 2014a), that could vary from $\Delta Y \sim 0.01$ dex to $\Delta Y \sim 0.15$ in the extreme cases.

The cause of the pollution of the material from which the other stellar generations formed has not been firmly identified yet. Many polluters have been proposed in the last decades, such as, for example, intermediate-mass asymptotic giant branch (AGB) stars (D'Antona et al. 2002), fast rotating massive stars (Decressin et al. 2007), and interactive massive binary stars (de Mink et al. 2009; Vanbeveren, Mennekens & De Greve 2012). The associated scenarios for the for-

mation and evolution of multiple stellar populations in GCs will be discussed in the section 1.5.

## 1.3 PHOTOMETRIC DISCOVERIES OF MULTIPLE STELLAR POPULATIONS

About a decade ago, the idea of GC as simple stellar population has been definitely wiped out by the discovery of multiple evolutionary sequences in the CMD of $\omega$ Centauri (Lee et al. 1999; Bedin et al. 2004). The first photometric evidence of MSPs in a GC was provided by Lee et al. (1999), from their discovery of the discrete nature of the RGBs in $\omega$ Centauri. The first evidence of MSPs in the unevolved sequence of $\omega$ Centauri was given by Bedin et al. (2004); they found that, 2/3 magnitudes below the turn-off, the MS of $\omega$ Centauri splits in two. Indeed, Jay Anderson, in his PhD Thesis (Anderson 1998), already found a first evidence of MS split in $\omega$ Centauri, but his CMD was based on only one external *HST* Wide-Field Planetary Camera 2 (WFPC2) field, and, because this result was unexpected, he decided to wait more accurate photometry to be sure of the MS split.

Now we know that the MS of $\omega$ Cen is composed by six or more stellar populations (Bellini et al. 2010), characterized by different metallicity. Indeed, the most "strange" discovery concerning the MSPs in $\omega$ Centauri, came from spectroscopic observations, that showed that the bluer MS has twice the metal abundance of the redder (and dominant) MS (Piotto et al. 2005). This combination of color and metallicity could be obtained only if we consider the bluer component extremely enriched in helium ($Y \sim 0.38$) relative to the dominant old-population, characterized by primordial helium. Indeed, the scenario of the peculiar GC $\omega$ Centauri is more complex: the multiple MSs spread in multiple sub giant branches (SGBs) and RGBs (see Fig. 2), characterized by different metallicities and ages (Sollima et al. 2005; Villanova et al. 2007; Bellini et al. 2010).

The case of $\omega$ Centauri has revitalized the interest on the globular clusters and stimulated a large number of investigations, both photometric and spectroscopic, that have shown that multiple population phenomenon is not a peculiarity of a single object. The second object that showed MSPs was NGC 2808. While spectroscopic measurements of red giants of this GC showed that these stars have nearly uniform iron content (Carretta et al. 2006), Piotto et al. (2007)

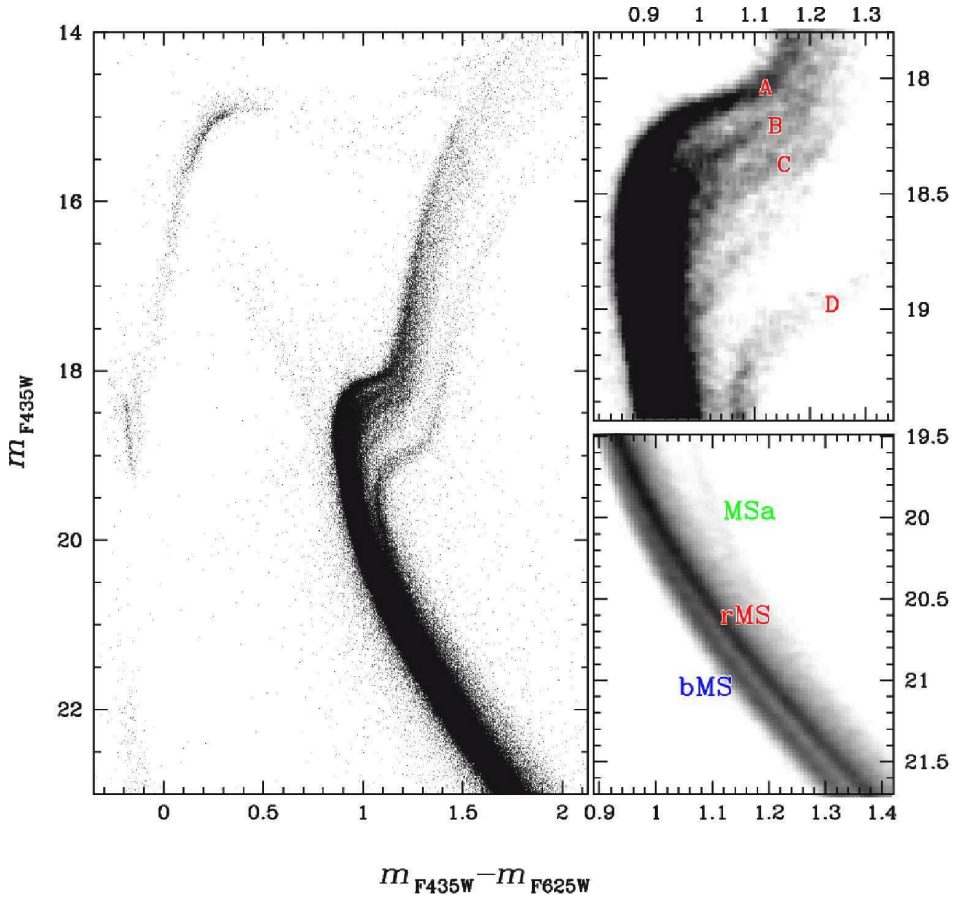


Figure 2: Left panel: $m_{F435W}$ versus $m_{F435W} - m_{F625W}$ CMD showing the complexity of $\omega$ Cen; right panels: Hess diagrams to highlight the four main SGBs (top) and the three MSs (bottom, from Bellini et al. 2010 )

found that the MS of NGC 2808 splits in three discrete components (see Fig. 3), characterized by different helium content ($Y \sim 0.248$, 0.31, 0.38). The Helium enhancement has also been demonstrated by direct spectroscopic observations of helium-rich stars along the RGB and the HB (Pasquini et al. 2011; Marino et al. 2014a). Other peculiarities suggest that NGC 2808 hosts multiple populations. For example, the HB is greatly extended blue-ward, well populated to both the blue and red of the instability strip (Dalessandro et al. 2011), and the distribution of stars is multimodal (Sosin et al. 1997; Bedin et al. 2000). The multi-modality of the RGB has also been demonstrated both with photometric (Lee et al. 2009a; Monelli et al. 2013) and spectroscopic investigations. The latest has shown star-to-star variations of large number of light elements, Na-O anticorrelation pattern (Norris et al. 1981; Carretta et al. 2006; Gratton et al. 2011; Marino et al. 2014a; Carretta 2014), and three distinct groups of O-normal, O-poor and super-O-poor stars.

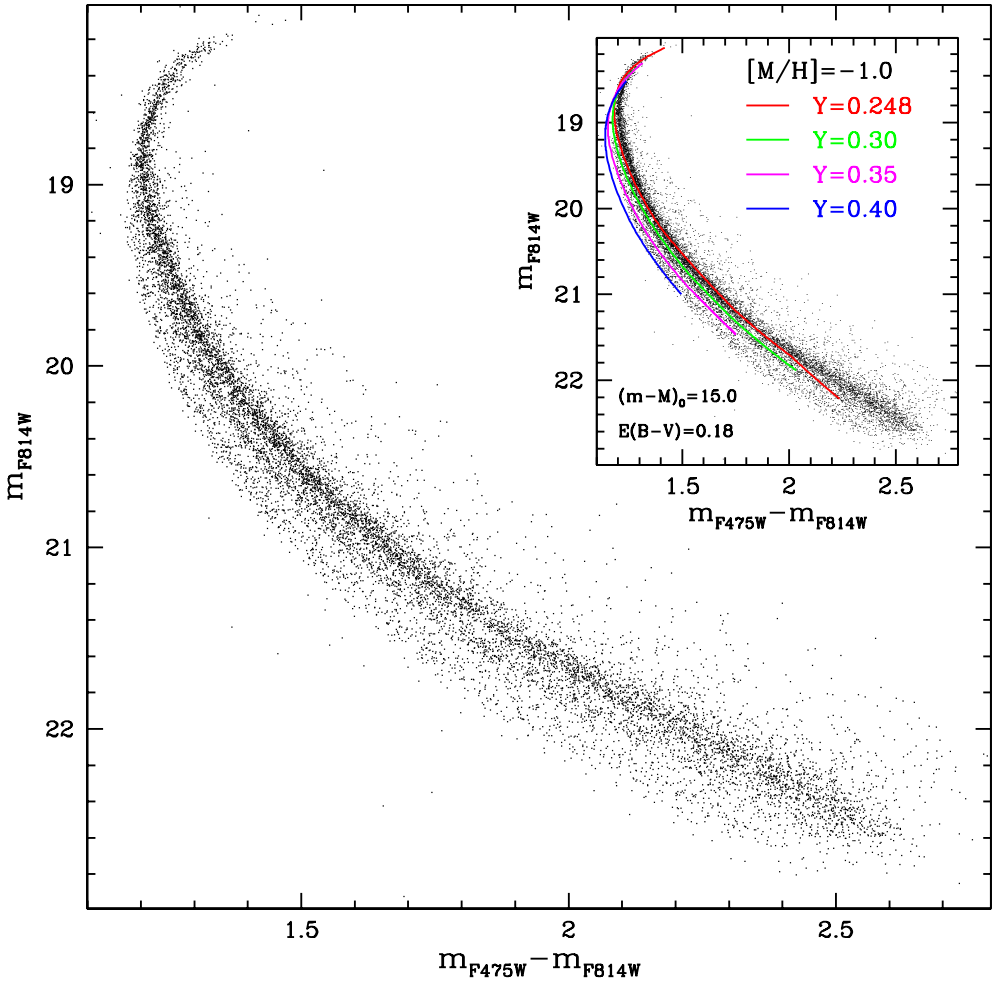


Figure 3: The triple MS of NGC 2808 in the $m_{\mathrm{F814W}}$ versus $m_{\mathrm{F475W}} - m_{\mathrm{F814W}}$ CMD (from Piotto et al. 2007)

Another Galactic GC that showed anomalies due to the presence of MSPs is NGC 1851. This is one of the most interesting cluster with multiple stellar populations. I also presents small star-to-star abundance dispersion for iron-peak and neutron-capture elements. The first important photometric discovery of MSPs in this GC came from the work by Milone et al. (2008), that showed the split of the SGB in two components in the $m_{\mathrm{F606W}} - m_{F814W}$ color-system (see Fig. 4). It was hypothesized that this split could be due to a difference in age of $\sim 1$ Gyr between the two populations, or, as an alternative, the two SGBs could be nearly coeval but with a different C+N+O content (Cassisi et al. 2008; Ventura et al. 2009). Recently, it has been demonstrated that there is a large spread in C+N+O abundance sum among RGB stars (Yong, Grundahl & Norris 2015,

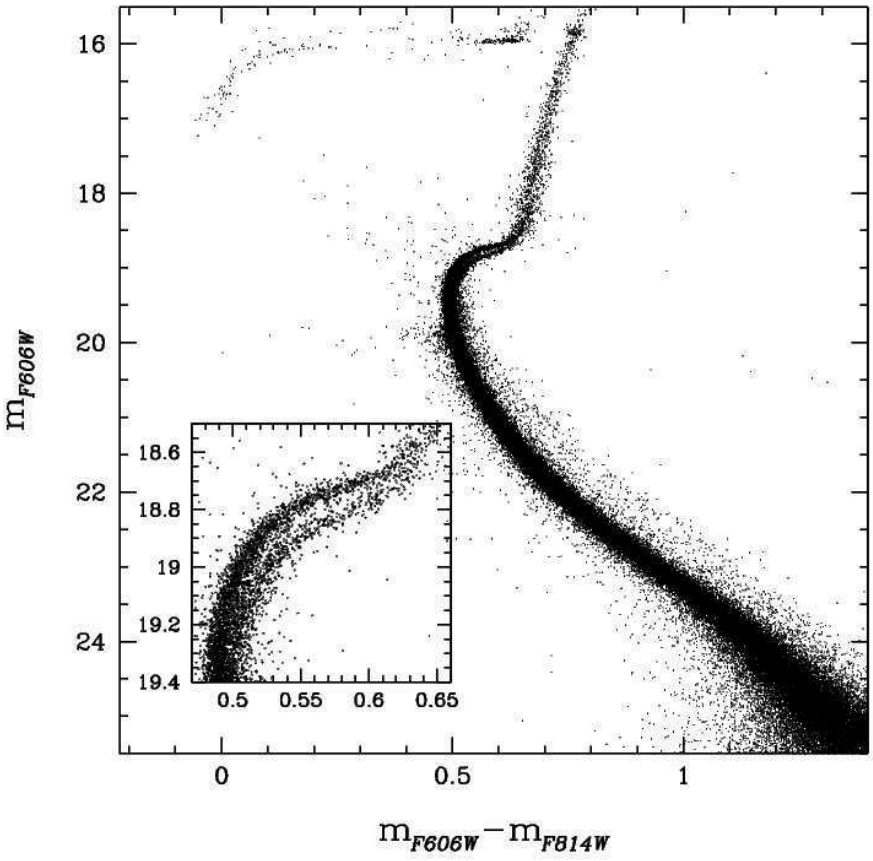


Figure 4: The $m_{\rm F606W}$ versus $m_{\rm F606W} - m_{\rm F814W}$ CMD of NGC 1851. The inset show a zoom around the double SGB (from Milone et al. 2009b).

and references therein). These observations confirm that the SGB split is mainly due to the difference in the C+N+O abundance between the two populations, by making this cluster unique. Moreover, spectroscopic observations of the stars in NGC 1851 have revealed the Na-O anticorrelation pattern (Villanova, Geisler & Piotto 2010), typical of GCs with MSPs.

The split of the SGB in optical bands is a common feature to few GCs. In addition to NGC 1851, also NGC 6388 and NGC 6441 (Bellini et al. 2013a), 47 Tuc (Milone et al. 2012d), NGC 362, NGC 5286, NGC 6656, NGC 6715, and NGC 7089 (Piotto et al. 2012) show multiple SGBs in optical bands (see Fig. 5 from Piotto et al. 2012). This peculiarity is consistent both with the presence of populations with different age, and with a significant difference in the C+N+O abundance of the populations.

After the case of NGC 1851, many other investigations have been performed to search for multiple populations in GCs, using both *HST* (see for

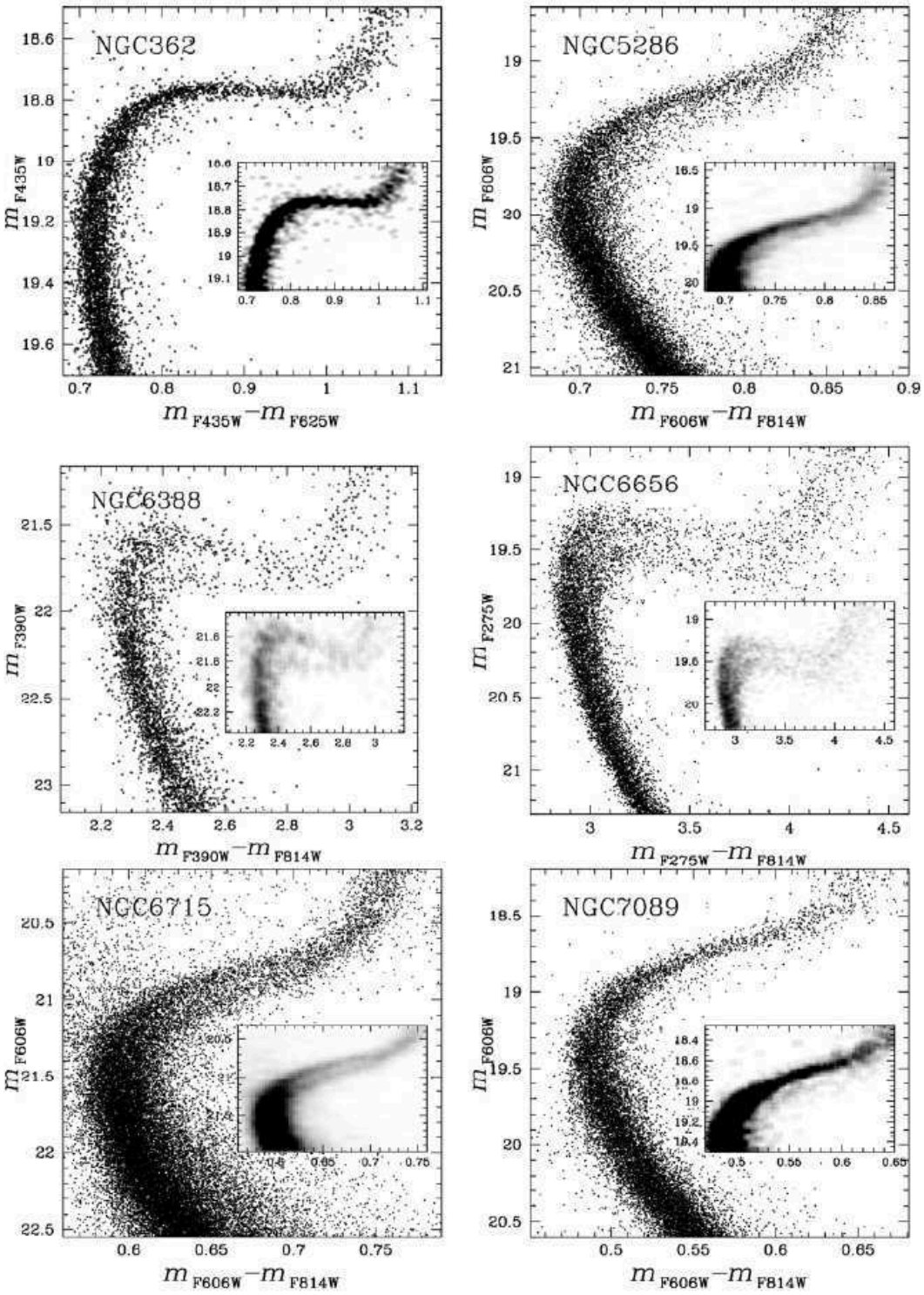


Figure 5: The $m_{F606W}$ versus $m_{F606W} - m_{F814W}$ CMD of NGC 362, NGC 5286, NGC 6388, NGC 6656, NGC 6715, and NGC 7089 (from Piotto et al. 2012).

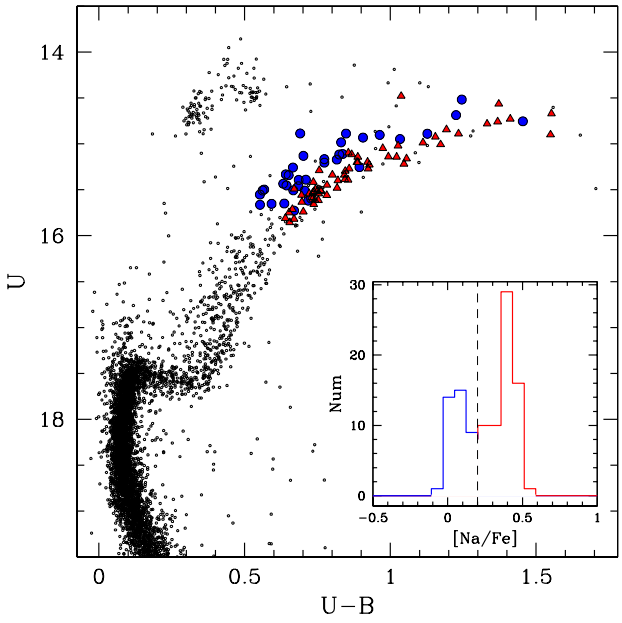


Figure 6: The $U$ versus $(U-B)$ CMD of NGC 6121 from WFI photometry. In the inset there is the distribution of the Na content from the UVES@VLT stellar spectra.The stars belonging to the two different Na groups are represented in two different colors: the red triangles represent the stars with [Na/Fe]$\leq$0.2 dex,and the blue circles the stars with [Na/Fe]$<$0.2 dex (from Marino et al. 2008).

example the cases of NGC 6397, Milone et al. 2012a, or the case of NGC 6752, Milone et al. 2013) and ground-based observations (Bellini et al. 2009b) . The work by Monelli et al. (2013), based on ground-based data, is the first evidence that a large sample of GCs in our Galaxy are formed by many stellar populations. Moreover, for a given GC, photometric results reflect the spectroscopic results and vice versa. An example is shown in Fig. 6, from the work by Marino et al. (2008): it shows the $U$ versus $(U-B)$ CMD of M 4. The blue and red the stars belong to two different groups of stars having [Na/Fe]$\leq$0.2 dex and [Na/Fe]$<$0.2 dex, respectively, as shown in the inset. These two groups of stars also form two different RGBs, and in particular, bluer stars are Na-poor (and O-rich), while redder stars are Na-rich (O-poor).

Thanks to UV/blue *HST* observations from the GO 13297 (see Piotto et al. 2015 for details), we know that all the GCs are composed by multiple stellar populations. There are some exceptions (even if higher precision data is

needed for a confirmation): Rup 106, as demonstrated by Villanova et al. (2013), and IC 4499 as shown by Walker et al. (2011).

All the GCs with MSPs appear to be homogeneous in iron, with some exceptions, i.e., NGC 7089 (M 2), $\omega$ Centauri, M 22, Terzan 5, M 54, NGC 5824, and NGC 1851 (Norris & Da Costa 1995; Da Costa et al. 2009; Ferraro et al. 2009; Marino et al. 2009; Carretta et al. 2010a,b; Johnson & Pilachowski 2010; Marino et al. 2011a,b; Da Costa, Held & Saviane 2014; Yong et al. 2014; Marino et al. 2014b). These 'anomalous' GCs, probably, have been a different formation history respect to the 'normal' GCs, because Supernovae (SNe) must have played a role in the internal chemical-enrichment history.

## 1.4 CHEMICAL ANOMALIES AND MULTIPLE SEQUENCES

As already shown in section 1.3, there is a connection between the chemical pattern observed with spectroscopic data and the presence of multiple sequences in the CMDs of Galactic GCs. Many recent works (e.g., Sbordone et al. 2011; Milone et al. 2012d) based on synthetic spectra, have demonstrated how the observed chemical anomalies translate in the photometric results.

Figure 7, from the work by Milone et al. (2012d), shows why the UV and blue photometric bands are most affected by the light-elements variations. In the upper panel there are the synthetic spectra of a star having primordial chemical abundances (in green) and belonging the MSa of 47 Tuc, and of a C- and O-poor, Na- and N-rich star (in magenta) belonging the MSb of 47 Tuc. In the middle panel there are the difference between the two synthetic spectra, while in the bottom panel the response of HST filters. In the figure it is possible to observe that color and magnitude changes are largest when UV and blue filters are used ($\lambda < 4500$ Å).

The combination of $BVI$ filters is useful to split the MS when along the GC stars there is a variation in helium (see, e.g., the case of NGC 2808 in Piotto et al. 2007), but optical filters are not affected by light-element variations. Instead, a variation of the sum of C+N+O-abundance permits to split the SGB using optical filters (see, e.g., the case of NGC 1851 in Milone et al. 2008).

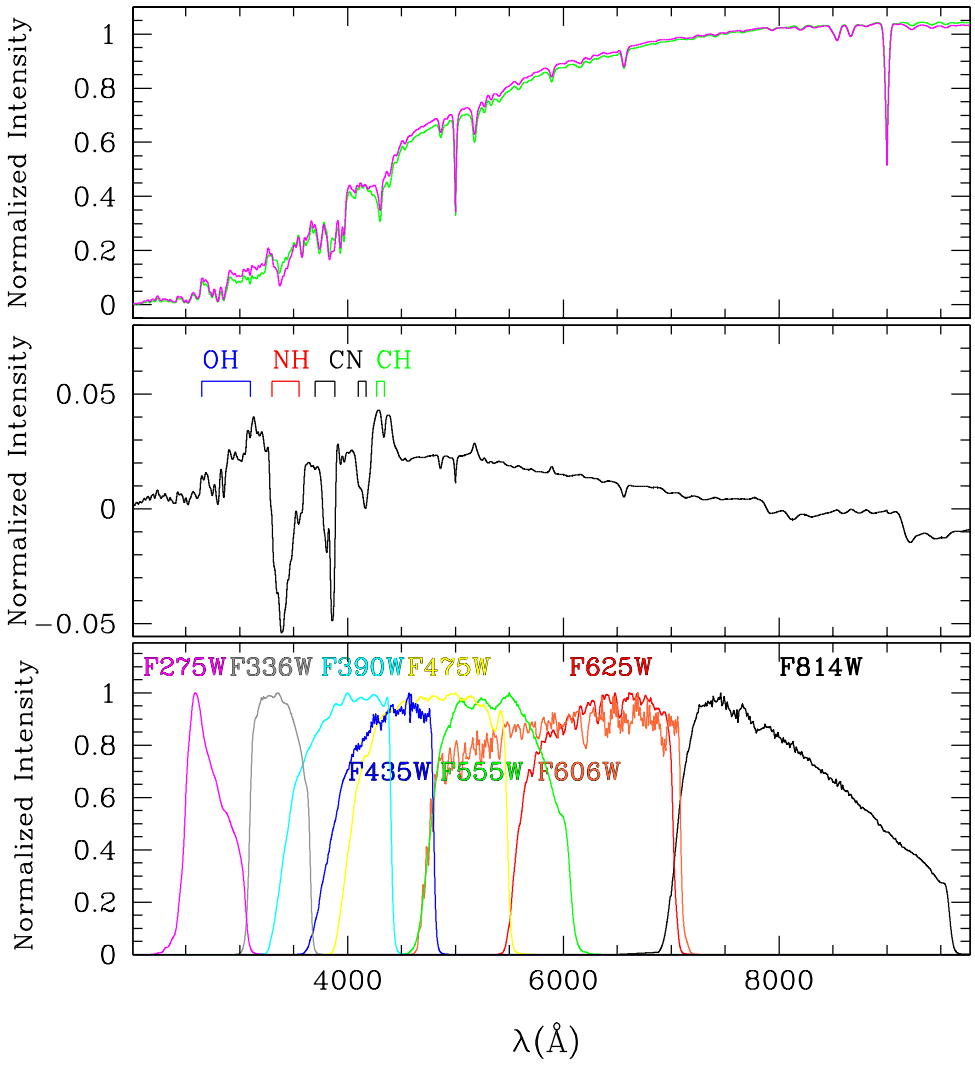


Figure 7: Top panel: synthetic spectra of two stars belonging the MSa (green) and MSb (magenta) of 47 Tuc. Middle panel: difference between the two spectra shown in top panel. Bottom panel: normalized responses of the HST filters (from Milone et al. 2012d).

The combination of UV/blue and optical filters is the perfect choice to photometrically disentangle the MSPs of GCs, as it will be demonstrated in Section 1.7.

## 1.5 MECHANISM OF MSPS FORMATION

The idea that GCs are formed by a first generation (FG) of stars, with composition similar to the proto-galactic interstellar matter, and a second generation (SG) of stars (or more stellar generations), characterized by C- and O- poor, N- and Na-rich, and He enriched stars, is well established in the astronomical community. This chemical pattern indicates that material out of which GCs formed was exposed to proton-capture processes at high temperatures and must have come from relatively massive FG stars.

In 'normal' GCs, SG stars have on average the same abundances of iron and other heavy-elements as the FG stars, indicating that SN ejecta are not the responsible of the pollution of material which SG stars formed from. The material come entirely from the stars belonging the first stellar generation, or it is a mixture of processed gas and pristine matter of the initial star forming cloud. Some 'normal' GCs exhibit small iron abundance spreads, indicating that only a tiny fraction of the SN products from FG were incorporated in SG stars (Renzini 2013).

Usually, the fraction of SG stars is higher than that of the FG (D'Antona & Caloi 2008). For this reason, the initial stellar population must have been larger than the stellar content of today's GCs, in such a way that FG stars produce enough CNO material to form SG stars. The lower fraction of FG stars could be due to dynamic loss in the early evolutionary phases (D'Ercole et al. 2008) or to the formation of the GC within a larger stellar environment, such as a dwarf galaxy, where the polluting matter is supplied by the surrounding stars (Bekki & Norris 2006).

In these last years, different theories have been developed to explain the mechanism of formation and evolution of MSPs in GCs. All these theories are based on the existence of a progenitor responsible of the pollution of the matter from which the SG formed. An important constraint on the progenitors is given by the fact that in almost all the observed GCs the C+N+O abundance is

constant within the errors, and therefore the progenitors must activate hot CNO cycle and not the He-burning phase.

Different progenitors for the SG stars have been proposed. The most accredited scenarios expect that the material from which SG stars formed comes from intermediate-mass asymptotic giant branch stars (AGB-M model, D'Antona et al. 2002; D'Ercole et al. 2008), fast-rotating massive stars (FRMS model, Decressin et al. 2007), massive interacting binary stars (de Mink et al. 2009; Vanbeveren, Mennekens & De Greve 2012), or super-massive stars (Denissenkov & Hartwick 2014; Denissenkov et al. 2015).

### 1.5.1 *Intermediate-mass asymptotic giant branch stars*

The **AGB-M** scenario is the model that presents fewer problems to explain the presence of multiple populations; indeed, already in 1980s, AGB stars were proposed as a possible cause of the observed chemical anomalies (D'Antona, Gratton & Chieffi 1983). In intermediate AGB stars, the H burning shell can extend into the convective envelope, contaminate the envelope with products of the various H-burning cycles, such as, for example, the CNO cycle. It is important that the CNONa anomalies arise within intermediate mass stars (3-8 $M_{\odot}$), in order to avoid the formation of carbon stars. In these kind of stars the second dredge-up happens shortly before reaching the AGB phase, leading to an He enrichment of the envelope. The slow winds of the intermediate mass AGB stars pollute with the processed material the pristine gas from which the other populations will form.

D'Ercole et al. (2008), using N-body hydrodinamical simulations, found that, initially, the FG must have been 10-20 times more massive than at present time. The FG formed from a first episode of star formation, that was followed by a SN explosion era. After this period, the polluted material, generated by the stellar winds of AGB stars (with mass of 5-8 $M_{\odot}$) and by ejection of planetary nebulae, moved toward the center of the cluster at low-velocity ($\sim$ 10-20 $\mathrm{km\,s^{-1}}$), forming a cooling flow. In the center of the GC a new episode of stellar formation started, forming SG stars. The ejected materials of the AGB stars had been processed through H burning at high temperature, hence the material from which SG formed was enriched in He and presented the Na-O and Al-Mg

anti-correlations. The hydrodinamical simulations of this scenario have proved that most of the stars belonging the FG were lost; this is the reason for which GCs are dominated by SG stars. This scenario have some problems; for example, it is not able to reproduce all the chemical anomalies observed in SG stars (e.g., the extreme O depletion observed in some GCs) or the large He enhancement required to reproduce the bluest MSs in $\omega$ Cen or NGC 2808.

### 1.5.2 *Fast-rotating massive stars*

Wallerstein, Myckky-Leep & Oke (1987) and Brown & Wallerstein (1993) proposed that the massive Wolf-Rayet stars could be a possible source of chemical anomalies observed in GCs. To explain the He-enhanced stars in $\omega$ Centauri, Maeder & Meynet (2006) proposed that these stars were formed from wind material of fast rotating massive stars. Prantzos & Charbonnel (2006) suggested that the winds of massive stars enriched in metallicity the material for the next stellar generation and that the SN explosions were the trigger for the star formation; the SN ejecta escape the GC environment along the cavities opened previously by the stellar winds.

In the scenario proposed by Decressin et al. (2007) and Decressin, Charbonnel & Meynet (2007) the winds of fast rotating massive stars (**FRMSs**) play an important role in the mechanism of formation of MSPs in GCs.

In this scenario, a FG stars, with mass that run from 0.1 $M_{\odot}$ to 120 $M_{\odot}$, formed from proto-cluster gas; these stars have composition similar to that of the field, with a high [O/Na] ratio. The more massive stars, which evolution is shown in Figure 8 (Decressin, Charbonnel & Meynet 2007), are also fast rotators. These stars reach the critical velocity (i.e. the velocity at the equator such that the centrifugal acceleration balances the gravity) at the beginning of their life, and remain in this status during the MS and part of the central He-burning phase. In this period, they lose material through mechanical wind, that lead to the formation of a Keplerian equatorial disc. The material of this disk presents the chemical anomalies observed in GCs, because the rotational mixing transports the products of all the burning cycles, from the core to the stellar surface. Moreover, the material is released in the circumstellar environment with very low velocity, in such a way that it can fall in the potential well of the GC, where

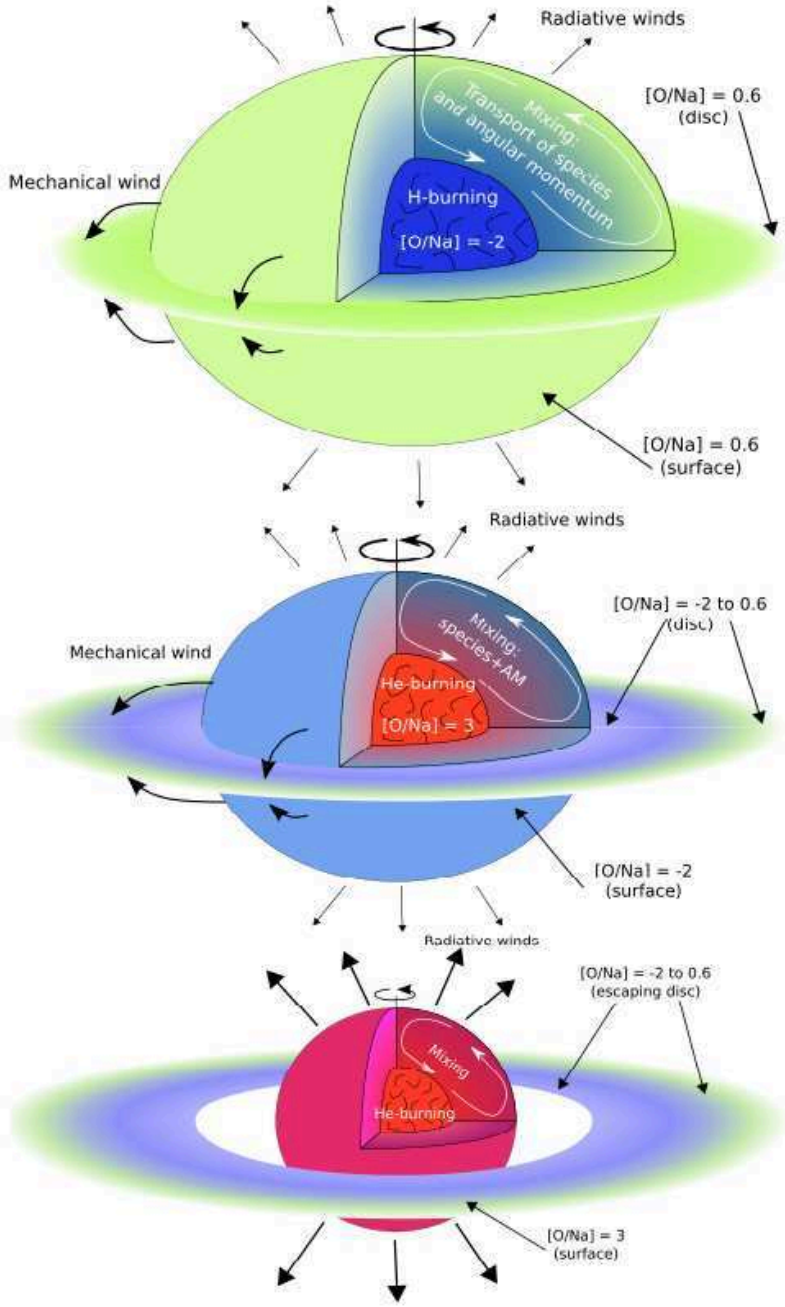


Figure 8: Schematic view of the evolution of fast rotating massive stars. The colors reflect the chemical composition of the various stellar regions: green corresponds to the initial chemical composition, blue and red are respectively for material loaded in H- and He-burning products. (from Decressin, Charbonnel & Meynet 2007, see the paper for details).

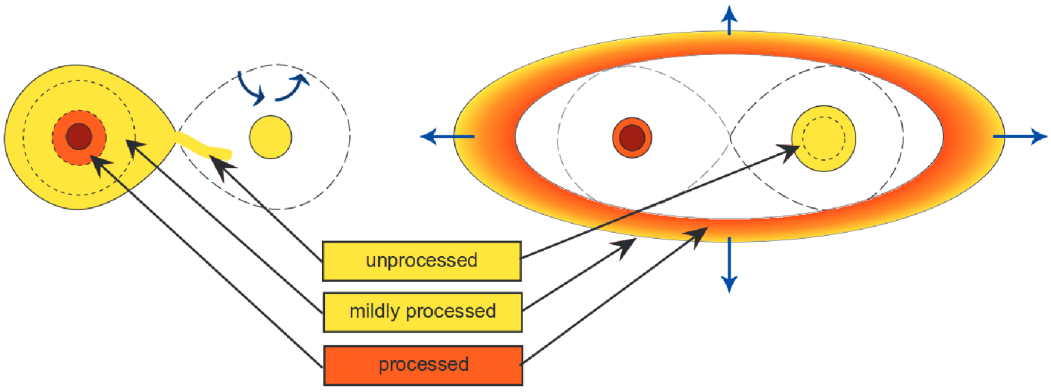


Figure 9: Schematic representation of the massive interacting binary stars scenario. Left: a binary system at the onset of mass transfer. The deepest layers in the donor star have been processed by p-capture reactions. The accreting star spins up as it accretes mass and angular momentum until it approaches the break-up limit. Right: the same system after the donor star has been stripped of its envelope. The companion star accreted just a fraction of the transferred mass, mainly unprocessed material originating from the outermost layers of the donor star. Material originating from deeper layers in the donor star is shed into a circumbinary disk. (from de Mink et al. 2010).

SG formed. The wind of massive stars, the SN shocks and the ionization front that these stars produce, trigger star formation in the vicinity of the progenitor. To take into account of the loss of FG low-mass stars and retain the observed proportion SG/FG stars, Decressin et al. (2010) in the FRMS scenario added an initial or very early mass segregation together with quick gas expulsion after the formation of the SG.

Even if the Na-O anticorrelation is well reproduced by this scenario, the expected smooth spread in $Y$ distribution is in contrast with the discreteness of the observed helium abundances. Moreover, this scenario has problems relating to the initial mass function and the predicted nucleosynthesis yields.

### 1.5.3 *Massive interacting binary stars*

de Mink et al. (2009) and Bastian et al. (2013) proposed and elaborated a scenario where massive interacting binaries (**MIBs**) are the possible source of abun-

dance anomalies in globular clusters. The majority of massive members of a GC are expected to form binary systems. Hydrogen burning processed material could be released by the interacting binaries into their surroundings during non-conservative mass transfer. This material has been part of the envelope of the primary star and is ejected at low velocities, of the order of 30-70 $\mathrm{km\,s^{-1}}$. Figure 9 shows a schematic representation of the scenario. Bastian et al. (2013) scenario includes also that the circumstellar disks of young, low mass stars sweep away the MIB ejecta. This model does not invoke the presence of multiple stellar generations.

As discussed in Bastian, Cabrera-Ziri & Salaris (2015), this model does not reproduce well the Na-O anticorrelation, because the models predict less O depletion than observed. Another problem is that the extreme yields of this model are not consistent with the small He enrichment observed in many GCs. Finally, the model does not reproduce the discreteness in the observed helium abundance distribution.

### 1.5.4 *Super-massive stars*

Super-massive stars (**SMSs**) have been proposed by Denissenkov & Hartwick (2014) and Denissenkov et al. (2015) as possible source of abundance anomalies of proton-capture elements observed in GCs. These stars are radiation-pressure-dominated objects with super-Eddington luminosities and mass of $\sim 10^4 M_\odot$, and lose mass at high rate. The SMSs in young GCs burn H in their core. After this phase, the stars lose greater part of the mass through stellar winds and various instabilities. The material lost from the SMSs is mixed with the pristine gas from which FG formed, and from this polluted medium SG is born. Because the SMSs are chemically homogeneous, the material released in the interstellar medium is enriched in helium and of products of CNO cycling, that are the chemical abundances typical of the 2G stars. Actually, this potential source has not been developed into a full scenario, i.e, how the material released by the SMSs forms new stars.

As discussed in Bastian, Cabrera-Ziri & Salaris (2015), SMSs produce too much helium for a given range in Na-O. Moreover, even if the formation of

SMSs may be stochastic in nature, the resulting yields could not have the same property and reproduce the wide range of observed GC properties.

## 1.6 RADIAL GRADIENTS OF MSPS

Combining observations from *HST* with ground-based data, it is possible to study the behavior of MSPs in a GC at different radial distances from the cluster center. An example could be the work by Milone et al. (2012d) on 47 Tuc: combining photometric and spectroscopic data from *HST* and ground-based facilities, they found that the second stellar generation of this globular is more centrally concentrated and is He-enriched.

The analysis of the radial distribution of MSPs is an very important issue. Hydrodynamical and N-body simulations for the formation and evolution of MSPs (D'Ercole et al. 2008) predict that, SG stars form in the inner regions of the cluster and are initially more concentrated than FG stars. The subsequent long-term dynamical evolution, driven by two-body relaxation, gradually erases the initial differences in the first and second generation spatial distributions, but N-body simulations predict that long relaxation-time GCs should still retain memory of the initial differences in the FG/SG spatial distribution (Vesperini et al. 2013).

As mentioned before, observational studies revealed that, for long relaxation systems, SG stars are indeed concentrated in the GC inner regions and retain some memory of the initial spatial segregation predicted by the formation and dynamical evolution models of D'Ercole et al. (2008) and Vesperini et al. (2013). Radial gradients have been found, for example, in $\omega$ Centauri (Sollima et al. 2007; Bellini et al. 2009b), 47 Tuc (Milone et al. 2012d), NGC 6388, and NGC 6411 (Bellini et al. 2013b), while a short relaxation-time GC such as NGC 6752 does not show any gradient (Nardiello et al. 2015a).

## 1.7 THE HUBBLE SPACE TELESCOPE UV LEGACY SURVEY OF GALACTIC GLOBULAR CLUSTER

The scientific results based on *Hubble Space Telescope* Treasury programme "UV Legacy Survey of Galactic Globular Clusters: Shedding Light on Their Populations and Formation" (GO 13297, PI Piotto) will be the cornerstone for understanding the mechanism of formation and evolution of multiple stellar populations in Galactic Globular Clusters. In this Chapter we describe the survey and why it is very efficient to disentangle the multiple stellar populations in globular clusters.

### 1.7.1 *Overview and observations*

The main aim of the *Hubble Space Telescope* programme "UV Legacy Survey of Galactic Globular Clusters: Shedding Light on Their Populations and Formation" (GO 13297, PI Piotto, see Piotto et al. 2015) is a detailed photometric analysis of MSPs in Galactic GCs using the UV/blue WFC3/UVIS filters F275W, F336W, and F438W. This survey is complementary to the *HST* Treasury programme "An Advanced Camera for Survey (ACS)Survey of Galactic Globular Clusters" (GO 10775, PI Sarajedini, see Sarajedini et al. 2007; Anderson et al. 2008), whose database consists of observations of GCs in the F606W and F814W bands.

The sample of the *HST* Treasury programme GO 13297 includes 47 Galactic GCs and a very old and peculiar open cluster (OC), NGC 6791 (with an age $\sim$ 8 Gyr, King et al. 2005; Bedin et al. 2008; Geisler et al. 2012). 131 *HST* orbits were allocated to this program.

To test the feasibility of the Treasury survey, two *HST* pilot projects have been carried out in the past. The data from these programmes represent an important complement to the GO 13297 data. The main pilot project was the "Advances in Understanding Multiple Stellar Generations in Globular Clusters" *HST* programme (GO 12605, PI Piotto, 22 orbits): a collection of WFC3/UVIS F275W, F336W, and F438W images of seven GCs (M 3, M 13, M 15, M 80, NGC 288, NGC 362, and NGC 2808). For these GCs there are F606W and F814W data from GO 10775 programme, too. An additional, earlier project is the "Multiple Stellar Populations in Galactic Globular Clusters" (GO 12311, PI Piotto,

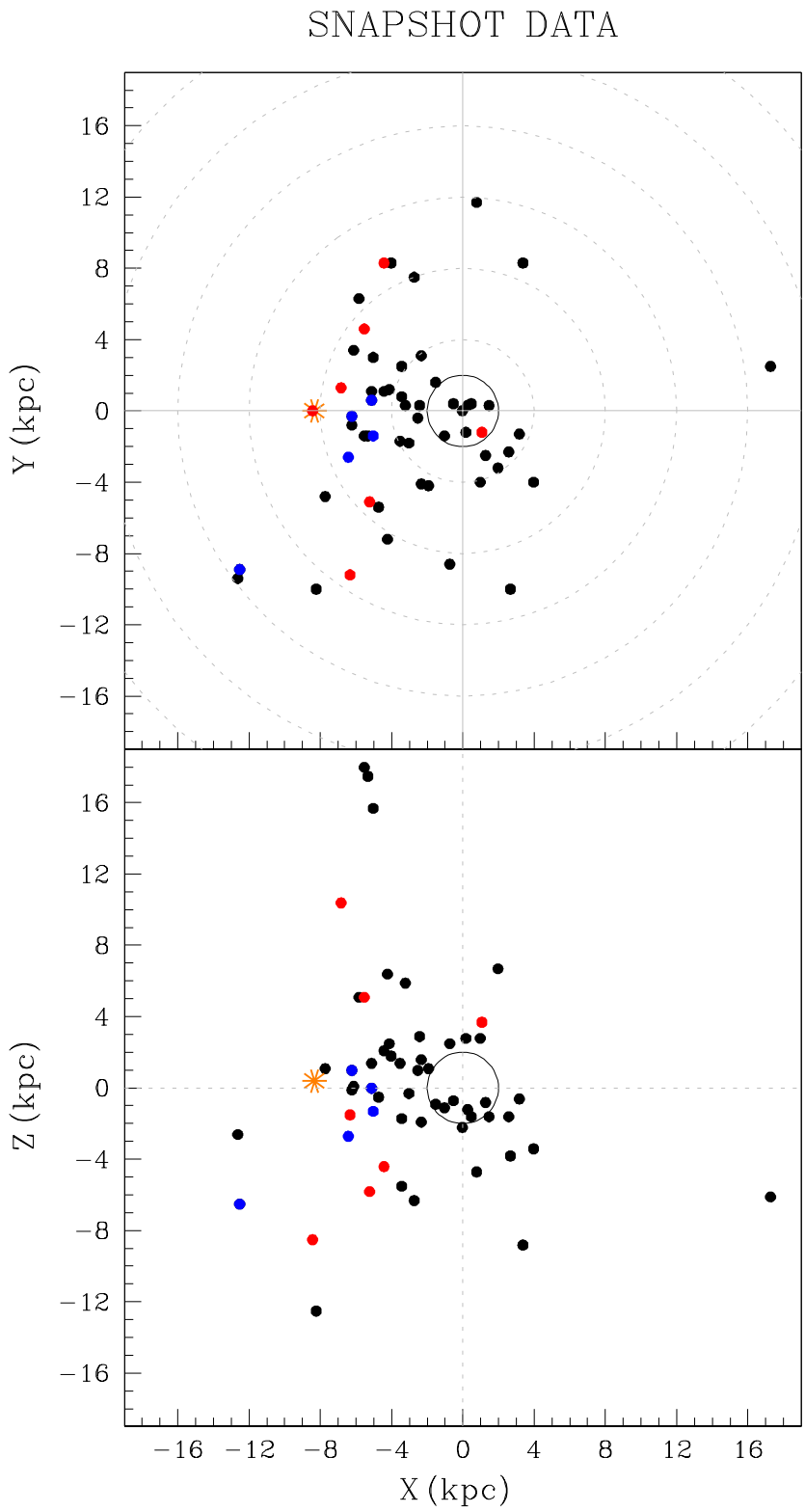


Figure 10: Spatial distribution of the target clusters for GO 13297 (black), GO 12605 (red), and GO 12311 (blue), in Galactic $XYZ$ coordinates. The adopted Sun position is indicated by an orange asterisk (from Piotto et al. 2015).

| Cluster | $X$ (kpc) | $Y$ (kpc) | $X$ (kpc) | $E(B-V)$ | $(m-M)_V$ | [Fe/H] (dex) | $M_V$ |
|---|---|---|---|---|---|---|---|
| NGC 104 (47 Tuc) | -6.4 | -2.6 | -2.7 | 0.04 | 13.37 | -0.72 | -9.42 |
| NGC 288 | -8.4 | 0.0 | -8.5 | 0.03 | 14.84 | -1.32 | -6.75 |
| NGC 362 | -5.2 | -5.1 | -5.8 | 0.05 | 14.83 | -1.26 | -8.43 |
| NGC 1261 | -8.2 | -10.0 | -12.5 | 0.01 | 16.09 | -1.27 | -7.80 |
| NGC 1851 | -12.5 | -8.9 | -6.5 | 0.02 | 15.47 | -1.18 | -8.33 |
| NGC 2298 | -12.6 | -9.4 | -2.6 | 0.14 | 15.60 | -1.92 | -6.31 |
| NGC 2808 | -6.3 | -9.2 | -1.5 | 0.22 | 15.59 | -1.14 | -9.39 |
| NGC 3201 | -7.7 | -4.8 | 1.1 | 0.24 | 14.20 | -1.59 | -7.45 |
| NGC 4590 (M 68) | -4.2 | -7.2 | 6.4 | 0.05 | 15.21 | -2.23 | -7.37 |
| NGC 4833 | -4.7 | -5.4 | -0.5 | 0.32 | 15.08 | -1.85 | -8.17 |
| NGC 5024 (M 53) | -5.5 | -1.4 | 18.0 | 0.02 | 16.32 | -2.10 | -8.71 |
| NGC 5053 | -5.3 | -1.4 | 17.5 | 0.01 | 16.23 | -2.27 | -6.76 |
| NGC 5272 (M 3) | -6.8 | 1.3 | 10.4 | 0.01 | 15.07 | -1.50 | -8.88 |
| NGC 5286 | -0.7 | -8.6 | 2.5 | 0.24 | 16.08 | -1.69 | -8.74 |
| NGC 5466 | -5.0 | 3.0 | 15.7 | 0.00 | 16.02 | -1.98 | -6.98 |
| NGC 5897 | 2.0 | -3.2 | 6.7 | 0.09 | 15.76 | -1.90 | -7.23 |
| NGC 5904 (M 5) | -3.2 | 0.3 | 5.9 | 0.03 | 14.46 | -1.29 | -8.81 |
| NGC 5927 | -1.9 | -4.2 | 1.1 | 0.45 | 15.82 | -0.49 | -7.81 |
| NGC 5986 | 1.0 | -4.0 | 2.8 | 0.28 | 15.96 | -1.59 | -8.44 |
| NGC 6093 (M 80) | 1.1 | -1.2 | 3.7 | 0.18 | 15.56 | -1.75 | -8.23 |
| NGC 6101 | 2.7 | -10.0 | -3.8 | 0.05 | 16.10 | -1.98 | -6.94 |
| NGC 6121 (M 4) | -6.2 | -0.3 | 1.0 | 0.35 | 12.82 | -1.16 | -7.19 |
| NGC 6144 | 0.2 | -1.2 | 2.8 | 0.36 | 15.86 | -1.76 | -6.85 |
| NGC 6171 | -2.4 | 0.3 | 2.9 | 0.33 | 15.05 | -1.02 | -7.12 |
| NGC 6205 (M 13) | -5.5 | 4.6 | 5.1 | 0.02 | 14.33 | -1.53 | -8.55 |
| NGC 6218 (M 12) | -4.1 | 1.2 | 2.5 | 0.19 | 14.01 | -1.37 | -7.31 |
| NGC 6254 (M 10) | -4.4 | 1.1 | 2.1 | 0.28 | 14.08 | -1.56 | -7.48 |
| NGC 6304 | -2.5 | -0.4 | 1.0 | 0.54 | 15.52 | -0.45 | -7.30 |
| NGC 6341 (M 92) | -5.8 | 6.3 | 5.1 | 0.02 | 14.65 | -2.31 | -8.21 |
| NGC 6352 | -3.0 | -1.8 | -0.3 | 0.22 | 14.43 | -0.64 | -6.47 |
| NGC 6362 | -2.3 | -4.1 | -1.9 | 0.09 | 14.68 | -0.99 | -6.95 |
| NGC 6366 | -5.1 | 1.1 | 1.4 | 0.71 | 14.94 | -0.59 | -5.74 |

Table 1: List of the Clusters observed in the GO 12311, GO 12605, and GO 13297 missions and the corresponding main parameters: Galactic $XYZ$ Coordinates, Reddening, Distance Modulus, Metallicity, and Absolute visual magnitude

| Cluster | $X$ (kpc) | $Y$ (kpc) | $X$ (kpc) | $E(B-V)$ | $(m-M)_V$ | [Fe/H] (dex) | $M_V$ |
|---|---|---|---|---|---|---|---|
| NGC 6388 | 1.3 | -2.5 | -0.8 | 0.37 | 16.13 | -0.55 | -9.41 |
| NGC 6397 | -6.2 | -0.8 | -0.1 | 0.18 | 12.37 | -2.02 | -6.64 |
| NGC 6441 | 3.2 | -1.3 | -0.6 | 0.47 | 16.78 | -0.46 | -9.63 |
| NGC 6496 | 2.6 | -2.3 | -1.6 | 0.15 | 15.74 | -0.46 | -7.20 |
| NGC 6535 | -2.3 | 3.1 | 1.6 | 0.34 | 15.22 | -1.79 | -4.75 |
| NGC 6541 | -1.0 | -1.4 | -1.1 | 0.14 | 14.82 | -1.81 | -8.52 |
| NGC 6584 | 4.0 | -4.0 | -3.4 | 0.10 | 15.96 | -1.50 | -7.69 |
| NGC 6624 | -0.5 | 0.4 | -0.7 | 0.28 | 15.36 | -0.44 | -7.49 |
| NGC 6637 (M 69) | 0.3 | 0.3 | -1.2 | 0.18 | 15.28 | -0.64 | -7.64 |
| NGC 6652 | 1.5 | 0.3 | -1.6 | 0.09 | 15.28 | -0.81 | -6.66 |
| NGC 6656 (M 22) | -5.1 | 0.6 | -0.0 | 0.34 | 13.60 | -1.70 | -8.50 |
| NGC 6681 (M 70) | 0.5 | 0.4 | -1.6 | 0.07 | 14.99 | -1.62 | -7.12 |
| NGC 6715 (M 54) | 17.3 | 2.5 | -6.1 | 0.15 | 17.58 | -1.49 | -9.98 |
| NGC 6717 | -1.5 | 1.6 | -0.9 | 0.22 | 14.94 | -1.26 | -5.66 |
| NGC 6723 | -0.0 | 0.0 | -2.2 | 0.05 | 14.84 | -1.10 | -7.83 |
| NGC 6752 | -5.0 | -1.4 | -1.3 | 0.04 | 13.13 | -1.54 | -7.73 |
| NGC 6779 (M 56) | -4.0 | 8.3 | 1.8 | 0.26 | 15.68 | -1.98 | -7.41 |
| NGC 6791 | -3.5 | -1.7 | 1.4 | 0.12 | 13.43 | 0.15 | -3.93 |
| NGC 6809 (M 55) | -3.4 | 0.8 | -1.7 | 0.08 | 13.89 | -1.94 | -7.57 |
| NGC 6838 (M 71) | -6.1 | 3.4 | 0.10 | 0.25 | 13.80 | -0.78 | -5.61 |
| NGC 6934 | 0.8 | 11.7 | -4.7 | 0.10 | 16.28 | -1.47 | -7.45 |
| NGC 6981 (M 72) | 3.4 | 8.3 | -8.8 | 0.05 | 16.31 | -1.42 | -7.04 |
| NGC 7078 (M 15) | -4.4 | 8.3 | -4.4 | 0.10 | 15.39 | -2.37 | -9.19 |
| NGC 7089 (M 2) | -2.7 | 7.5 | -6.3 | 0.06 | 15.50 | -1.65 | -9.03 |
| NGC 7099 (M 30) | -3.4 | 2.5 | -5.5 | 0.03 | 14.64 | -2.27 | -7.45 |

Table 1.7 (Continued)

17 orbits). For this programme WFC3/UVIS F275W images (complementary to the F606W and F814W observations from GO 10775) of five clusters (47 Tuc, M 4, M 22, NGC 1851, and NGC 6752) have been collected. For NGC 1851, M 4, and M 22 observations in F336W and F438W have been collected during the GO 13297.

In summary, all the *HST* programmes described in this section provide data for 56 GCs and an old OC, in five photometric bands: F275W, F336W, F438W, F606W, and F814W. As shown in the next sections, these bands, especially UV/blue are crucial to identify MSPs in all the analyzed GCs. Moreover

the overlaps between the GO 13297 and GO 10775 images, provide a temporal baseline of $\sim 7-8$ years, enough to compute the relative stellar proper motion and the membership probabilities.

In Fig. 10 the distribution of the globular clusters in the Galactic $XY$ and $XZ$ planes is shown. Table 1.7 lists the 57 clusters with some of their properties, such as $XYZ$ Galactocentric coordinates, the reddening, the distance modulus, the metallicity, and the absolute visual magnitude (from Harris 1996, 2010 edition).

### 1.7.2 *WFC3/UVIS' UV/blue Filters*

A great number of spectroscopic works (e.g.,Yong et al. 2008; Marino et al. 2008; Lee et al. 2009b; Lim et al. 2015), ground-based photometric works (e.g.,Lee et al. 1999; Han et al. 2009; Roh et al. 2011; Monelli et al. 2013; Lee et al. 2013; Nardiello et al. 2015a) and *HST* photometric works (e.g.,Bellini et al. 2010, 2013a; Milone et al. 2012a,c,d, 2013; Piotto et al. 2012, 2013) have demonstrated that Strömgren and ultraviolet photometries are good tools for separating MSPs across the entire CMD of Galactic GCs.

Figure 11 help understanding why the combinations of UV filters is a powerful tool to disentangle the MSPs in GCs. The upper panel shows, in red, the simulated spectrum of a star of the first stellar generation (N-poor, He-poor) which belongs the RGBa of NGC 6752, and in blue the simulated spectrum of a third generation, N-rich, He-rich, RGBc star (Milone et al. 2010); in the middle panel there is the flux ratio of the two spectra reproduced in the upper panel. The lower panel shows the band-passes of WFC/UVIS filters F275W, F336W, and F438W.

As described by Milone et al. (2012d), F275W pass-band includes an OH molecular band, F336W an NH band, and F438W CN and CH bands, as also illustrated in the upper panel of Fig. 11. This property of the *HST* filter system is at the basis of the Treasury programme. The first generation stars, which are oxygen- and carbon-rich and nitrogen-poor, are relatively faint in F275W and F438W, but bright in F336W. Conversely, second generation stars, whose material has been CNO-cycle processed, are oxygen- and carbon-poor, but nitrogen-rich. As a consequence, they are relatively bright in F275W and F438W, but faint in

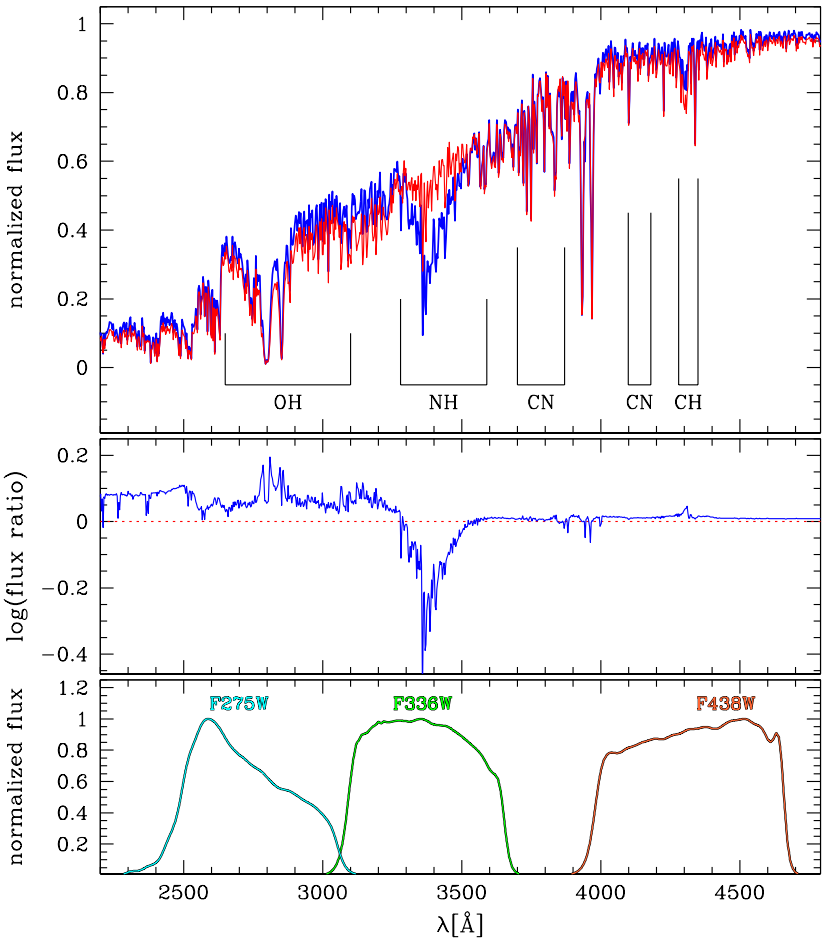


Figure 11: Upper panel: in red the simulated spectrum of a star of the first stellar generation (N-poor) RGBa in NGC 6752; in blue the simulated spectrum of a third generation, N-rich, RGBc star (Milone et al. 2010). Middle panel: flux ratio of the two spectra reproduced in the upper panel. Lower panel: band-passes of WFC3/UVIS with F275W, F336W, and F438W (from Piotto et al. 2015).

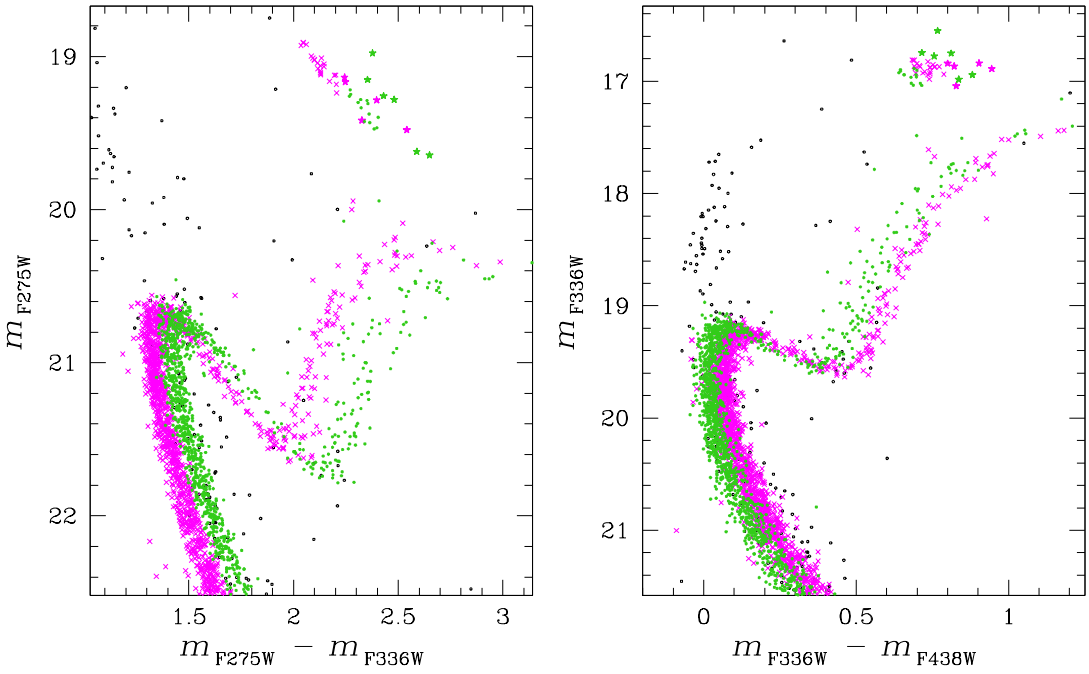


Figure 12: The $m_{F275W}$ versus $m_{F275W} - m_{F336W}$ (left panel) and $m_{F336W}$ versus $m_{F336W} - m_{F438W}$ (right panel) CMDs of NGC 6352. In the first CMD, first-generation stars (green dots) are redder than second-generation stars (magenta crosses), while in the second CMD, first-generation stars have, on average, bluer colors than second-generation stars.

F336W. Therefore, first generation stars are bluer then second generation ones in one color (F336W−F438W), but redder in another (F275−F336W), and this inversion is seen in Figure 12 in the case of NGC 6352: the left panel shows that in the $m_{F275W}$ versus $m_{F275W} - m_{F336W}$ CMD first-generation stars (green) are redder than second-generation stars (magenta), while the right panel shows that in the $m_{F336W}$ versus $m_{F336W} - m_{F438W}$ CMD first-generation stars are bluer than second-generation ones.

Milone et al. (2013) defined a pseudo-color $C_{F275W,F336W,F438W} = (m_{F275W} - m_{F336W}) - (m_{F336W} - m_{F438W})$, which is quite efficient in the separation of multiple sequences because it maximizes the virtue of both F336W-F438W and F275W-F336W colors.

Figure 13 shows an example for the NGC 6352 data. The left panels show the power of the pseudo-color $C_{F275W,F336W,F438W}$ in separating all the sequences in the pseudo-CMD. The middle panels show that in the $m_{F336W}$ versus

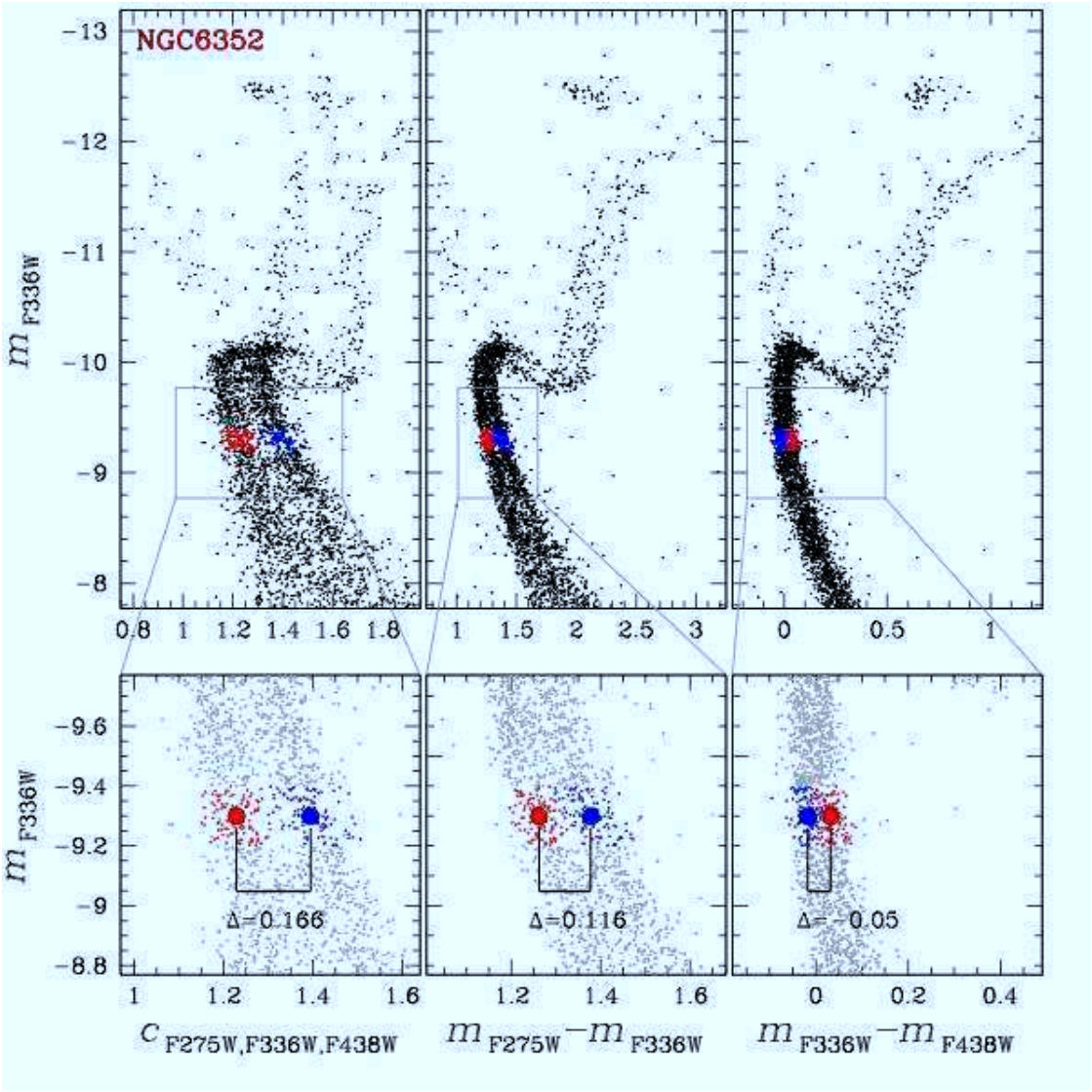


Figure 13: CMDs of NGC 6352 from GO 13297 data. $m_{F336W}$ versus $C_{F275W,F336W,F438W}$ (left panels), $m_{F336W}$ versus $m_{F275W} - m_{F336W}$ (middle panels), and $m_{F336W}$ versus $m_{F336W} - m_{F438W}$ (right panels) CMDs. Lower panels show a zoom of the MS. Red dots highlight second-generation stars; blue dots first-generation stars (from Piotto et al. 2015).

$m_{\rm F275W} - m_{\rm F336W}$ CMDs, firts-generation stars are redder then second-generation ones, but they become bluer in the $m_{\rm F336W}$ versus $m_{\rm F336W} - m_{\rm F438W}$ CMDs (right panels).

Thanks to F275W, F336W, and F438W data, the two stellar generations are clearly distinguished from the MS, through the SGB, the RGB to the HB.

The UV pass-bands are thus able to probe the CNO content of the cluster stars. Note that the nuclear processes that produce the light-element (anti-)correlations (e.g., the Na-O or the Mg-Al anti-correlations) also produce helium, and measuring the helium enhancement of each sub-population is particularly important to help pinpoint what kind of stars may have produced the second-generation material. Enhanced helium abundance affects the interior structure of stars, leading to changes in luminosity and effective temperature, while it is irrelevant for the atmospheric structure at fixed $\log g$ and $T_{eff}$, even for extreme enhancement (e.g., $Y = 0.40$, Sbordone et al. 2011). The photometric impact of helium is mainly on the optical bands, and, using synthetic spectra, it is possible to measure variations of only a few percent in helium between the different populations (as demonstrated in Chapter 2 and 3; see also Milone et al. 2012d,a, 2013 ). Therefore, combinations of UV and optical colors permit to estimate the content of C, N, O, and He, even for stars that are too faint to pursue with spectroscopy (Milone et al. 2012d,a, 2013).

When a GC hosts a population enhanced in helium, the HB morphology could be anomalous (bluer and extended HB). These anomalies can be better observed in UV. When $Y$ is increased from 0.23 to 0.38 the blue HB becomes 1 mag brighter in F275W, while the extreme HB becomes 0.5 mag fainter. Thus the UV band is crucial for determining the physical parameters of HB stars and their helium content.

### 1.7.3 *Multiple stellar populations and principal goals of the Treasury programme GO 13297*

The principal goal of the *HST* Treasury programme GO 13297 is the analysis of all the phenomena related to the MSPs in GCs. However, the data could be useful also for a large number of other projects.

Combining UV/blue and optical filters, it is possible to distinguish between different effect due to differences in He, C, N, O, Na content. Combining synthetic spectra based on observed (when possible) chemical compositions with the behavior of the multiple stellar populations in different CMDs, it is possible to obtain the relative helium abundance for each stellar population. This technique has been applied to some GCs, such as, for example, 47 Tuc (Milone et al. 2012d), NGC 6397 (Milone et al. 2012a), NGC 288 (Piotto et al. 2013), NGC 6752 (Milone et al. 2013), M 4 (Nardiello et al. 2015a, see Chapter 2), and NGC 6352 (Nardiello et al. 2015b, see Chapter 3)

The combination of UV/blue data with optical data permits to compute GC radial star density profiles based on resolved star counts (see Ferraro et al. 2003; Miocchi et al. 2013). The radial density profiles are an important tool useful to characterize the structural and dynamical properties of GCs.

A good fraction of the GCs observed during the GO 13297 mission was also observed during the GO 10775 and other *HST* programmes. This permits to measure internal proper motions with time baselines between 7 and 14 years. This permits to measure separately the kinematical properties of each different stellar population hosted by a GC and photometrically identified. Kinematical differences between the populations would strongly constraint formation mechanism of MSPs. With the internal proper motions it is possible to obtain direct measurements of the radial velocity dispersion profiles, the velocity dispersion anisotropy, and possible rotation of many GCs. Moreover, it is possible to create dynamical models to constrain the mass profiles of the GCs, including the presence of intermediate-mass black holes (see for example van der Marel & Anderson 2010 for the case of $\omega$ Cen).

The GO 13297 data set would be useful to obtain the distances of the Galactic GCs. Indeed, GC distances have generally been obtained mostly through isochrone-fitting techniques and the RR Lyrae variables. By comparing high-precision *HST* proper motions (at the level of mas $yr^{-1}$) with existing line of sight velocity data (in km $s^{-1}$), it becomes possible to obtain entirely independent kinematical distance estimates.

The HB of GCs contains a large number of information about the MSPs. Because optical colors become degenerate at high temperature, the UV bands are useful to characterize the full HB morphology, including the extreme HB.

At higher $Y$, the HB generally extends to hotter temperature, and also exhibits significant variations in luminosity, with higher luminosity on the blue HB and lower luminosity on the extreme HB. It has already been demonstrated that peculiar HB of some GCs are associated to the MSPs phenomenon; some examples are: NGC 2808 (D'Antona et al. 2005; Piotto et al. 2007; Dalessandro et al. 2011), NGC 6388 and NGC 6441 (Busso et al. 2007; Caloi & D'Antona 2007; Bellini et al. 2013b). This connection is supported by recent studies, based on spectroscopy of HB stars, which have shown that distinct stellar populations, with different content of light elements and helium, occupy different regions along the HB (Marino et al. 2011c; Marino, Milone & Lind 2013; Marino et al. 2014a; Villanova et al. 2012; Gratton et al. 2011, 2012, 2013). Milone et al. (2014b) analyzed the effects of GC global and local parameters on the HB morphology; the GO 13297 data will be useful to extend this investigation.

As demonstrated in Chapter 3, the GO 13297 data are useful to constraint the ages of the different populations hosted by a GC. Relative ages of 64 GCs were measured in the ACS Treasury Program of Galactic GCs (Marín-Franch et al. 2009). Single stellar populations were assumed, however, and no dependence on chemical abundances was taken into account. As demonstrated in Chapter 3, with GO 13297 data it is possible to distinguish different stellar populations hosted by a GC, that are characterized by different light element and helium contents, and to measure their relative age.

The GO 13297 data set has permitted to confirm that the MSPs phenomenon is common to almost all GCs. Figures 14-28 show the $m_{\rm F275W}$ versus $C_{\rm F275W,F336W,F438W}$ for 45 GCs in the GO 13297 data set. All the GCs are corrected for differential reddening, using the procedure described by Milone et al. (2012d). It is possible to note that all the GCs show multiple sequences, as a photometric evidence of multiple stellar populations.

### 1.7.4 *Summary*

In this section we have illustrated the *Hubble Space Telescope* programme "UV Legacy Survey of Galactic Globular Clusters: Shedding Light on Their Populations and Formation" (GO 13297, PI Piotto), a WFC3/UVIS survey of 56 GCs and an old OC in F275W, F336W, and F438W *HST* bands. This survey is com-

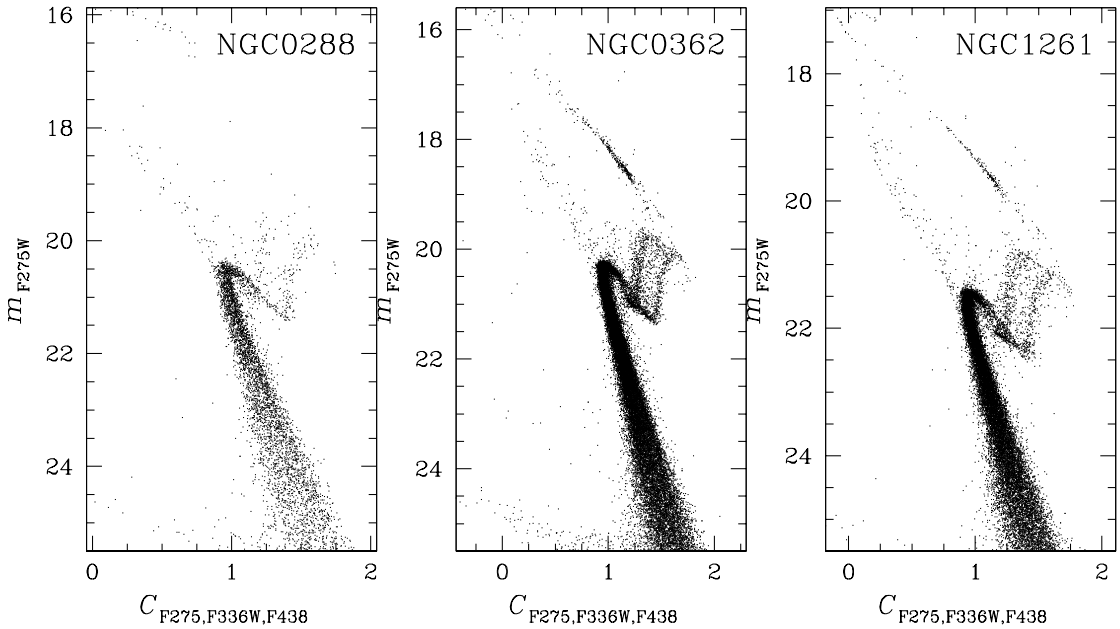


Figure 14: The $m_{F275W}$ versus $C_{F275W,F336W,F438W}$ pseudo-CMDs for NGC 288, NGC 362, and NGC 1261.

plementary to the *HST* Treasury programme "An Advanced Camera for Survey (ACS)Survey of Galactic Globular Clusters" (GO 10775, PI Sarajedini), that consists of observations of the same clusters in F606W and F814W. In this way, for each cluster it is possible to analyze the color-magnitude and color-color diagrams combining five photometric bands.

The main goal of the GO 13297 survey is the characterization and the analysis of multiple stellar populations hosted by GCs. Thanks to the "magic trio" of filters, it is possible to disentangle the multiple stellar populations in all the GCs present in the sample of the survey. Indeed, we know that different stellar populations, hosted by a GC, are characterized by different C, N, O, Na, and He content, in particular the first generations of stars are N-poor and C- and O-rich, while the second generation is N-rich and C- and O-poor. The reason why the "magic trio" of filter is very efficient is that the *HST* WFC3/UV photometric bands are centered on the molecular bands of OH (F275W), NH (F336W), CN, and CH (F438W) and are therefore sensible to C, N, and O variations of these elements among the different stellar populations.

The combination of UV/blue data with optical data permits to compute the relative helium abundance among different stellar populations hosted by a GC. This is possible exploiting the sensitivity of various colors to different prop-

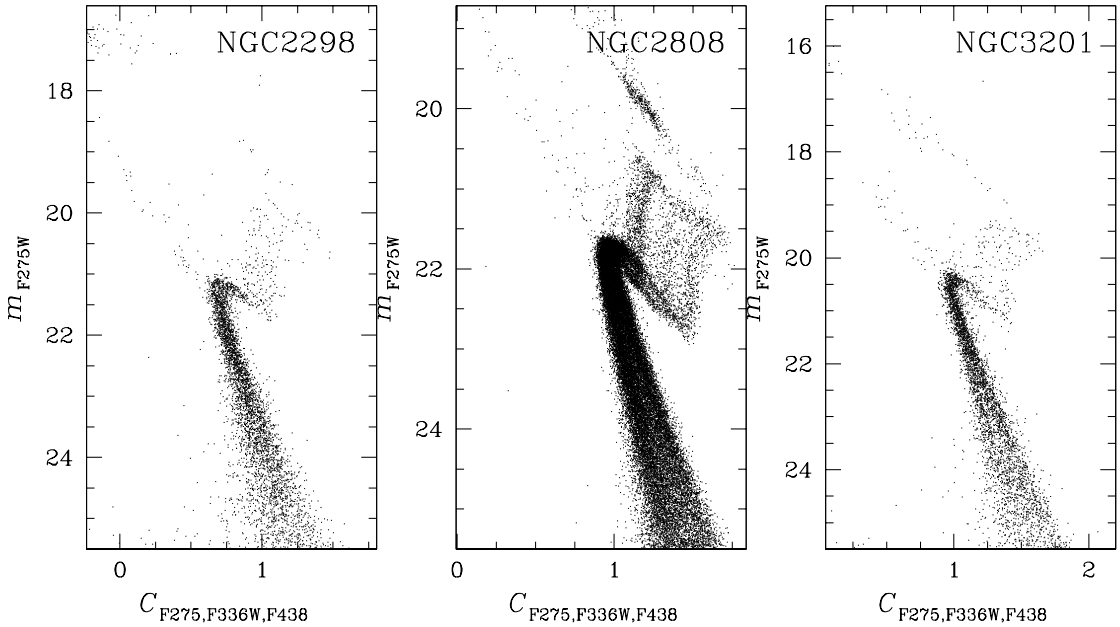


Figure 15: The $m_{F275W}$ versus $C_{F275W,F336W,F438W}$ pseudo-CMDs for NGC 2298, NGC 2808, and NGC 3201.

erties of stellar populations and combining the photometric information with grids of synthetic spectra constructed with chemical compositions constrained from spectroscopic observations.

The chance to distinguish different stellar populations across the entire CMD, particularly around the MS turn-off, permits to obtain the ages of different stellar populations. Indeed, in the past the ages of all the GCs in the GO 10775 data set were calculated without taking into account the presence of multiple stellar populations. Now, it is possible to treat the different stellar populations as single stellar populations and compute the age for each of them, and therefore to put constraints on the relative age (see Chapter 3).

Finally , the GO 13297 data set will be useful for a large number of other project, such as, internal proper motion analysis, internal dynamical models, absolute proper motions, modeling of the radial distribution of multiple stellar populations, estimate of GC distances, analysis of CMDs' regions (RGB bump, HB morphology, AGB star counts), analysis of binaries, blue stragglers, stellar exotica and X-ray sources, differential reddening map and luminosity and mass functions.

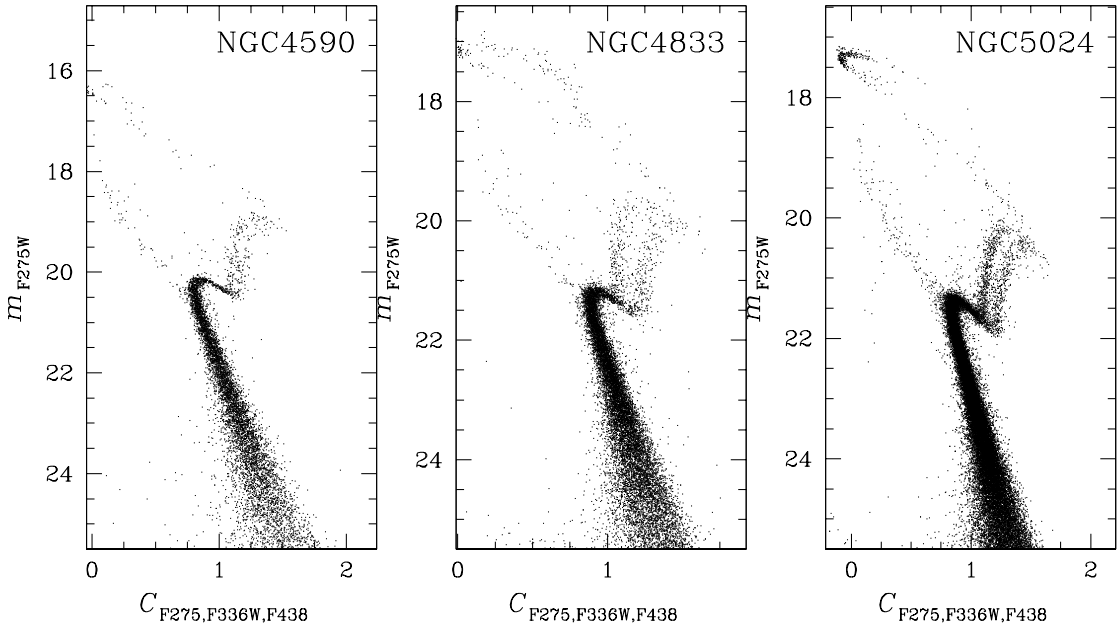


Figure 16: The $m_{F275W}$ versus $C_{F275W,F336W,F438W}$ pseudo-CMDs for NGC 4590, NGC 4833, and NGC 5024.

## 1.8 THESIS LAYOUT

The thesis is structured as follows:

- In Chapter 2, I discuss the results of the ground-based photometric analysis of MS stars of three Galactic GCs: NGC 6121 (M 4), NGC 6397 and NGC 6752. We were able to find the presence of MSPs in two of these clusters (M 4 and NGC 6752), especially thanks to a combination of $UBVI$ filters. We analyzed the radial distributions of the various stellar populations from the center to the outskirts of each GC and the helium enrichment of the SG stars.

- Chapter 3 regards the analysis of the GC NGC 6352 based on GO 13297 *HST* data. We were able to split all the sequences in the CMDs of this GC, from the MS, to the SGB, RGB, and HB. We computed the helium enrichment of the SG stars. The most important result is the constraint on the relative age between the two populations. Using isochrones, synthetic CMDs and considering the uncertainties on [Fe/H], [$\alpha$/Fe] and $Y$, we were able to put an upper limit on the difference in age between the two generations.

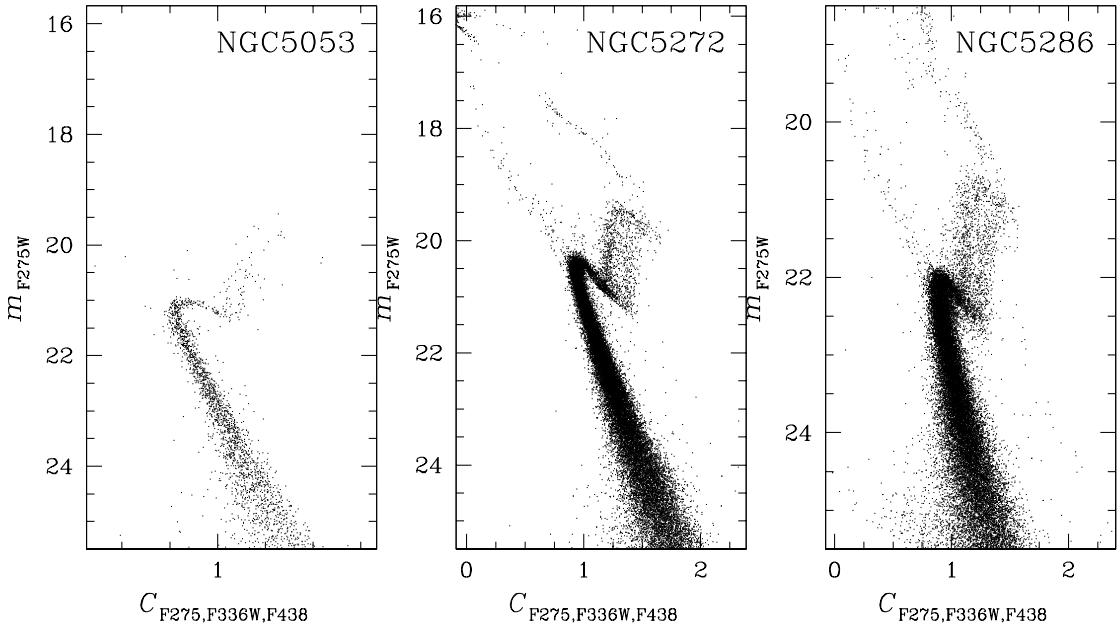


Figure 17: The $m_{F275W}$ versus $C_{F275W,F336W,F438W}$ pseudo-CMDs for NGC 5053, NGC 5272, and NGC 5286.

- in Chapter 4 I present a summary of my works and a list of the future projects that I plan to execute.

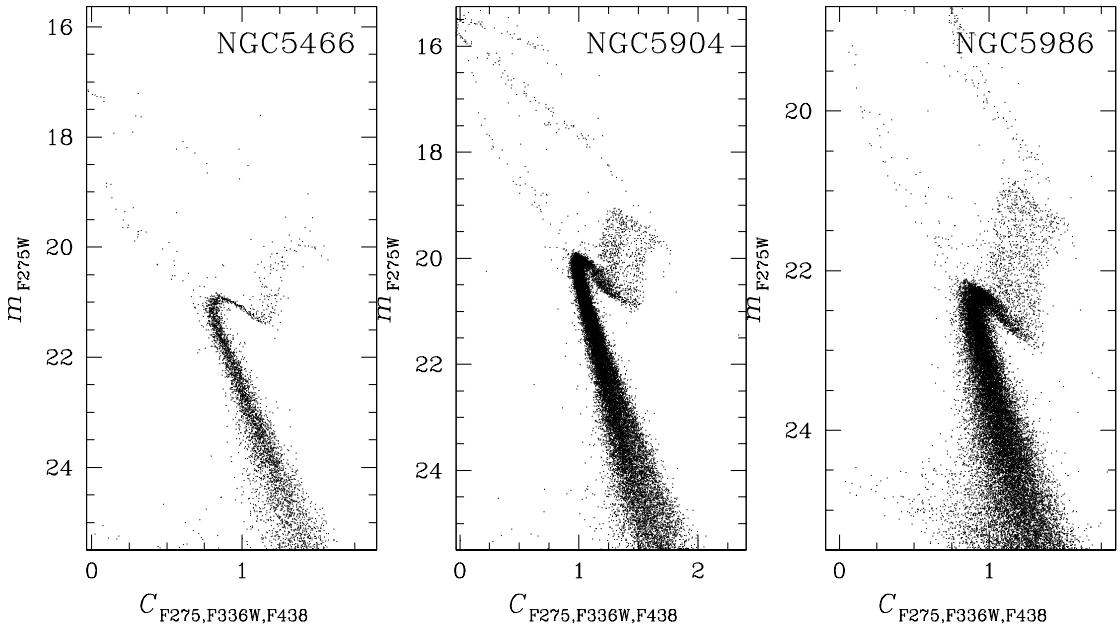


Figure 18: The $m_{F275W}$ versus $C_{F275W,F336W,F438W}$ pseudo-CMDs for NGC 5466, NGC 5904, and NGC 5986.

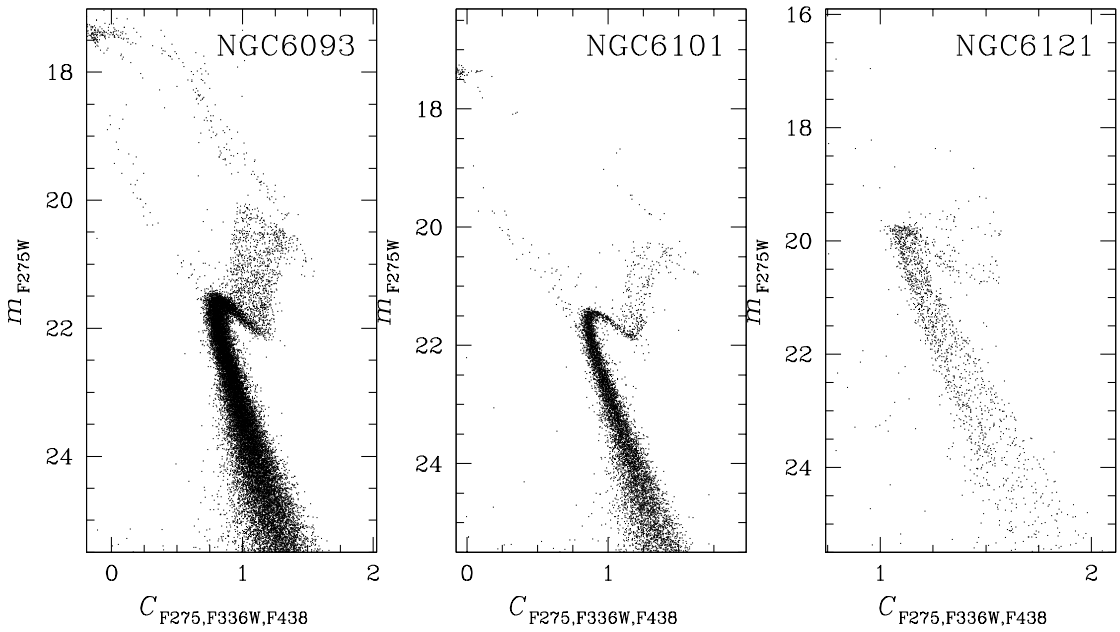


Figure 19: The $m_{F275W}$ versus $C_{F275W,F336W,F438W}$ pseudo-CMDs for NGC 6093, NGC 6101, and NGC 6121.

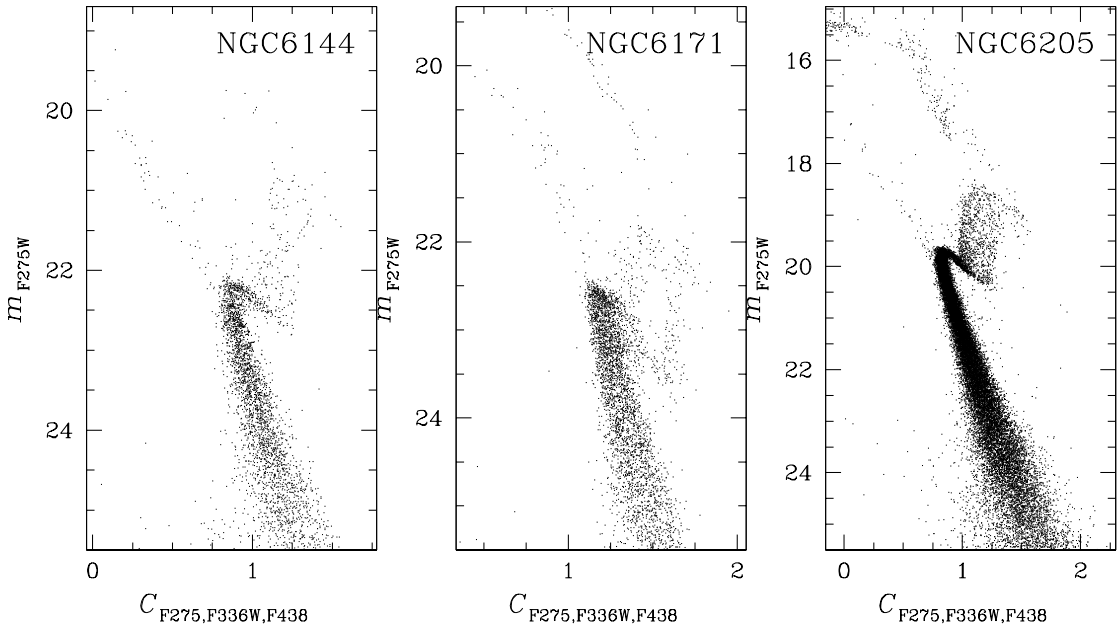


Figure 20: The $m_{F275W}$ versus $C_{F275W,F336W,F438W}$ pseudo-CMDs for NGC 6144, NGC 6171, and NGC 6205.

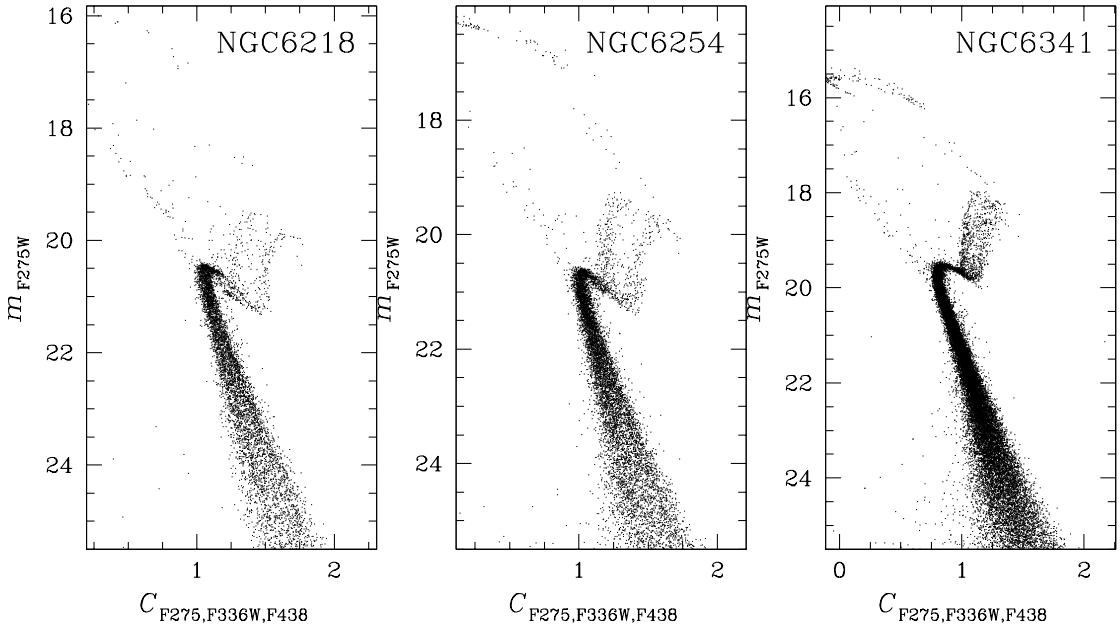


Figure 21: The $m_{F275W}$ versus $C_{F275W,F336W,F438W}$ pseudo-CMDs for NGC 6218, NGC 6254, and NGC 6341.

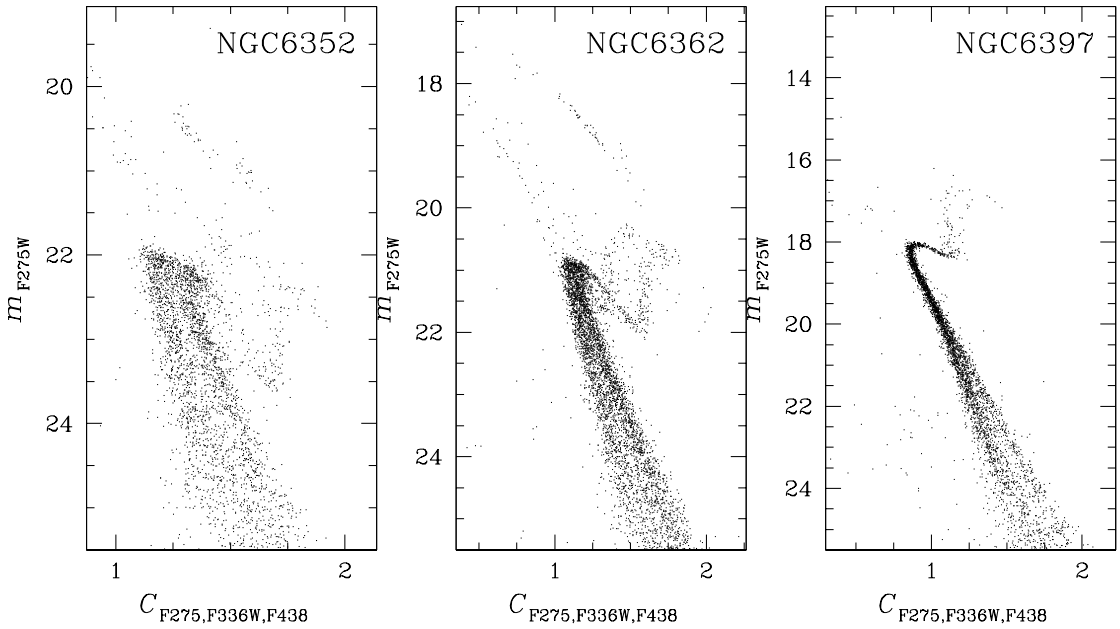


Figure 22: The $m_{F275W}$ versus $C_{F275W,F336W,F438W}$ pseudo-CMDs for NGC 6352, NGC 6362, and NGC 6397.

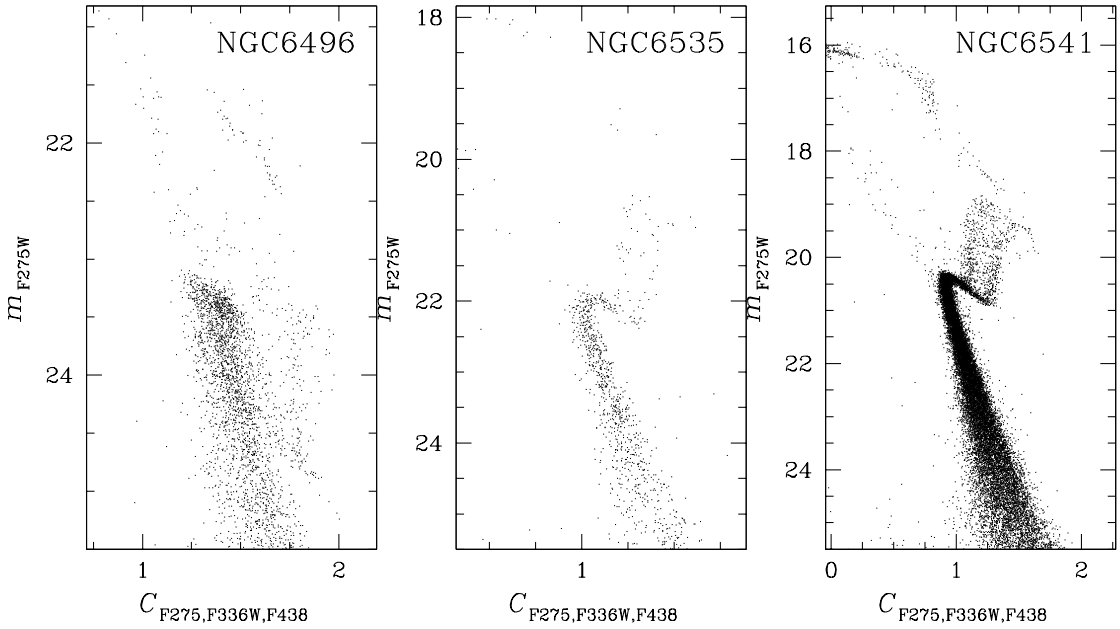


Figure 23: The $m_{F275W}$ versus $C_{F275W,F336W,F438W}$ pseudo-CMDs for NGC 6496, NGC 6535, and NGC 6541.

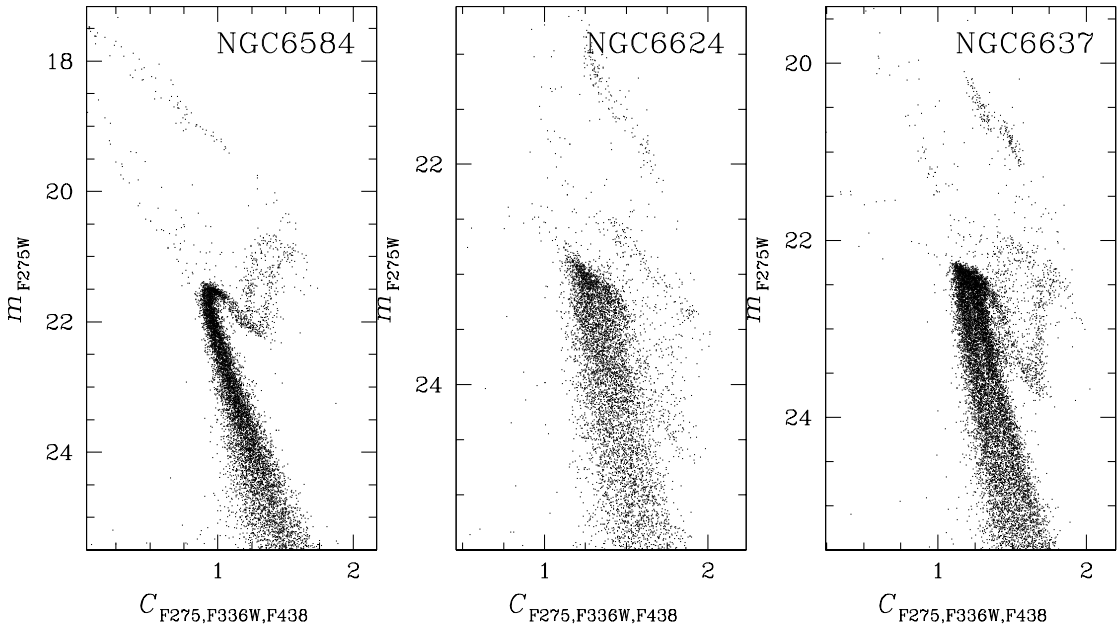


Figure 24: The $m_{F275W}$ versus $C_{F275W,F336W,F438W}$ pseudo-CMDs for NGC 6584, NGC 6624, and NGC 6637.

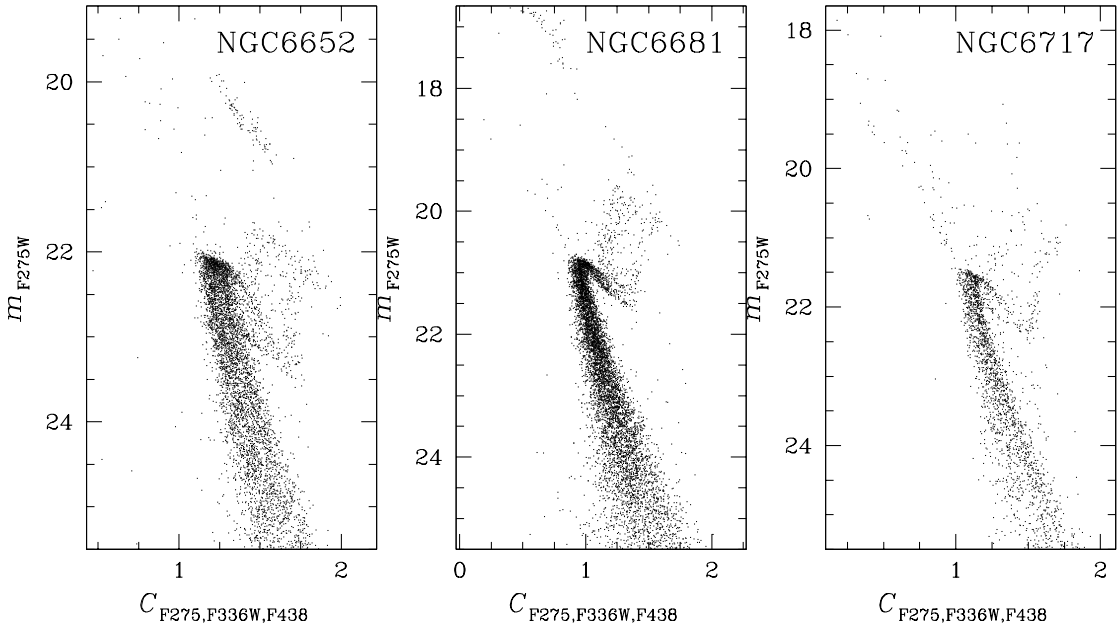


Figure 25: The $m_{F275W}$ versus $C_{F275W,F336W,F438W}$ pseudo-CMDs for NGC 6652, NGC 6681, and NGC 6717.

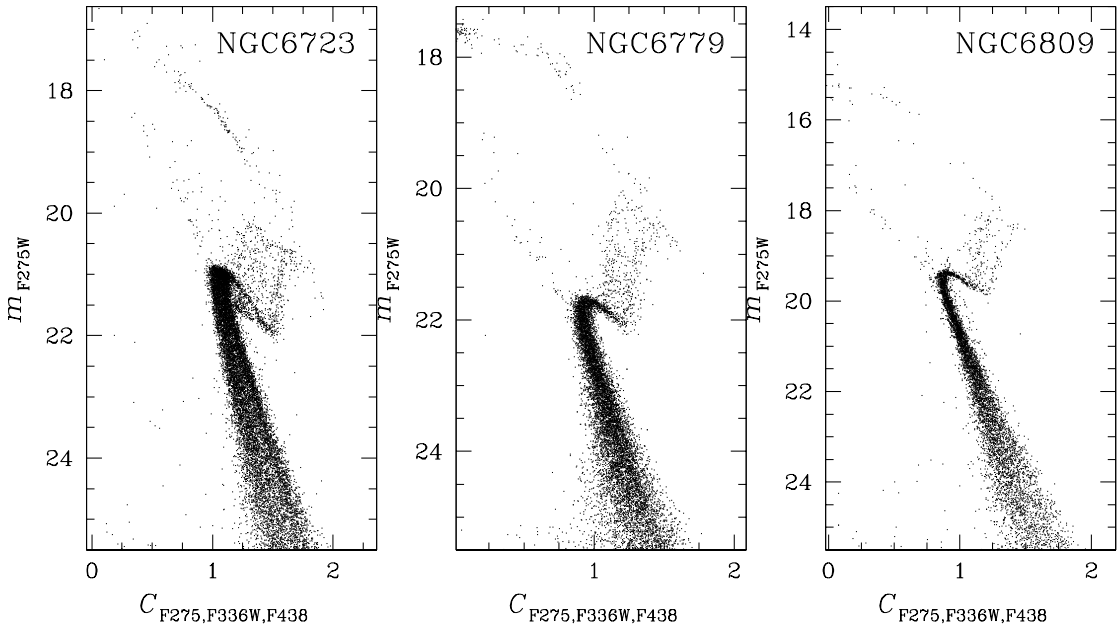


Figure 26: The $m_{F275W}$ versus $C_{F275W,F336W,F438W}$ pseudo-CMDs for NGC 6723, NGC 6779, and NGC 6809.

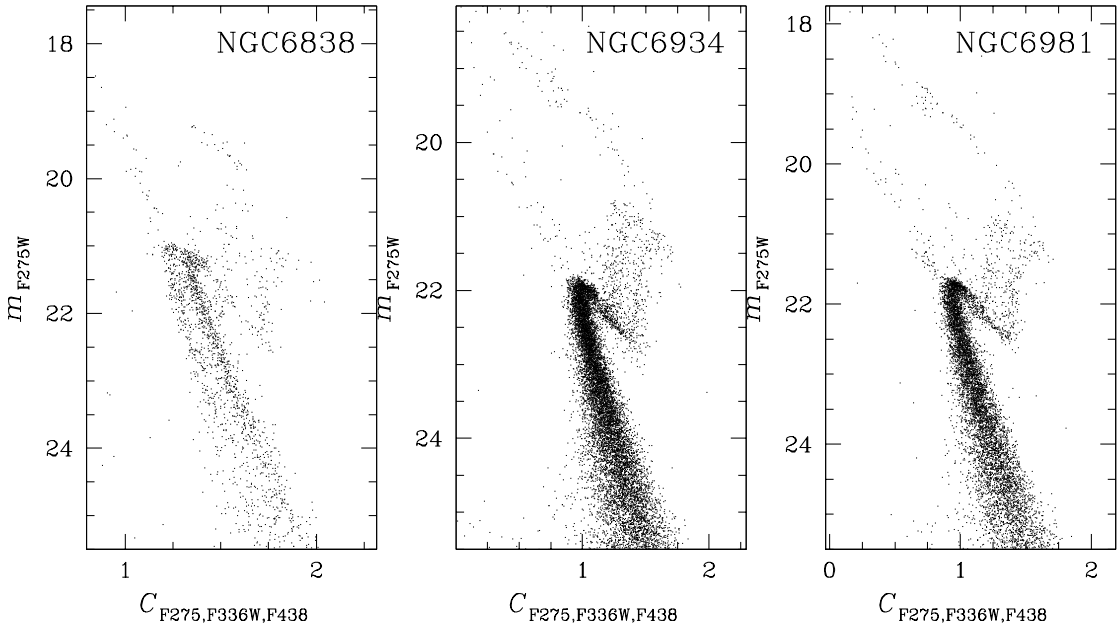


Figure 27: The $m_{F275W}$ versus $C_{F275W,F336W,F438W}$ pseudo-CMDs for NGC 6838, NGC 6934, and NGC 6981.

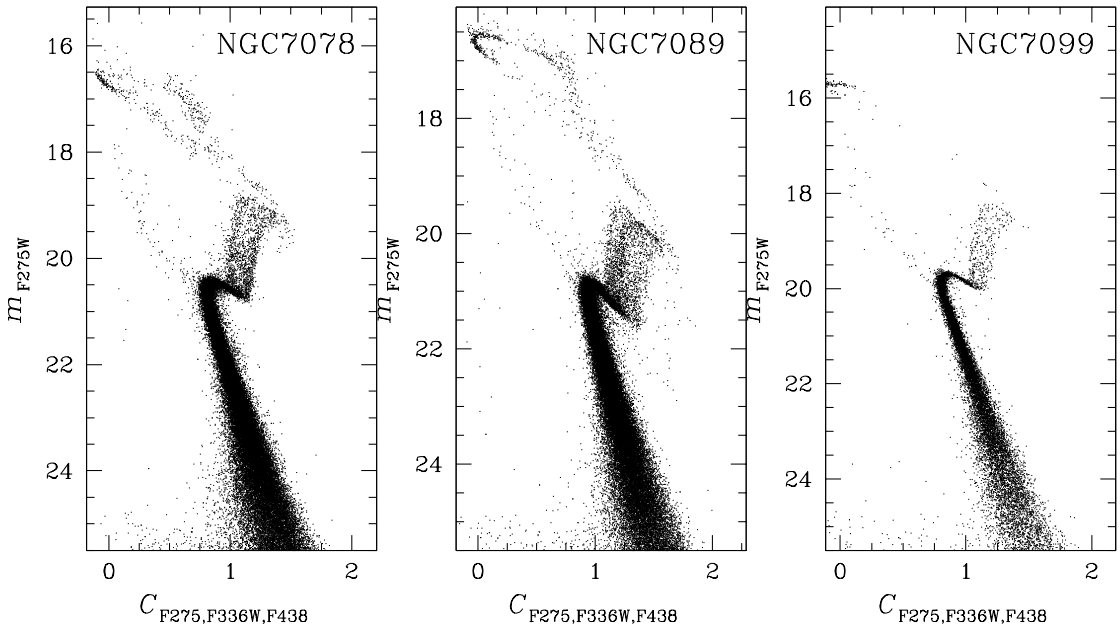


Figure 28: The $m_{F275W}$ versus $C_{F275W,F336W,F438W}$ pseudo-CMDs for NGC 7078, NGC 7089, and NGC 7099.

# 2

# MAIN SEQUENCE PHOTOMETRY IN OUTER REGIONS OF NGC 6752, NGC 6397 AND NGC 6121 (M 4)

If we exclude the very particular case of $\omega$ Cen, all the studies focused on the multiple stellar populations in the **main sequence** of globular clusters has been performed until now by using exclusively Hubble Space Telescope data. This Chapter, from the work by Nardiello et al. (2015a), is the prove that, using high-accuracy photometry and appropriate combinations of colors and magnitudes, it is possible to disentangle multiple populations in the main sequence of globular cluster also using ground-based data.

## 2.1 INTRODUCTION

In recent years, the discovery that the color-magnitude diagrams (CMDs) of many globular clusters (GCs) are made of multiple sequences has provided overwhelming proof that these stellar systems have experienced a complex star-formation history. The evidence that GCs host multiple stellar populations has reawakened interest in these objects both from the observational and theoretical point of view.

Multiple sequences have been observed over the entire CMD, from the main sequence (MS, e.g., Piotto et al. 2007) through the subgiant branch (SGB, e.g., Piotto et al. 2012) and from the SGB to the red giant branch (RGB, e.g., Marino et al. 2008), and even in the white dwarf cooling sequence (Bellini et al., 2013a).

Multiple populations along the RGB have been widely studied in a large number of GCs (e.g., Yong et al. 2008, Lee et al. 2009a, Monelli et al. 2013) using photometry from both ground-based facilities and from the Hubble Space Telescope (HST). In contrast, with the remarkable exception of $\omega$ Centauri (Sollima

et al. 2007, Bellini et al. 2009b), the investigation of multiple MSs has been carried out with HST only (e.g., Bedin et al. 2004, Piotto et al. 2007, Milone et al. 2012a and references therein, Bellini et al. 2013b).

We will exploit the FOcal Reducer and low dispersion Spectrograph 2 (FORS2), mounted at the Very Large Telescope (VLT) of the European Southern Observatory (ESO) to obtain accurate *U*,*B*,*V*,*I* photometry of MS stars in the outskirts of three nearby GCs, namely NGC 6121 (M 4), NGC 6397, and NGC 6752, and we aim to study their stellar populations.

The Chapter is organized as follows: in Section 2.2 we provide an overview of the three GCs we studied. The observations and data reduction are described in Section 2.3. The CMDs are analyzed in Section 2.4, where we also show evidence of bimodal MSs for stars in the outskirts of NGC 6121 and NGC 6752 and calculate the fraction of stars in each MS. In Section 2.5, we study the radial distribution of stellar populations in NGC 6752 and NGC 6121. In Section 2.6, we estimate the helium difference between the two stellar populations of NGC 6121 and NGC 6752. A summary follows in Section 2.7.

## 2.2 PROPERTIES OF THE TARGET GCS

Multiple stellar populations have been widely studied in the three GCs analyzed here. In this section, we summarize the observational scenario and provide useful information to interpret our observations.

### 2.2.1 *NGC 6121*

NGC 6121 is the closest GC ($d \sim 2.2$ kpc) and has intermediate metal abundance ([Fe/H]=$-1.16$ Harris 1996, 2010 edition).

The RGB stars of this cluster exhibit a large spread in the abundance distribution of some light-elements such as C, N, O, Na, and Al (Gratton, Quarta & Ortolani 1986; Brown, Wallerstein & Oke 1990; Drake, Smith & Suntzeff 1992; Smith & Briley 2005). There is evidence of a CN bimodality distribution and Na-O anticorrelation (e.g., Norris 1981; Ivans et al. 1999).

The distribution of sodium and oxygen is also bimodal. Sodium-rich (oxygen-poor) stars define a red sequence along the RGB in the $U$ versus $U-B$ CMD, while Na-poor stars populate a bluer RGB sequence (Marino et al. 2008). Further evidence of multiple sequences along the RGB of NGC 6121 are provided by Lee et al. (2009a) and Monelli et al. (2013). NGC 6121 has a bimodal HB, populated both on the blue and red side of the instability strip. The HB morphology of this cluster is closely connected with multiple stellar populations. Indeed, blue HB stars are all Na-rich and O-poor (hence belong to the second stellar generation), while red-HB stars have the same chemical composition as first-generation stars (Marino et al., 2011c).

### 2.2.2 *NGC 6397*

Located at a distance of 2.3 kpc, NGC 6397 is a very metal-poor GC ([Fe/H] $=-2.02$; Harris 1996, 2010 edition).

In the late 1970s, Bell, Dickens & Gustafsson (1979) already demonstrated that the RGB stars of this cluster show a spread in light-element abundance. NGC 6397 exhibits modest star-to-star variations of oxygen and sodium and a mild Na-O anticorrelation (e.g., Ramírez & Cohen 2002, Carretta et al. 2009b). Similar to NGC 6121, the distribution of sodium and oxygen is bimodal and the groups of Na-rich (O-poor) and Na-poor (O-rich) stars populate two distinct RGBs in the Strömgren $y$ versus $c_y$ index diagram (Lind et al. 2011).

The MS of NGC 6397 is also bimodal, but the small color separation between the two MSs can be detected only when appropriate filters (like the F225W, F336W from HST/WFC3) are used. Observations of the double MSs from multiwavelength HST photometry have been interpreted as two stellar populations with different light-element abundance and a modest helium variation of $\Delta Y \sim 0.01$ ( di Criscienzo, D'Antona & Ventura 2010, Milone et al. 2012a).

### 2.2.3 *NGC 6752*

NGC 6752 is a nearby metal-poor GC ($d = 4.0$ kpc, [Fe/H] $=-1.54$; Harris 1996, 2010 edition).

Since the 1980s spectroscopic data reported 'anomalies' in the light-element abundances of the RGB stars of this cluster (Norris et al. 1981, Cottrell & Da Costa 1981). More recent works confirm star-to-star light-element variations in NGC 6752 (Grundahl et al. 2002; Yong et al. 2003, 2008, 2013; Carretta et al. 2005), O-Na, Mg-Al, and C-N (anti)correlations for both unevolved (Gratton et al. 2001; Shen et al. 2010; Pancino et al. 2010) and RGB stars (Yong et al. 2005; Carretta et al. 2007, 2012) in close analogy with what was observed in most Galactic GCs (see e.g. Ramírez & Cohen 2002, Carretta et al. 2009b and references therein). In particular, there are three main groups of stars with different Na, O, N, Al, which populate three different RGBs when appropriate indices are used (like the $c_1$ and $c_y$ Stromgren indices or the $c_{U,B,I}$ visual index, Yong et al. 2008, 2003, Carretta et al. 2012, Monelli et al. 2013).

As shown by Milone et al. (2013, hereafter Mi13), the CMD of NGC 6752 is made of three distinct sequences that can be followed continuously from the MS to the SGB and from the SGB to the RGB. These sequences correspond to three stellar populations with different light-element and helium abundance.

## 2.3 OBSERVATIONS AND DATA REDUCTION

We used $2 \times 2$ binned images taken with the ESO/FORS2 ($2 \times 2k \times 4k$ MIT CCDs) mounted at the VLT, using the standard resolution collimator. With this configuration, the field of view of FORS2 is reduced to $\sim 6.8 \times 6.8$ arcmin$^2$ by the MOS unit in the focal plane and the pixel scale is $\sim 0.25$ arcsec/pixel. The dithered images of NGC 6121, NGC 6397, and NGC 6752 were acquired using u_HIGH, b_HIGH, v_HIGH, and I_Bessel broadband filters between April 14, 2012 and July 23, 2012. A detailed log of observations is reported in Table 2. Figures 29, 30, and 31 show the combined field of view for each cluster.

We used a modified version of the software described in Anderson et al. (2006) to reduce the data. Briefly, for each image we obtained a grid of 18 empirical point spread functions (PSFs, an array of $3 \times 3$ PSFs for each chip of FORS2) that vary spatially, using the most isolated, bright and not saturated stars. In this way, each pixel of the image corresponds to a PSF that is a bilinear interpolation of the closest four PSFs of the grid. This makes it possible to measure star positions and fluxes in each individual exposure using an appropriate PSF and

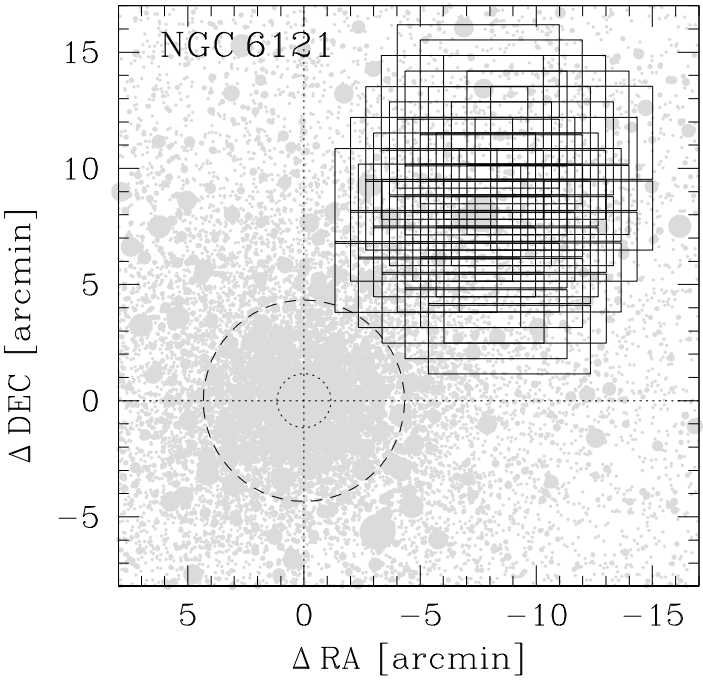


Figure 29: Dither pattern of the FORS2 images taken in the fields of NGC 6121. The dotted, dashed, and dashed-dotted circles indicate the core, half-light, and tidal radius of the three GCs.

to obtain a catalog of stars for each frame. We registered, for each cluster and for each filter, all star positions and magnitudes of each catalog into a common frame (master-frame) using linear transformations. The final result is a list of stars (master list) for each cluster. We plot in Fig. 32 the rms of the photometric residual and of the position as a function of the mean magnitude for each filter and each star measured in NGC 6121. In the case of NGC 6752 and NGC 6397, the distributions are similar.

We specify here that we used magnitude to express the luminosities of the stars under study.

We noted that all the CMDs of the three GCs showed unusually spread out sequences (see panel (a) of Fig. 33 for an example of the $V$ versus $U-V$ CMD of NGC 6397). Part of this spread is due to differential reddening, but this is not the only cause. In fact, we found that by selecting stars in different regions of the master list, we obtained shifted MSs. As an example, in panel (d) of Fig. 33, we show the variation of the color $\Delta(U-V)$ for NGC 6397. This plot shows

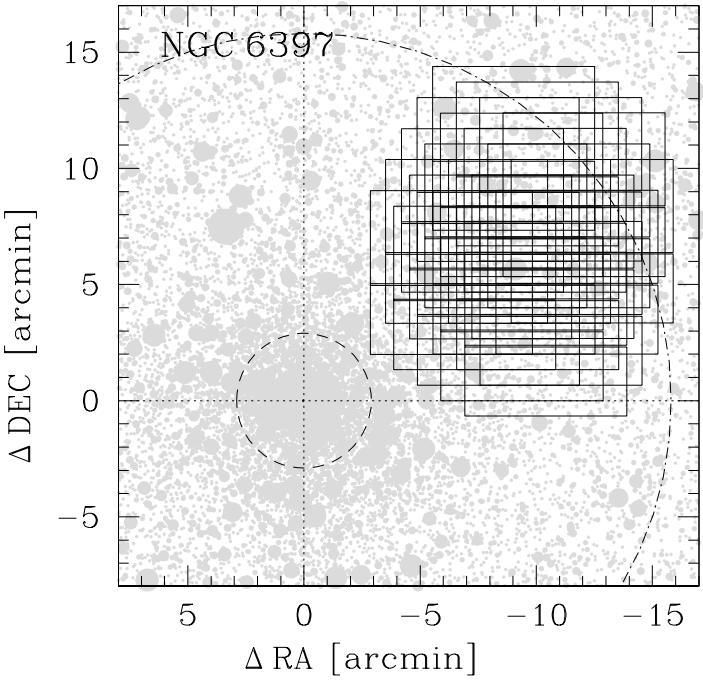


Figure 30: As in Fig. 29, but for NGC 6397, a post-core-collapse cluster.

that there is an important gradient of $\Delta(U-V)$ along the x-axis. We selected two groups of stars in this plot : the stars with $x > 1050$ and those with $x < 1050$. We plotted these two subsamples in the $V$ versus $U-V$ CMDs, in black crosses ($x > 1050$) and red circles ($x < 1050$) respectively: panel (a) of Fig. 33 shows the result. The two groups form two shifted MSs. This effect is present in all the CMD of the three GCs, even when they have different extent levels.

Freudling et al. (2007) showed that there is an illumination gradient in the FORS2 flats produced by the twilight sky. This gradient changes with time and with the position of the Sun relative to the pointing of the telescope and could produce a photometric zero-point variation across the FORS2 detectors. The illumination gradient in the flat fields could contribute to the observed enlargement of the CMDs.

We obtained star fluxes using local sky values, and therefore it is expected that these systematic effects are negligible. If the gradient in the flat field images is not properly removed during the prereduction procedure, the pixel quantum efficiency correction will be wrong. The consequence is that the luminosity of a star measured in a given location of the CCD will be underestimated

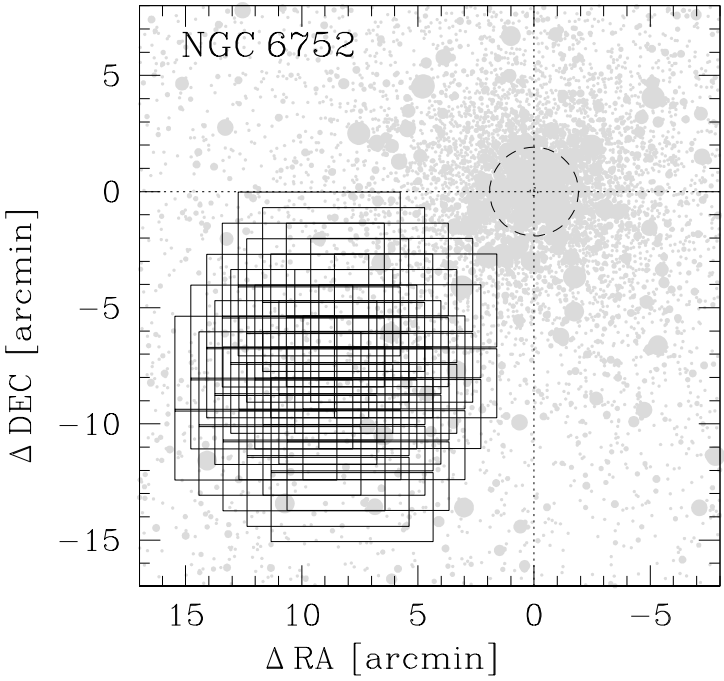


Figure 31: As in Fig. 29, but for NGC 6752, a post-core-collapse cluster.

(or overestimated) with respect to the luminosity of the same star measured in another location of the CCD.

Using the measured star positions and fluxes, we performed a similar correction to that described by Bellini et al. (2009a). The correction is a self-consistent, autocalibration of the illumination map and takes advantage of the fact that the images are well dithered.

For each cluster and for each filter, the best image (characterized by lower airmass and best seeing) is defined as reference frame. We considered the measured raw magnitude $m_{ij}$ of each star $i$ in each image $j$. Using common stars between the image $j$ and the reference frame we computed the average magnitude shift

$$\Delta_j = \frac{1}{M} \sum_{i=1}^{M} (m_{ij} - m_{i,\mathrm{ref}})$$

| Filter | Exp. time | Airmass ($\sec z$) | Seeing (arcsec) |
|---|---|---|---|
| | **NGC 6121** | | |
| u_HIGH | $25 \times 410$ s | 1.004–1.104 | 0.58–0.90 |
| b_HIGH | $25 \times 200$ s | 1.007–1.113 | 0.71–1.20 |
| v_HIGH | $25 \times 52$ s | 1.118–1.251 | 0.70–1.21 |
| I_BESS | $25 \times 30$ s | 1.036–1.150 | 0.56–1.03 |
| | **NGC 6397** | | |
| u_HIGH | $25 \times 410$ s | 1.153–1.452 | 0.81–1.09 |
| b_HIGH | $35 \times 200$ s | 1.144–1.599 | 0.73–1.52 |
| v_HIGH | $50 \times 52$ s | 1.142–1.272 | 0.82–1.23 |
| I_BESS | $25 \times 30$ s | 1.251–1.355 | 0.70–1.21 |
| | **NGC 6752** | | |
| u_HIGH | $25 \times 410$ s | 1.227–1.416 | 0.67–1.30 |
| b_HIGH | $33 \times 200$ s | 1.227–1.850 | 0.49–1.36 |
| v_HIGH | $25 \times 52$ s | 1.367–1.483 | 0.68–0.86 |
| I_BESS | $25 \times 30$ s | 1.293–1.363 | 0.50–0.77 |

Table 2: Log of observations

where M is the number of stars in common between the reference frame and the single image $j$. For each star that is centered in a different pixel in each dithered frame, we computed its average magnitude in the reference system

$$\bar{m} = \frac{1}{N} \sum_{j=1}^{N} (m_{ij} - \Delta_j)$$

where $N$ is the number of images in which the star appears. Then we computed the residual:

$$\delta_{ij} = m_{ij} - \Delta_j - \bar{m}_j \,.$$

We divided each FORS2 chip in a spatial grid of $10 \times 10$ boxes, and, for each box, we computed the average of the residuals from the stars located in that region in each single image. This provides a first spatial correction to our photometry. To obtain the best correction, we iterate until the residual average becomes smaller than 1 mmag. To guarantee convergence, we applied half of the correction calculated in each box for each star. Moreover, to obtain the best correction at any location of the camera, we computed a bilinear interpolation of the closest four grid points. At the edges of the detectors the correction is less efficient because

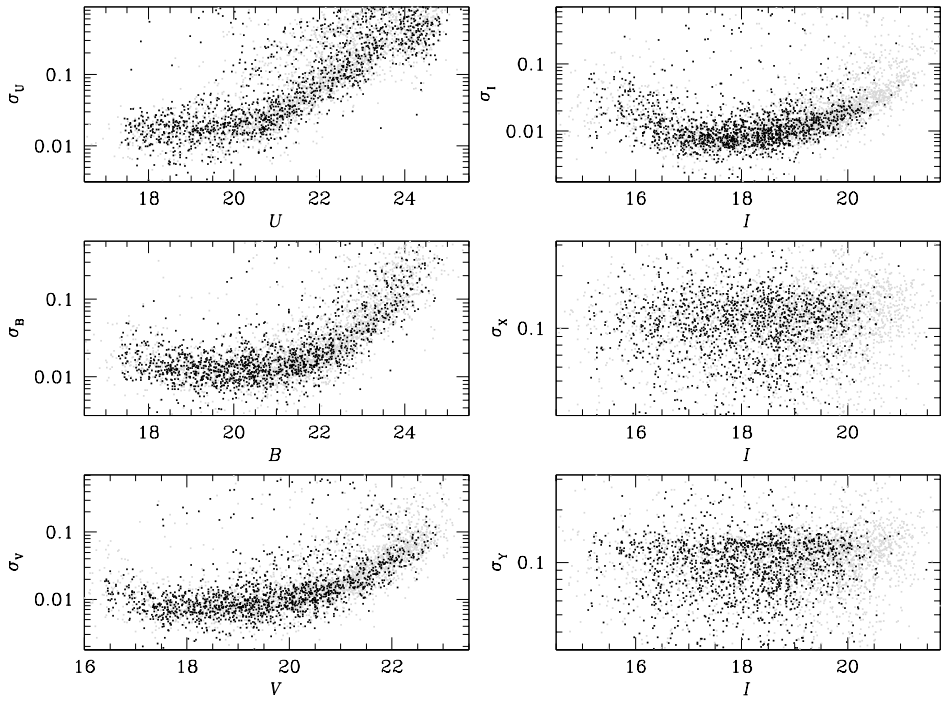


Figure 32: Photometric (left panels and top right panel) and position residuals (middle and bottom right panels) from single measurements in the single images of NGC 6121 plotted as a function of the average magnitude. Gray points show all detected stars; black points refer to proper motion selected stars. In the case of NGC 6752 and NGC 6397, the distributions are similar.

the corresponding grid points have been moved toward the external borders of the grid to allow the bilinear interpolation to be computed all across the CCDs. In panel (e) of Fig. 33, we show our final correction grid for the v_HIGH filter.

The final correction grids are different for each filter and for each set of images. In particular as well as the size of the zero-point variations, the patterns are different from filter to filter. This quantity also changes using different data sets. The maximum amplitudes of our corrections are tabulated in Table 2.

We corrected the spread of the CMD due to differential reddening using the procedure as described by Milone et al. (2012b). Briefly, we defined a fiducial line for the MS of the cluster. Then, for each star, we considered a set of neighbors (usually 30, selected anew for each filter combination) and estimated the median offset relative to the fiducial sequence. These systematic color and magnitude offsets, measured along the reddening line, represent an estimate of

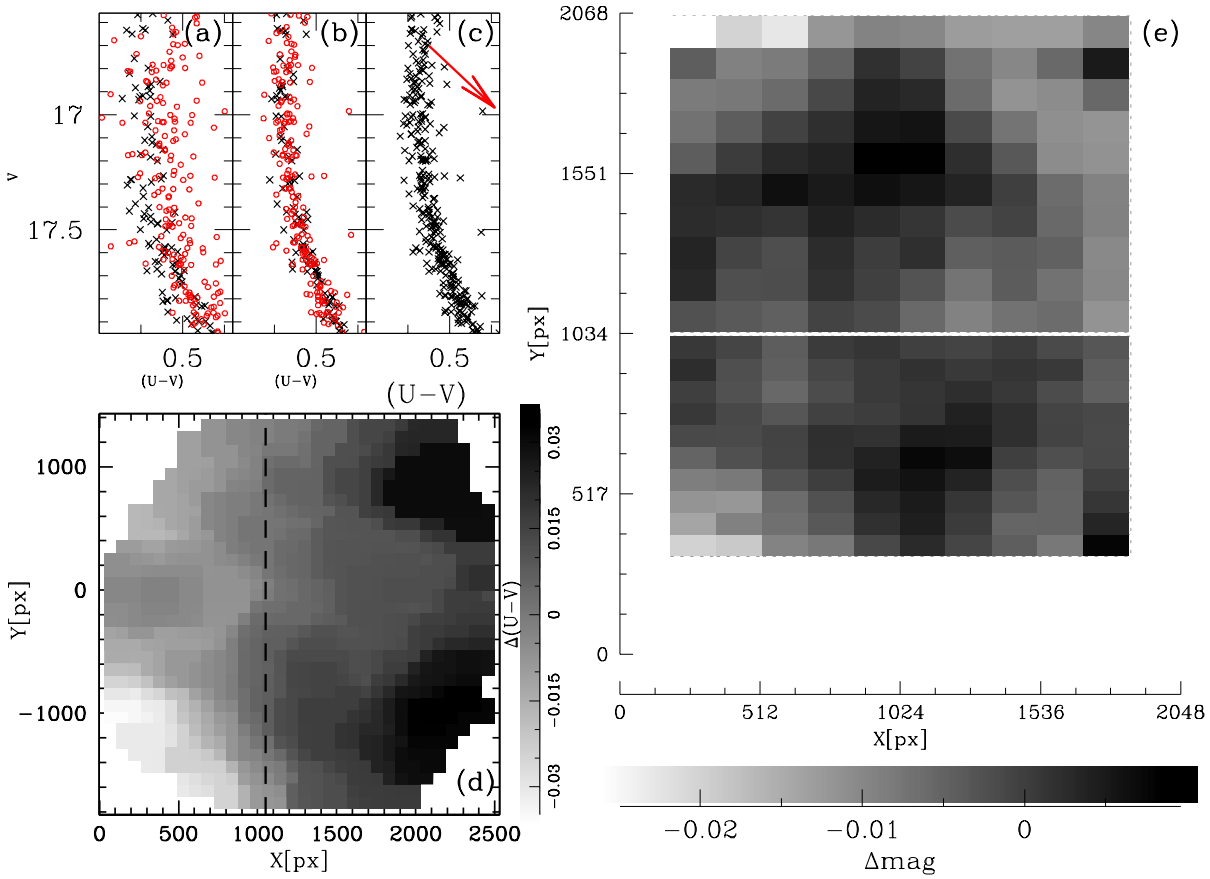


Figure 33: Visualization of the effects of the photometric zero-point variation. Panel (a): CMDs zoomed into the MS region of NGC 6397 before the zero-point correction; panel (b): CMD after the zero-point correction; panel (c): CMD after the differential reddening correction (in red the reddening vector, scaled by a factor 1/3) ; panel (d) map of the color zero-point variation; the dashed line divide the two groups of stars shown in the panels (a) and (b); panel (e): final Δmag correction grid for the filter v_HIGH and the NGC 6397 data set.

| **Filter** | **Δmag** | | |
|---|---|---|---|
| | **NGC 6121** | **NGC 6397** | **NGC 6752** |
| u_HIGH | 0.11 | 0.13 | 0.09 |
| b_HIGH | 0.04 | 0.05 | 0.03 |
| v_HIGH | 0.12 | 0.04 | 0.06 |
| I_BESS | 0.04 | 0.04 | 0.04 |

Table 3: Maximum amplitudes of photometric zero-point corrections.

the local differential reddening. With this procedure, we also mitigated the photometric zero-point residuals left by the illumination correction (especially close to the corners of the field of view). Panel (c) of Fig. 33 shows the CMD after all the corrections are applied.

The photometric calibration of FORS2 data for $UBV$ Johnson and $I_C$ Cousins bands was obtained using the photometric Secondary Standards star catalog by Stetson (2000). We matched our final catalogs to the Stetson standard stars, and derived calibration equations by means of least squares fitting of straight lines using magnitudes and colors.

### 2.3.1 *Proper motions*

Since NGC 6121 (l,b=350°.97,15°.97) and NGC 6397 (l,b=338°.17;−11°.96) are projected at low Galactic latitude, their CMDs are both dramatically contaminated by disk and bulge stars, in contrast to NGC 6752 (l,b=336°.49; −25°.63) which presents low-field contamination. The average proper motions of NGC 6121, NGC 6397 and NGC 6752 strongly differ from those of these field stars (e.g., Bedin et al. 2003, Milone et al. 2006). Therefore, to minimize the contamination from field stars, we identified cluster members on the basis of stellar proper motions.

In order to get information on the cluster membership, we estimated the displacement between the stellar positions obtained from our FORS2 data set and those in the ground-based data taken from the image archive maintained by Stetson (2000) and also used in Monelli et al. (2013). These observations include images from different observing runs with the Max Planck 2.2m telescope, the CTIO 4m, 1.5m and 0.9m telescopes, and the Dutch 0.9m telescope on La Silla.

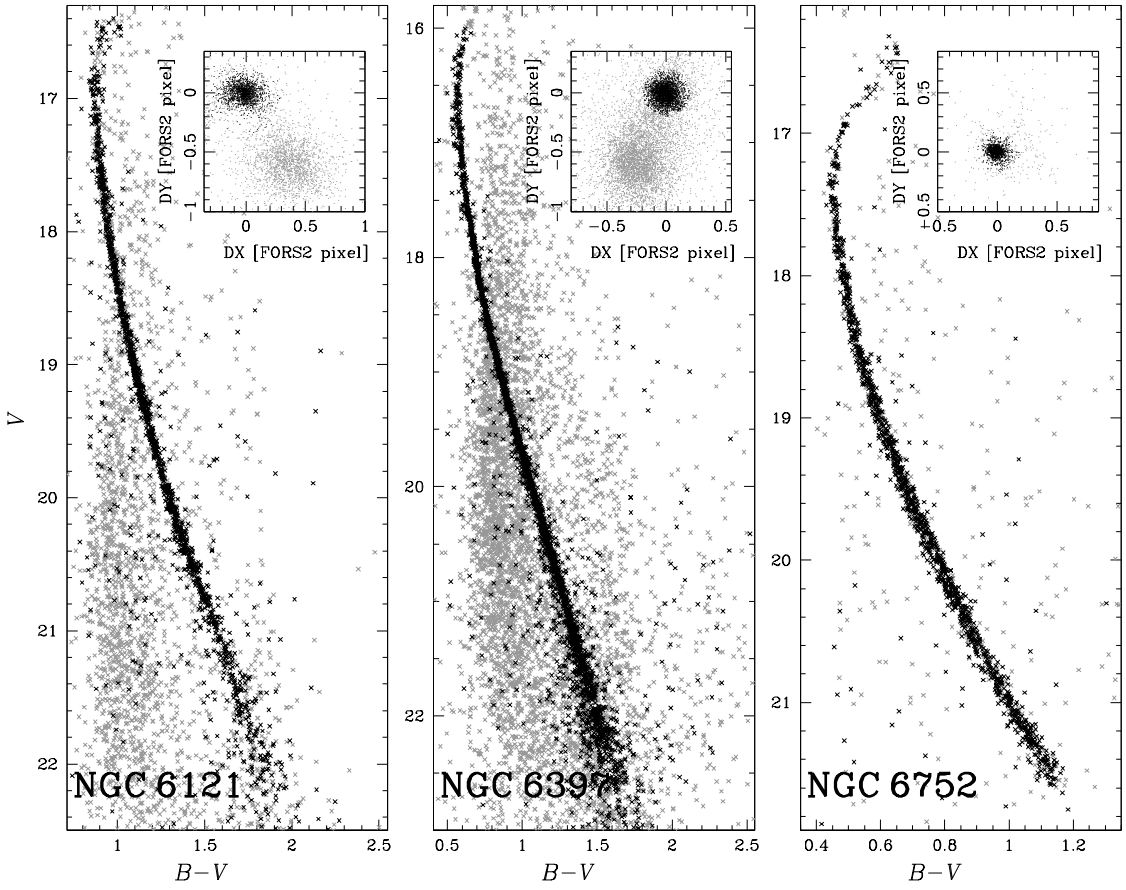


Figure 34: The $V$ versus $B-V$ CMD of stars in the field of view of NGC 6121 (left), NGC 6397 (middle), and NGC 6752 (right). The insets show the vector-point diagram of stellar displacements along the X and Y direction. Black and gray points indicate stars that, according to their proper motions, are considered cluster members and field stars, respectively (see text for details).

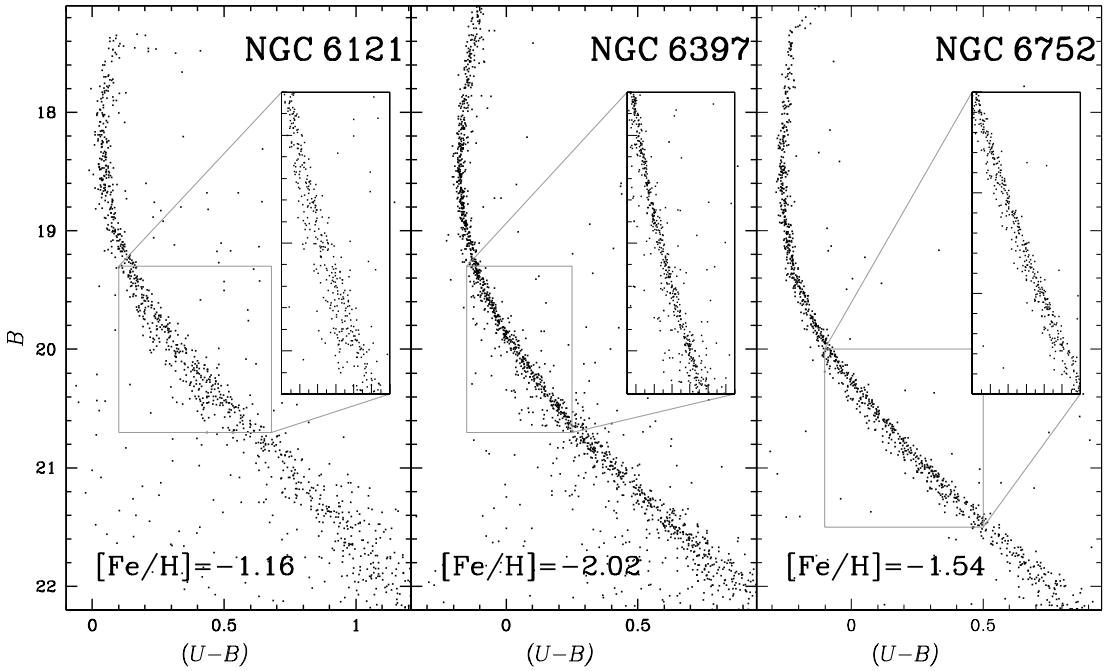


Figure 35: The $B$ versus $(U-B)$ CMD for NGC 6121 (left), NGC 6397 (middle), and NGC 6752 (right). The inset is a zoom around the upper MS. The CMDs only show the cluster members and are corrected by zero-point variations and differential reddening.

To obtain the displacement, we used six-parameter local transformations based on a sample of likely cluster members in close analogy to what was done by Bedin et al. (2003) and Anderson et al. (2006) to calculate stellar proper motions.

The results are shown in Fig. 55. The figure shows the $V$ versus $B-V$ CMDs for NGC 6121, NGC 6397, and NGC 6752. The insets show the vector-point diagrams of the stellar displacements for the same stars shown in the CMDs: the cluster-field separation is evident. Likely cluster members are plotted in black both in the CMDs and in the vector-point diagrams, and in gray the rejected stars.

## 2.4 THE CMDS OF THE THREE GCS

Previous studies on multiple stellar populations have demonstrated that the $U-B$ color is very efficient in detecting multiple RGBs (see Marino et al. 2008

and Milone et al. 2010 for the cases of NGC 6121 and NGC 6752), and multiple MSs (see Milone et al. 2012b, Mi13 for the cases of NGC 6397 and NGC 6752). As discussed by Sbordone et al. (2011), CNO abundance variations affect wavelengths shorter than $\sim 400$ nm, owing to the rise of molecular absorption bands in cooler atmospheres. The consequences are that the CMDs in $UB$ filters show enlarged sequences, mainly because of variations in the N abundance, with the largest variations affecting the RGB and the lower MS.

Motivated by these results, we started our analysis from the $B$ versus $U-B$ CMDs shown in Fig. 35; the inset of each panel is a zoom-in of the upper MS between $\sim 1.5$ and $\sim 2.5$ magnitudes below the turn off (TO).

A visual inspection at these CMDs reveals that the color broadening of MS stars in both NGC 6121 and NGC 6752 is larger than that of NGC 6397. A small fraction of MS stars in NGC 6121 and NGC 6752 defines an additional sequence on the blue side of the most populous MS.

To investigate whether the widening of the MSs is due to the presence of multiple populations, we identified in the $B$ versus $U-B$ CMD of each cluster two groups of red-MS (rMS) and blue-MS (bMS) stars, as shown in panels (a) of Fig. 36. We colored the two MSs in red and blue, respectively, and these colors are used consistently hereafter. In the case of NGC 6121 and NGC 6752, where there is some hint of a split MS, we identified by eye the fiducial that divide the rMS and bMS. In the case of NGC 6397, we have considered rMS (or bMS) as the stars that are redder (or bluer) than the MS fiducial line. Each inset shows the color distribution of $\Delta(U-B)$ for the two MSs, where $\Delta(U-B)$ is obtained by subtracting the color of the fiducial that divide the two MSs to the color of the rMS and bMS stars. In the cases of NGC 6121 and NGC 6752, the color distributions show a double peak that could be due to the presence of two populations; we fitted them with a sum of Gaussians (in red and blue for the rMS and bMS, respectively). We applied a moving box procedure to further verify that the distribution of $\Delta(U-B)$ in the case of NGC6121 is bimodal. We changed the bin size, ranging from 0.005 to 0.02 (approximately the error in color) with steps of 0.001. Furthermore, from our data set we determined a kernel-density distribution by assuming a Gaussian kernel with $\sigma$ =0.02 mag. In all cases, we consistently found that the distribution can only be reproduced by two Gaussians.

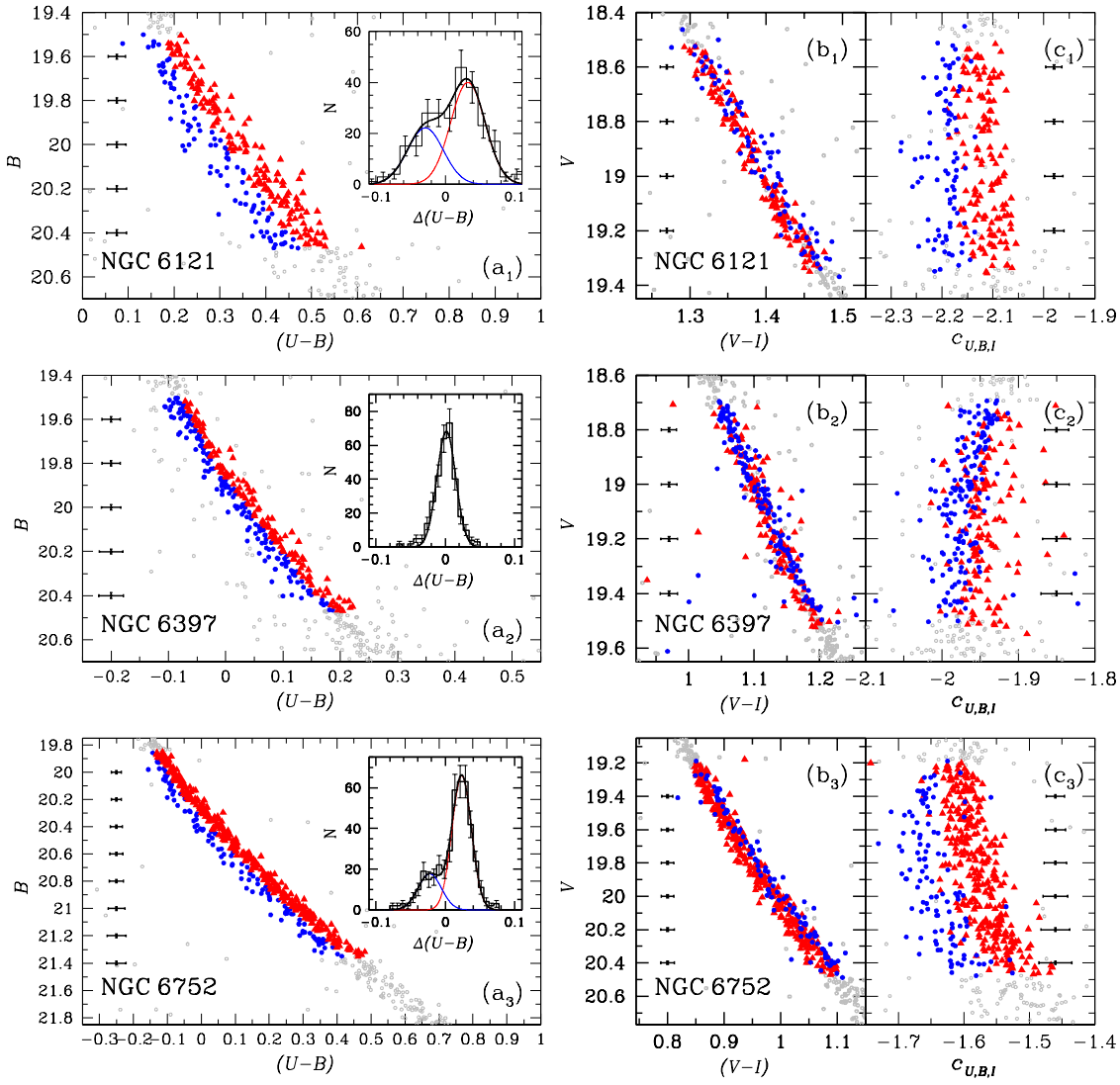


Figure 36: Comparison between the $B$ vs. $U-B$ (panels a), the $V$ vs. $V-I$ (panels b) and $V$ vs $c_{U,B,I}$ (panels c) CMDs of NGC 6121 (up), NGC 6397 (middle) and NGC 6752 (down). Red triangles and blue points represent the groups of rMS and bMS stars defined in panels (a). The insets of panels (a) show the $\Delta(U-B)$ distributions, fitted with a bi-gaussian in the case of NGC 6121 and NGC 6752 and with a Gaussian in the case of NGC 6397. The horizontal bars show the mean error in color.

A multiple sequence in NGC 6752 had already been identified by Mi13 using HST data. Very recently, we had the first F275W, F336W, F438W WFC3 images of NGC 6121 from the HST GO-13297 UV Large Legacy Program (P.I. Piotto). Even a preliminary reduction of the data shows a clear separation of the MS into two branches in the F438W vs F336W-F438W CMD, fully confirming what we anticipate here in the equivalent, groundbased $U$ vs $U-B$ diagram of Fig. 36. In the case of NGC 6397, it is possible to fit the distribution with a single Gaussian.

As an additional check for the presence of multiple populations, we investigated whether the widening of the MSs of all the GCs is intrinsic or if it is entirely due to photometric errors. We have compared two CMDs, $B$ versus $U-B$ with $V$ versus $V-I$, obtained using independent data sets. We considered the rMS and bMS defined previously: if the color spread is entirely due to photometric errors, a star that is red (or blue) in the $B$ versus $U-B$ CMD will have the same chance of being either red or blue in the $V$ vs $V-I$ CMD. By contrast, the fact that the two sequences identified in the first CMD have systematically different colors in the second CMD would be a proof that the color broadening of the MS is intrinsic. In panels (b) of Fig. 36 we plotted the rMS and bMS in $V$ versus $V-I$ CMDs. The fact that the rMS stars of both NGC 6121 and NGC 6752 have, on average, different $V-I$ than bMS stars demonstrates that the color broadening of their MS in the $U$ versus $U-B$ CMDs is intrinsic. This is the first evidence that the MS of NGC 6121 is not consistent with a simple stellar population. In the case of NGC 6397, rMS and bMS stars share almost the same $V-I$ thus suggesting that most of the colors broadening is due to photometric errors.

As a last test, we plotted the two MSs in the $V$ versus $c_{U,B,I}$ CMD. The $c_{U,B,I}$ index, which is defined as the color difference $(U-B)-(B-I)$, is a very efficient tool to identify multiple sequences in GCs. Indeed, it maximizes the color separation between the stellar populations that is due to both helium and light-element variations (Monelli et al. 2013). Panels (c) of Fig. 36 confirm the previous results: rMS and bMS of NGC 6121 and NGC 6752 are well defined in the $V$ versus $c_{U,B,I}$ CMDs, but this is less evident for NGC 6397.

As a last proof, we plotted in Figures 37, 38, and 39 the $(U-B)$ versus $(V-I)$ diagrams for each cluster: the rMS and bMS are plotted in red and blue as defined previously. The figure shows that for both NGC 6121 and NGC 6752

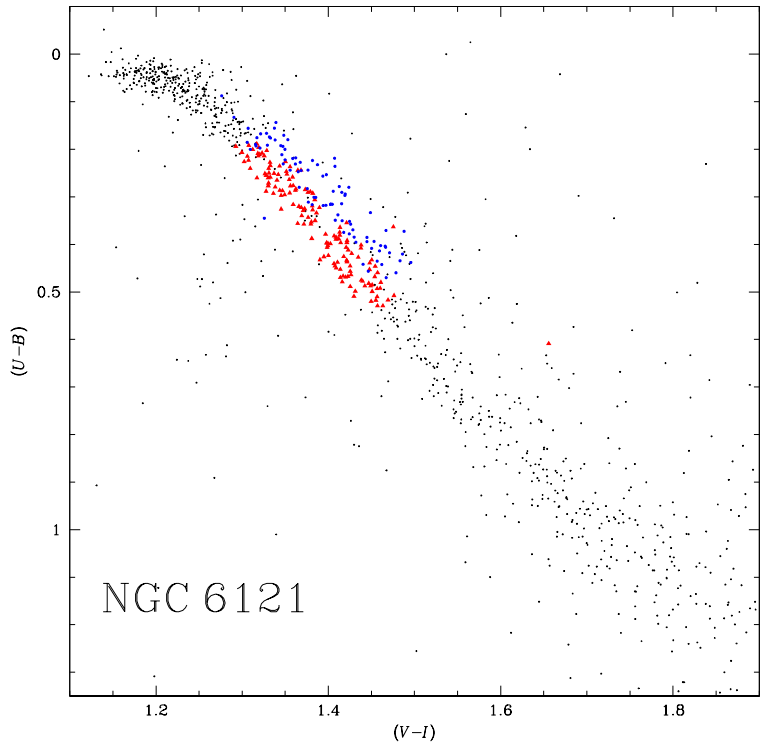


Figure 37: Color-color diagrams for NGC 6121. In red (triangles) and blue (dots) we show the rMS and bMS as defined in Fig. 36

the two MSs are well defined, while for NGC 6397 the rMS and bMS stars are mixed.

Figure 40 shows the $V$ versus $c_{U,B,I}$ diagram for the three GCs under study here. In their analysis of multiple stellar populations in 22 GCs, Monelli et al. (2013) found that all the analyzed clusters show a multimodal or spread RGB in the $V$ versus $c_{U,B,I}$ diagram, and the $c_{U,B,I}$ value of each star depends on its light-element abundance. The $c_{U,B,I}$-index width of the RGB ($W_{\rm RGB}$) correlates with the cluster metallicity, with the more metal rich GCs also having the largest values of $W_{\rm RGB}$. In order to compare the MSs of the three GCs we studied, we introduce a quantity, $W_{\rm MS}$, which is akin to $W_{\rm RGB}$, but is indicative of the $c_{U,B,I}$-index broadening of the MS. The procedure to determine $W_{\rm MS}$ is illustrated in Fig. 41 for NGC 6121 and is the same for the other clusters. We have considered the magnitude of the TOs as magnitude of reference: $V_{\rm MSTO} \sim 16.6$ in the case of NGC 6397, $V_{\rm MSTO} \sim 17.4$ for NGC 6752, and $V_{\rm MSTO} \sim 16.75$ for NGC 6121. Panel (a) of Fig. 41 shows the $V$ versus $c_{U,B,I}$ diagram for NGC 6121 in a range of magnitudes from $V_{MSTO} - 0.5$ to $V_{MSTO} + 5$ . In this range of magnitudes, we obtained the fiducial line for the MSs computing the $3.5\sigma$-clipped median of

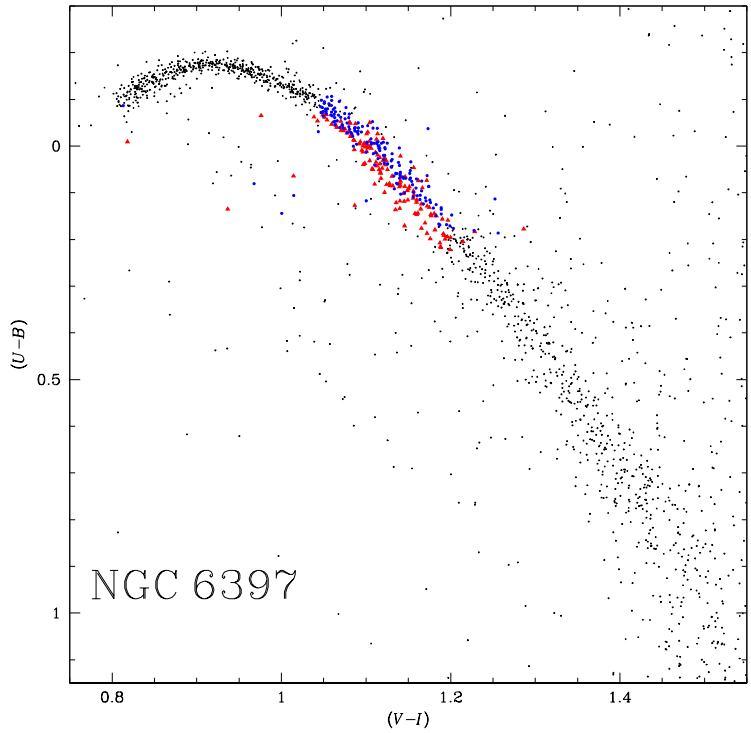


Figure 38: Color-color diagrams for NGC 6397. In red (triangles) and blue (dots) we show the rMS and bMS as defined in Fig. 36

the color in the interval of 0.35 mag and interpolated these points with a spline. In our analysis, we only used MS stars with $2 < V - V_{\rm MSTO} < 2.5$, where the MS split is visible for both NGC 6121 and NGC 6752. This magnitude interval is delimited by the two dashed lines of Fig. 41a. The thick line is the fiducial in the considered magnitude interval. The verticalized $V$ versus $\Delta c_{U,B,I}$ diagrams is plotted in panel (b) of Fig. 41, while panel (c) shows the histogram distribution of $\Delta c_{U,B,I}$. The MS width, $W_{\rm MS}$, is defined as the $\Delta c_{U,B,I}$ extension of the histogram and is obtained by rejecting the 5% of the reddest and the bluest stars on the extreme sides. To account for photometric error, we have subtracted from the observed $W_{\rm MS,OBS}$ the average error in $c_{U,B,I}$ in the same magnitude interval, i.e., $W_{\rm MS} = \sqrt{W^2_{\rm MS,OBS} - \sigma^2_{c_{U,B,I}}}$. We found that the most metal-rich GC, NGC 6121, exhibits the largest $c_{U,B,I}$ index width for MS stars ($W_{\rm MS} = 0.169 \pm 0.014$).
The spread in $c_{U,B,I}$ is smaller in the case of NGC 6752 ($W_{\rm MS} = 0.115 \pm 0.006$) and drops down to $W_{\rm MS} = 0.093 \pm 0.014$ in the most metal-poor GC NGC 6397. To estimate the statistical uncertainty in measuring $W_{\rm MS}$, we used the bootstrap resampling of the data to generate 10000 samples drawn from the original data sets. We computed the standard deviation from the mean of the simulated $W_{\rm MS}$ and adopted this as the uncertainty of the observed $W_{\rm MS}$.

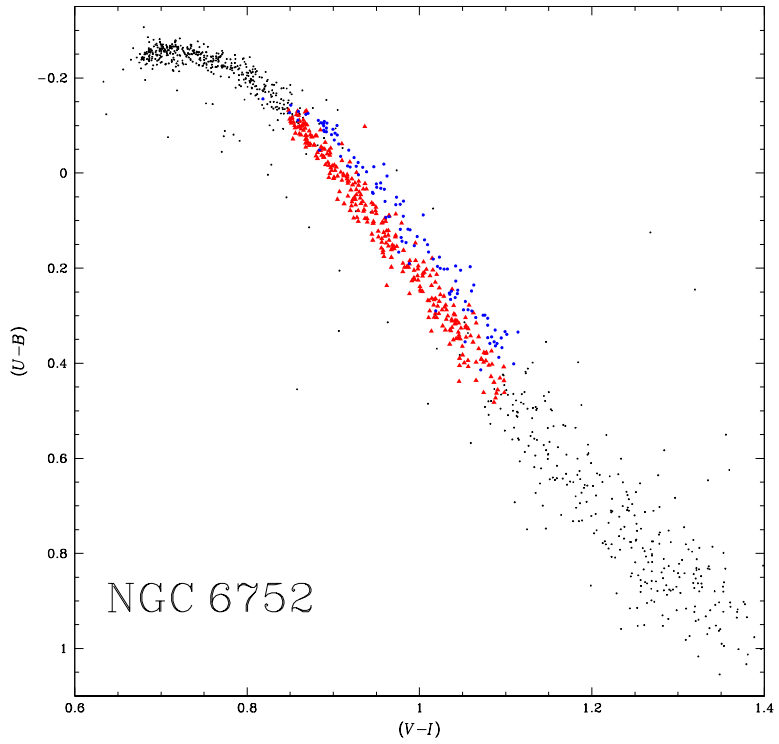


Figure 39: Color-color diagrams for NGC 6752. In red (triangles) and blue (dots) we show the rMS and bMS as defined in Fig. 36

These findings make it tempting to speculate that the $c_{U,B,I}$ index width of the MS could be correlated with the cluster metallicity in close analogy with what we observed for RGB stars. An analysis of a large sample of GCs is mandatory to infer any conclusion on the relation between $W_{\rm MS}$ and [Fe/H].

Milone et al. (2013) have identified three stellar populations in NGC 6752 that they have named 'a', 'b', and 'c'. Population 'a' has a chemical composition similar to field halo stars of the same metallicity, population 'c' is enhanced in sodium and nitrogen, depleted in carbon and oxygen and enhanced in helium ($\Delta Y$ $\sim$0.03), while population 'b' has an intermediate chemical composition between 'a' and 'c' and is slightly helium enhanced ($\Delta Y$ $\sim$0.01). However, the MSs of populations 'b' and 'c' are nearly coincident in the $m_{\rm F336W}$ versus $m_{\rm F336W} - m_{\rm F390W}$ CMD, while population 'a' stars have bluer $m_{\rm F336W} - m_{\rm F390W}$ colors (Mi13, see their Fig. 8). The three MSs also exhibit a similar behavior in the $m_{\rm F336W} - m_{\rm F410M}$ and $m_{\rm F336W} - m_{\rm F467M}$ colors. Since these colors are similar to $U - B$, the less populous MS identified in this work should correspond to the population 'a' identified by Mi13, while the rMS hosts both population 'b' and population 'c' stars.

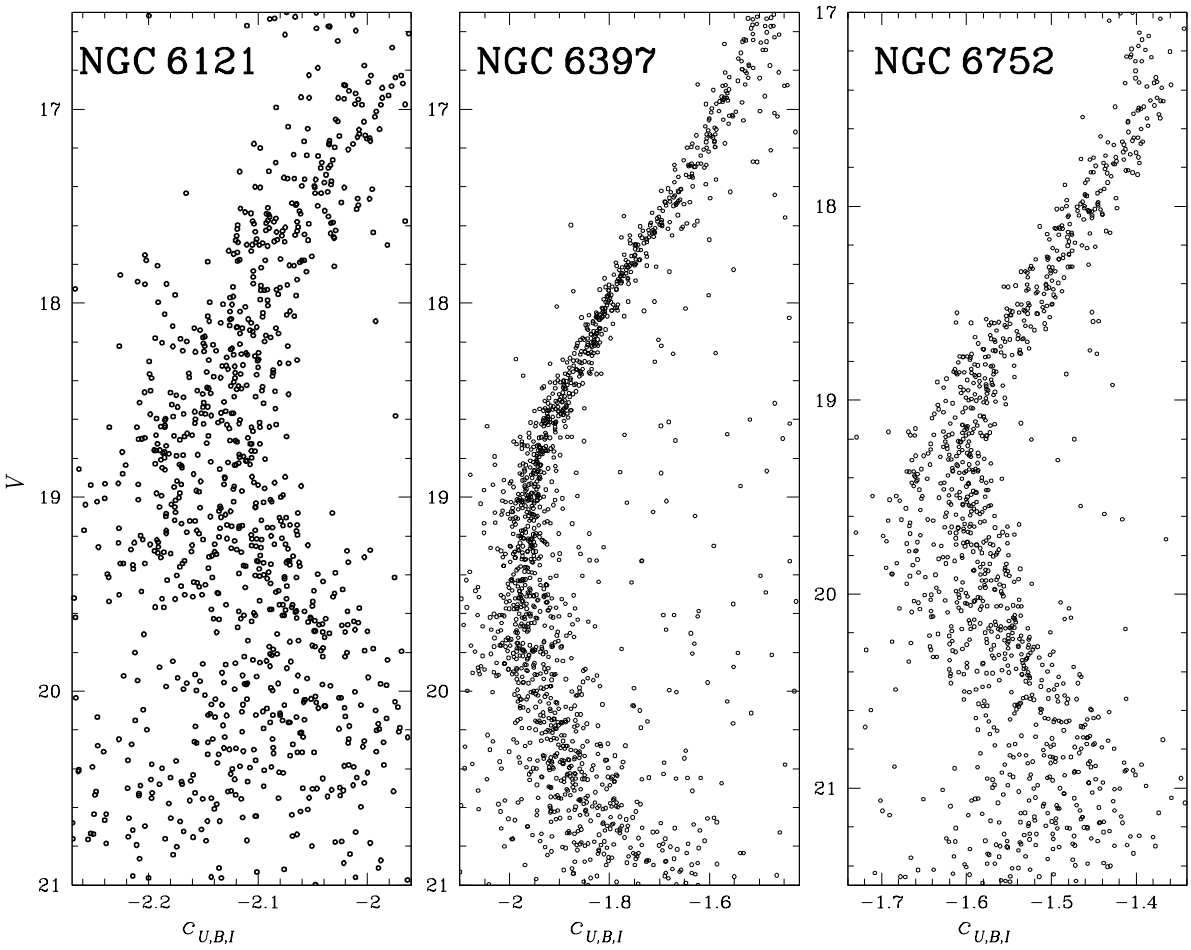


Figure 40: $V$, $c_{U,B,I}$ diagrams for NGC 6121 (left), NGC 6397 (middle), and NGC 6752 (right).

### 2.4.1 *The fraction of rMS and bMS in NGC 6121 and NGC 6752*

In order to measure the fraction of stars in each MS, we followed the procedure illustrated in Fig. 42 for NGC 6752, which our group already used in several previous works (e.g., Piotto et al. 2007, Mi13).

Panel (a) shows the $V$ versus $c_{U,B,I}$ CMD of the MS stars in the magnitude interval $19.25 < V < 20.55$, where the MS split is most evident. We verticalized the selected MS by subtracting the color of the stars to the color of the fiducial line of the rMS, obtaining $\Delta c_{U,B,I}$. The fiducial line is obtained by hand selecting the stars of the rMS, dividing them in bins of magnitude, computing the median colors of the stars within each bin, and interpolating these

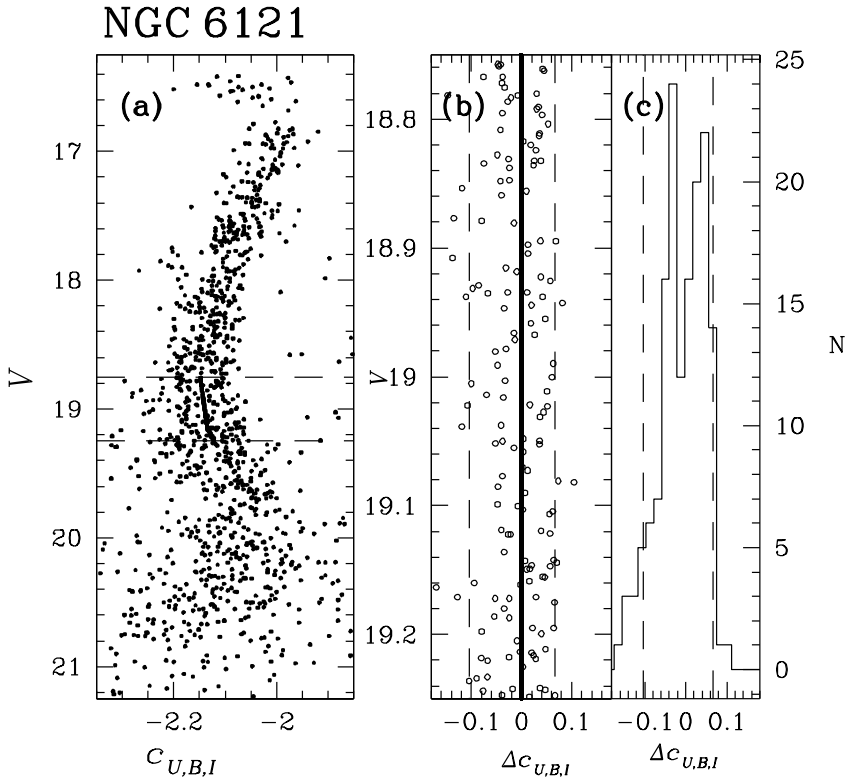


Figure 41: Procedure to estimate the MS width for NGC 6121. Panel (a) shows the $V$ versus $c_{U,B,I}$ CMD of NGC 6121. The thick line is the MS fiducial line (see text for details). Panel (b) shows the verticalized MS between the two dashed lines of panel (a). Panel (c) is the distribution of the color for the stars of panel (b).

median points with a spline. The verticalized $V$ versus $\Delta c_{U,B,I}$ diagram is plotted in panel (b).

The $\Delta c_{U,B,I}$ color distribution of the stars for three magnitude intervals is shown in panels (c). Each histogram clearly shows two peaks and has been simultaneously fitted with a double Gaussian, whose single components are shown in blue and red for the bMS and the rMS, respectively.

For each magnitude interval, we infer the fraction of bMS and rMS stars from the area under the Gaussians. The errors ($\sigma$) associated with the fraction of stars are estimated as $\sigma = \sqrt{\sigma_{\rm I}^2 + \sigma_{\rm II}^2}$, where $\sigma_{\rm I}$ is derived from binomial statistics and $\sigma_{\rm II}$ is the uncertainty introduced by the histogram binning and is derived as in Libralato et al. (2014). Briefly, we have derived $N$ times the population ratio

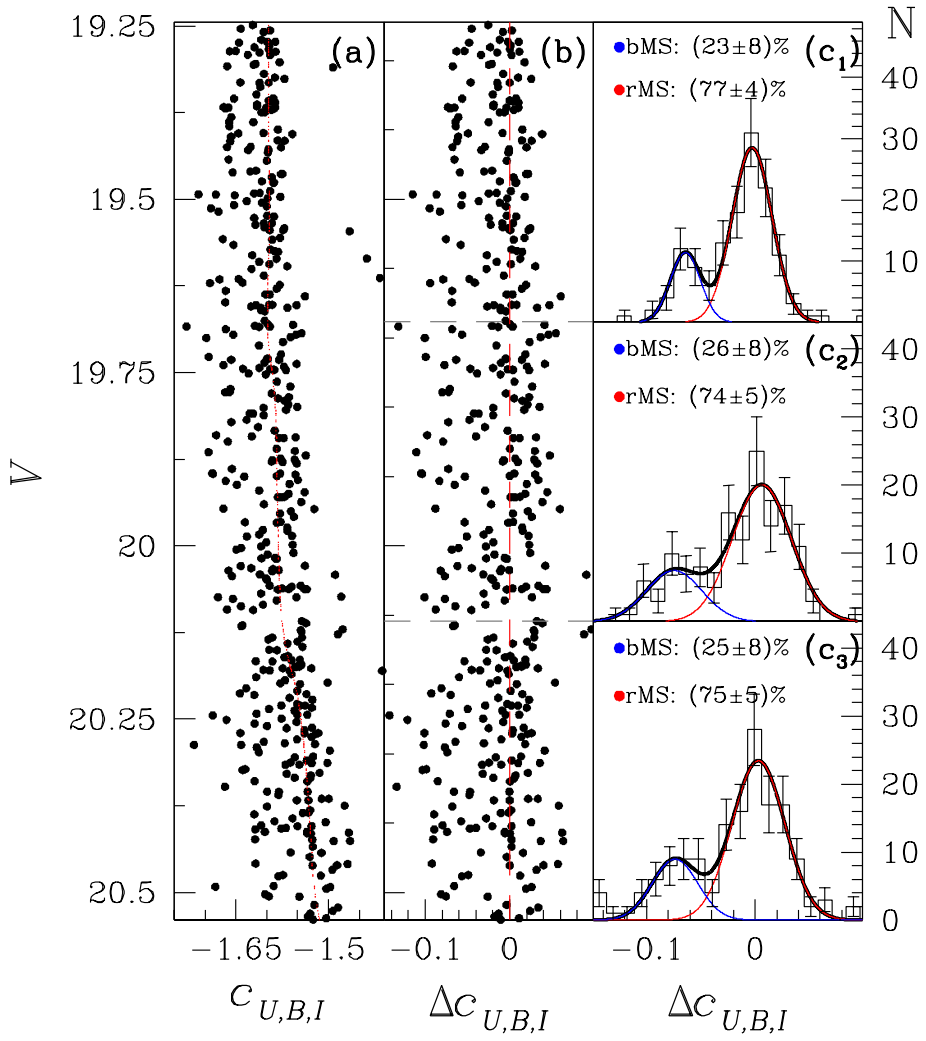


Figure 42: Procedure to estimate the fraction of rMS and bMS stars in NGC 6752 using the $V$ versus $c_{U,B,I}$ diagram (panels (a), (b), and (c)), and the $B$ versus $U-B$ CMD (panels (d), (e), and (f)). Panel (a) reproduces the same diagram as Figs. 40. The red line is the rMS fiducial line. Panel (b) show the verticalized MS. The histogram distribution of $\Delta$(color) for the stars of the panel (b) is plotted in panels (c) for three intervals of magnitude. The thick black lines, superimposed to each histogram, are the best-fitting biGaussian functions, whose components are colored red and blue. In the case of $V$ versus $c_{U,B,I}$ CMD, we found that rMS and bMS contain $77 \pm 4$ % and $23 \pm 8$ % of MS stars in panel (c1), $74 \pm 5$ % and $26 \pm 8$ % of MS stars in panel (c2) and, $75 \pm 5$ % and $25 \pm 8$ % of the MS stars, respectively.

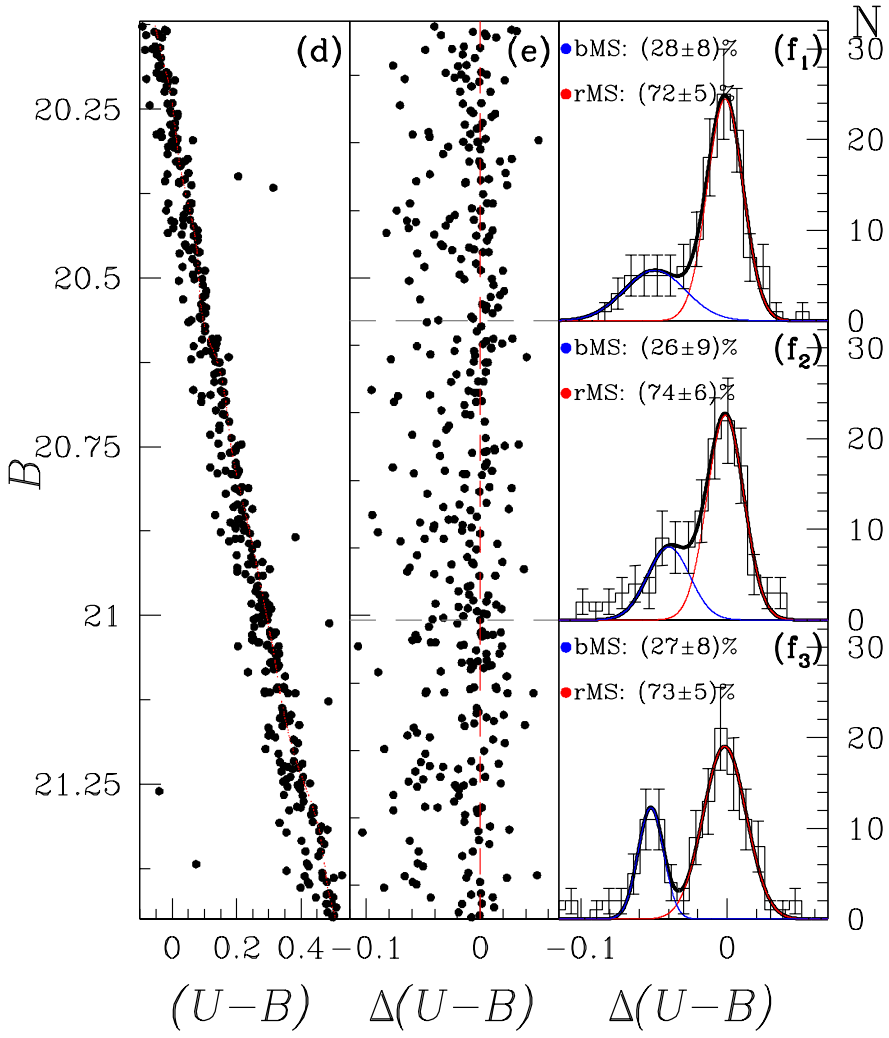


Figure 43: Procedure to estimate the fraction of rMS and bMS stars in NGC 6752 using the $B$ versus $U-B$ CMD (panels (d), (e), and (f)). Panel (d) reproduce the same diagrams as Figs. 35. The red line is the rMS fiducial line. Panel (e) show the verticalized MS. The histogram distribution of $\Delta(\text{color})$ for the stars of the panel (e) is plotted in panels (f) for three intervals of magnitude. The thick black lines, superimposed to each histogram, are the best-fitting biGaussian functions, whose components are colored red and blue. In the case of $B$ versus $(U-B)$ CMD, we found that rMS and bMS contain $72 \pm 5\,\%$ and $28 \pm 8\,\%$ of MS stars in panel (f1), $74 \pm 6\,\%$ and $26 \pm 9\,\%$ of MS stars in panel (f2), $73 \pm 5\,\%$ and $27 \pm 8\,\%$ of MS stars in panel (f3), respectively.

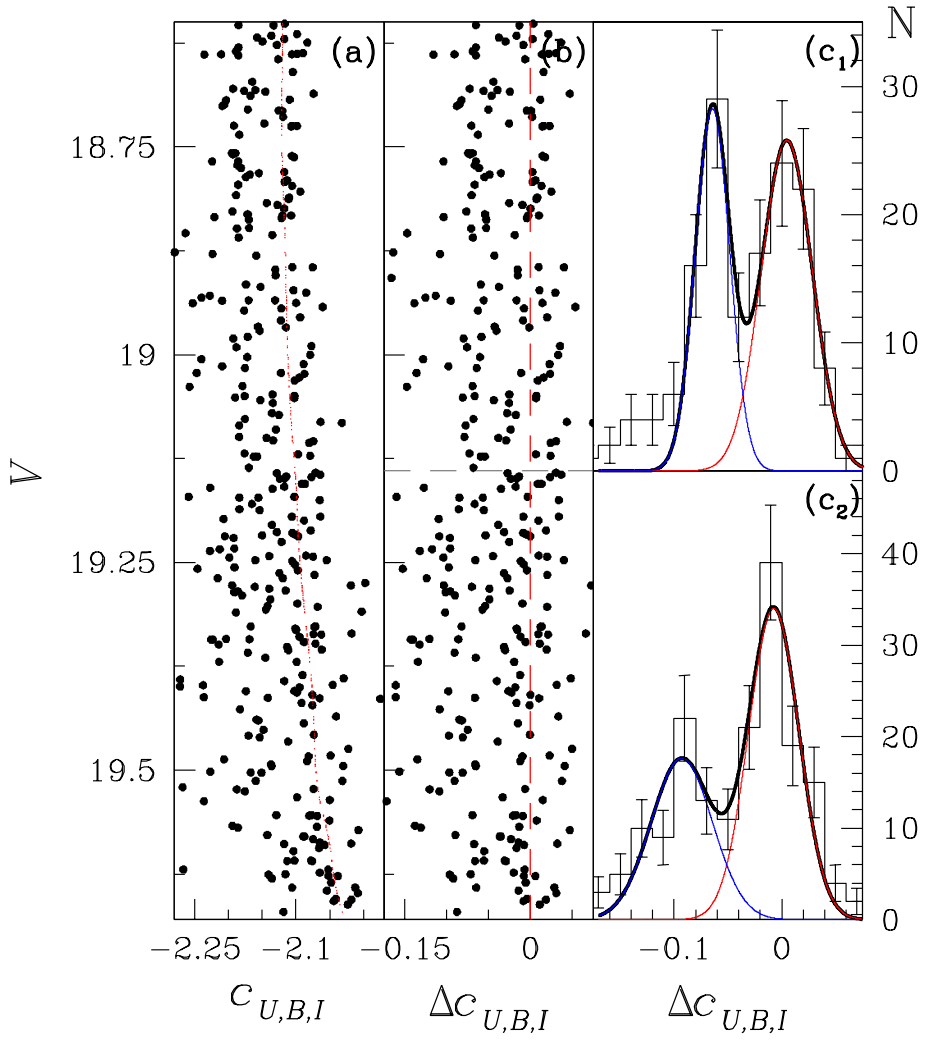


Figure 44: As in Fig. 42, in the case of NGC 6121. In the case of $V$ versus $c_{U,B,I}$ CMD, we found that rMS and bMS contain $60 \pm 7$ % and $40 \pm 8$ % of MS stars in panel (c1), $61 \pm 6$ % and $39 \pm 7$ % of MS stars in panel (c2), respectively.

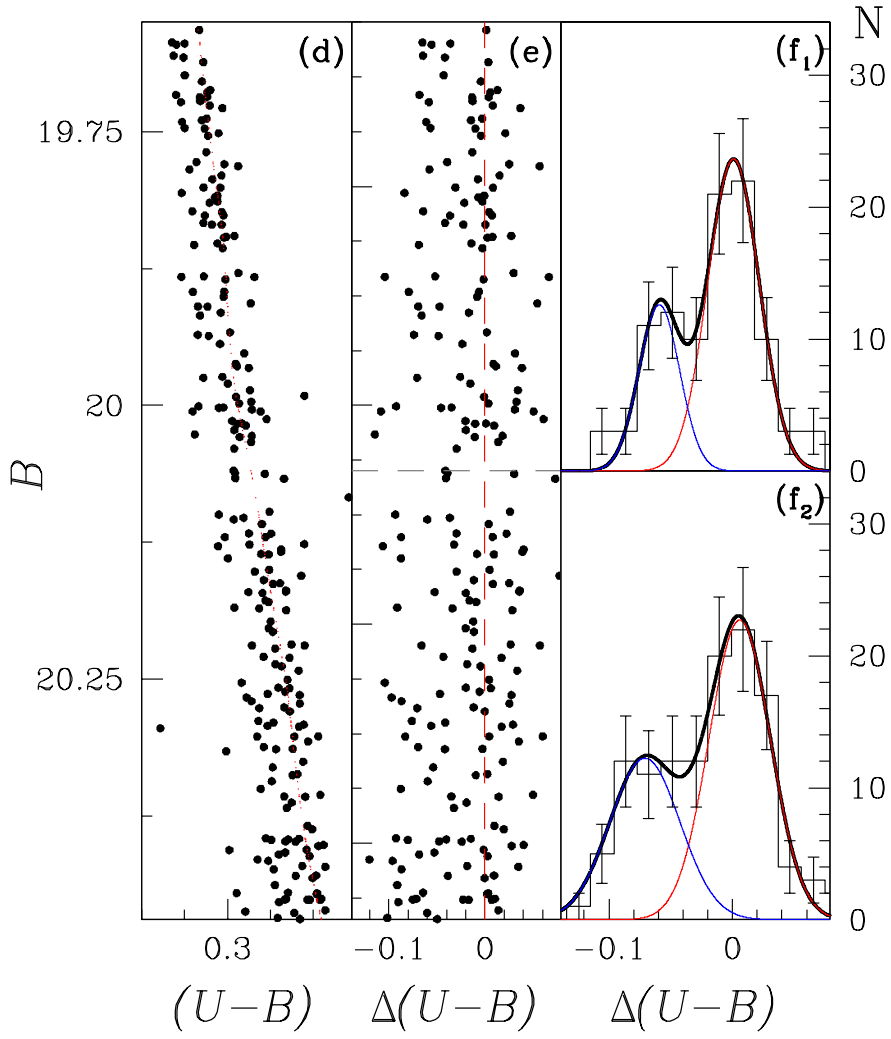


Figure 45: As in Fig. 43, in the case of NGC 6121. In the case of $B$ versus $(U-B)$ CMD, we found that rMS and bMS contain $67 \pm 7\,\%$ and $33 \pm 10\,\%$ of MS stars in panel (f1), $75 \pm 13\,\%$ and $25 \pm 14\,\%$ of MS stars in panel (f2), respectively.

as described above, but by varying the binning and starting/ending point in the histogram. We assumed $\sigma_{II}$ as the rms scatter of these $N$ determinations.

We computed the weighted mean of the bMS and rMS fractions of the three magnitude intervals, using as weight $w = 1/\sigma^2$. In the case of $V$ versus $c_{U,B,I}$, we obtained that the rMS and bMS contain $75\% \pm 3\%$ and $25\% \pm 5\%$ of MS stars, respectively. In panels (d), (e), and (f) of Fig. 43, we applied the same procedure in the $B$ versus $(U - B)$ using the stars with $20.10 < B < 21.45$. We found that the blue MS contains $27\% \pm 5\%$ of the total number of MS stars, and the red MS is made of the remaining $73\% \pm 3\%$ stars. We also calculated the weighted mean of the results of the two CMDs of NGC 6752, finding that there are the $74\% \pm 2\%$ of stars in the rMS, and the remaining $26\% \pm 4\%$ are in the bMS.

We have already demonstrated that the $\Delta(U - B)$ distribution, in the $B$ versus $U - B$ CMD of NGC 6121, shows a double peak, proving the presence of multiple populations (see panel $a_1$ of Fig. 36). We performed a detailed analysis of the MS of NGC 6121, applying the same procedure described for NGC 6752. The procedure and the results are shown in Figures 44 and 45. We find from the analysis of the $B$ versus $U - B$ CMD that the bMS contains $31\% \pm 8\%$ of MS stars, and the rMS includes the remaining $69\% \pm 7\%$. In the case of the $V$ versus $c_{U,B,I}$ diagram, we infer that rMS and bMS contain $61\% \pm 4\%$ and $39\% \pm 5\%$ of the total number of MS stars, respectively. We computed the fraction of rMS and bMS for NGC6121 using different histogram bin sizes and changing starting/ending points. We used bin sizes with values between 0.005 and 0.025 (larger than color error), starting points between -0.5 and -0.15 and ending points between 0.15 and 0.5. In all cases, the resulting fraction of stars are in agreement with the values we quote above within the errors. The results from the two CMDs imply that in the rMS and bMS there are $63\% \pm 3\%$ and $37\% \pm 4\%$ of MS stars, respectively.

## 2.5 THE RADIAL DISTRIBUTION OF STELLAR POPULATIONS IN NGC 6752 AND NGC 6121

The analysis of the radial distribution of rMS and bMS stars in NGC 6121 and NGC 6752 is an important ingredient to shed light on the formation and the evolution of multiple stellar populations in these GCs. Indeed, theoretical mod-

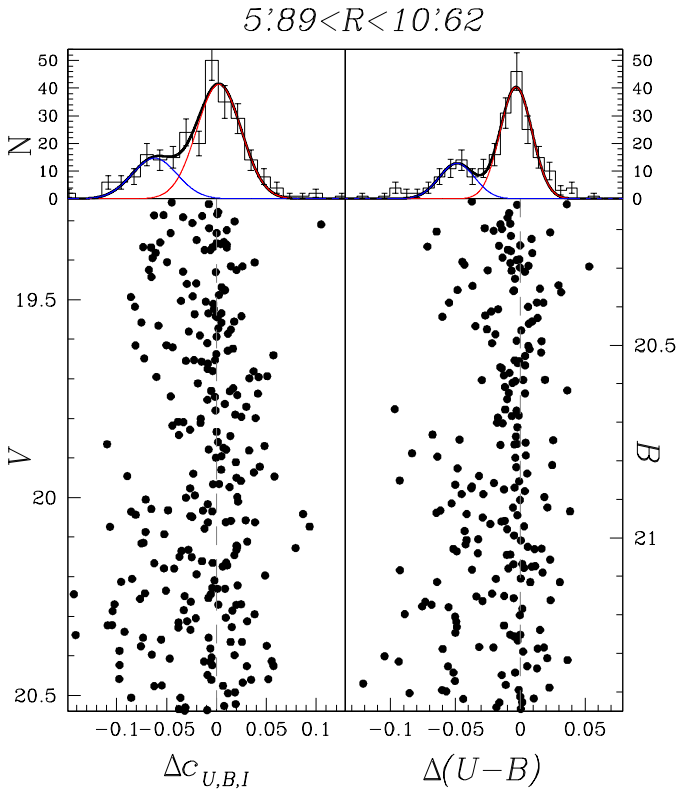


Figure 46: Color distribution analysis for the MSs stars of NGC 6752 in the inner field. We found that MSa (blue) and MSbc (red) contain $28 \pm 6$ % and $72 \pm 4$ % of MS stars, respectively, in the $V$ versus $c_{U,B,I}$ CMD, and $27 \pm 6$ % and $73 \pm 4$ % of MS stars, respectively, in the $B$ versus $(U - B)$ CMD.

els predict that, when the GC forms second-generation stars should be more centrally concentrated than first-generation stars, and many GCs could still keep memory of the primordial radial distribution of their stellar populations (e.g., D'Ercole et al. 2008, Bekki 2011, Vesperini et al. 2013).

The radial distribution of stellar populations in NGC 6752 is still controversial. Kravtsov et al. (2011) determined wide field, multiband photometry of NGC 6752 and studied the distribution of its stellar populations across the field of view. They concluded that there is a strong difference in the radial distribution between the populations of RGB stars that are bluer (bRGB) and redder (rRGB) in $(U - B)$ color, and obtained similar findings from the study of the SGB. Specifically, at a radial distance close to the half-mass radius ($r_{\rm h} = 1.91$ arcmin; Harris 1996, 2010 edition) the fraction of rRGB stars abruptly decreases. These results are in disagreement with the conclusions by Mi13 who showed that the

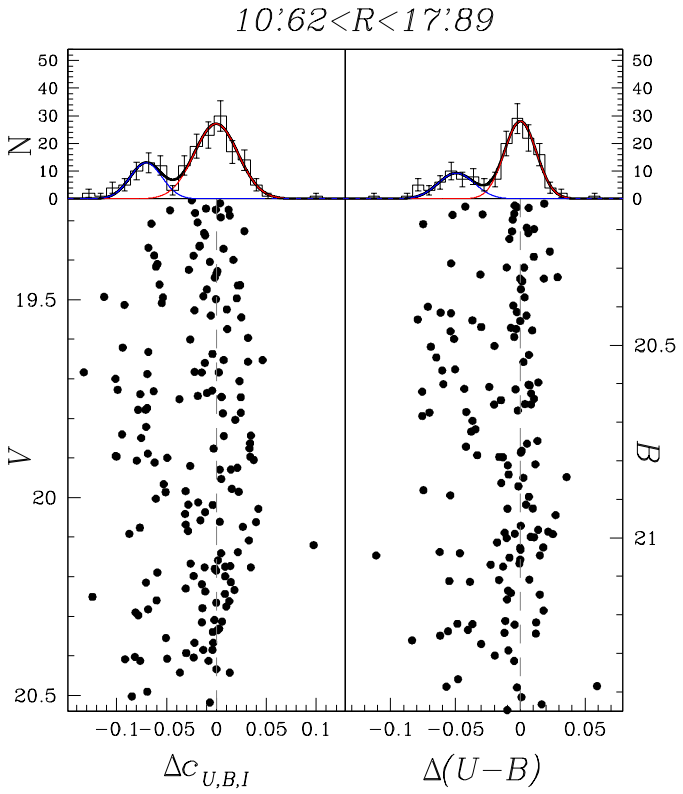


Figure 47: Color distribution analysis for the MSs stars of NGC 6752 in outer field. We found that MSa and MSbc contain $26 \pm 7$ % and $74 \pm 4$ % of MS stars, respectively, in the $V$ versus $c_{U,B,I}$ CMD, and $29 \pm 8$ % and $71 \pm 6$ % of MS stars, respectively, in the $B$ versus $(U - B)$ CMD.

three stellar populations identified in their paper share almost the same radial distribution. Kravtsov and collaborators analyzed stars with a radial distance from the center of NGC 6752 out to $\sim$ 9.5 arcmin , while the study by Mi13 is limited to the innermost $\sim$ 6 arcmin. We extend our analysis to larger radii[1].

As already mentioned in Sect. 2.4, we suggest that the bMS of NGC 6752 corresponds to the population 'a' identified by Mi13, while the most populous rMS hosts both population 'b' and population 'c' stars of Mi13. For this reason, in this section we rename the bMS in MSa and the rMS in MSbc.

To investigate the radial distribution of stellar populations within the field of view analyzed in this work, we divided the catalog of NGC 6752 stars

1 We assume that stars in the fields of NGC6752 and NGC6121 are representative of stellar populations at the studied radial distance; we are not able to investigate any dependency on the angular position using the data set presented in this work.

into two groups at different radial distance from the cluster center, each containing almost the same total number of stars.

The inner sample of stars (inner field) lies between 5.89 arcmin and 10.62 arcmin from the cluster center. The outer group of stars (outer field) is between 10.62 arcmin and 17.89 arcmin from the center. We estimated the fraction of stars in each group, following the same procedure described in Sect. 2.4.1.

The results are illustrated in Figures 46 and 47. In Fig. 46, we show the verticalized $V$ versus $\Delta c_{U,B,I}$ and the $B$ versus $\Delta(U-B)$ diagrams for stars in the inner field. In this region, the MSa contains $27\% \pm 4\%$ and the MSbc hosts the remaining $73\% \pm 3\%$ of the total number of MS stars. In the outer field ( Fig. 46), the MSa and the MSbc are made of the $27\% \pm 5\%$ and $73\% \pm 3\%$ of MS stars, respectively. We conclude that there is no evidence for a gradient within the field of view studied in this work.

To further investigate the radial distribution of stellar populations in NGC 6752 we compare our results for stars with a distance from the cluster center larger than $\sim 6$ arcmin and the fraction of stars that have been estimated by Mi13 in the internal regions using the same method.

Since the MSbc contains both populations 'b' and population 'c' stars, we have added together the fractions of population 'b' ($f_{\rm POPb}$) and population 'c' stars ($f_{\rm POPc}$) listed by Milone et al. (2013, see their Table 4) and calculated the fraction of stars in these two populations: $f_{\rm POPbc} = f_{\rm POPb} + f_{\rm POPc}$. As aforementioned in Sect. 2.4, we further compare the fractions of population 'a' stars by Mi13, with the fractions of MSa stars derived in this work. The values of $f_{\rm POPa}$ and $f_{\rm POPbc}$ are listed in Tab. 4.

Results are shown in Fig 48, where the top panels show the distribution of the fraction of population 'a' (in blue) and the fraction of population 'b'+'c' (in red) as a function of the radial distance from the cluster center, while the bottom panels show the radial trend of the ratio between the fraction of population 'a' and the fraction of population 'b'+'c'. In the left panels, we show both the above described distributions considering single radial intervals for each set of data, while in the right panels we divided each radial interval into different bins. Our findings suggest that there is no evidence for a radial gradient among population 'a' and population 'b'+'c' of NGC 6752.

| $R_{min}$ | $R_{max}$ | $R_{ave}$ | $f_{POPa}$ | $f_{POPbc}$ | Seq. |
|---|---|---|---|---|---|
| 0.00 | 1.70 | 0.95 | $0.25 \pm 0.02$ | $0.75 \pm 0.05$ | MS |
| 0.00 | 1.70 | 0.87 | $0.28 \pm 0.03$ | $0.72 \pm 0.04$ | RGB |
| 1.70 | 6.13 | 3.26 | $0.27 \pm 0.04$ | $0.73 \pm 0.06$ | RGB |
| 5.89 | 17.89 | 10.88 | $0.26 \pm 0.04$ | $0.74 \pm 0.02$ | MS |
| 0.00 | 0.53 | 0.31 | $0.24 \pm 0.02$ | $0.76 \pm 0.07$ | MS |
| 0.53 | 0.83 | 0.68 | $0.23 \pm 0.02$ | $0.75 \pm 0.05$ | MS |
| 0.83 | 1.12 | 0.97 | $0.28 \pm 0.02$ | $0.72 \pm 0.07$ | MS |
| 1.12 | 2.33 | 1.44 | $0.28 \pm 0.03$ | $0.72 \pm 0.05$ | MS |
| 1.70 | 3.11 | 2.35 | $0.26 \pm 0.05$ | $0.74 \pm 0.07$ | RGB |
| 3.11 | 6.13 | 4.15 | $0.30 \pm 0.05$ | $0.70 \pm 0.07$ | RGB |
| 5.89 | 10.62 | 8.63 | $0.27 \pm 0.04$ | $0.73 \pm 0.03$ | MS |
| 10.62 | 17.89 | 13.12 | $0.27 \pm 0.05$ | $0.73 \pm 0.03$ | MS |

Table 4: Fraction of POPa and POPbc Stars for NGC 6752

To investigate the radial distribution of stellar populations in NGC 6121, we divided the field of view we analyzed into two regions, with a radial distance from the cluster center of $5.12 < R < 9.63$ arcmin (inner field) and $9.63 < R < 17.81$ arcmin (outer field). Each region contains almost the same number of stars. We determined the fraction of rMS and bMS stars by following the same recipe described in detail for NGC 6752. The results are shown in Figures 49 and 50. We found that in the inner field the fraction of bMS is $40\% \pm 13\%$ and the fraction of rMS is $60\% \pm 13\%$. For the outer field we find that the bMS and the rMS contains $36\% \pm 6\%$ and $64\% \pm 4\%$ of the total number of the considered MS, respectively. Also for NGC 6121, we found no evidence of population gradients.

## 2.6 THE HELIUM CONTENT OF STELLAR POPULATIONS IN NGC 6121 AND NGC 6752.

The ultraviolet passband is very efficient at separating multiple sequences due to its sensitivity to difference in C, N, O abundance (Marino et al. 2008, Sbordone et al. 2011). In contrast, $B - I$ and $V - I$ colors are marginally affected by light-element variations, but are very sensitive to the helium abundance of the stellar populations (e.g., D'Antona et al. 2002, Piotto et al. 2007, Sbordone et al. 2011, King et al. 2012, Cassisi, Salaris & Pietrinferni 2013), thus providing us with an efficient tool to infer the helium content.

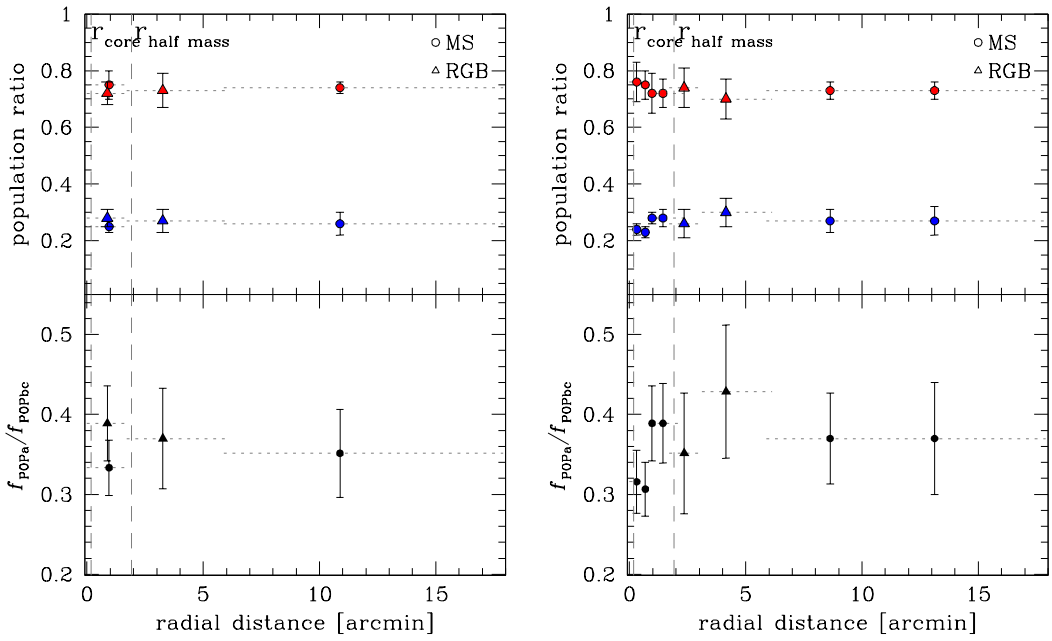


Figure 48: *Left*: Radial distribution of the fraction of population 'a' (blue) and 'b'+'c' (red) stars with respect the total number of stars. *Right*: radial trend of the ratio between $f_{\rm POPa}$ and $f_{\rm POPbc}$ stars. At left, we consider single radial interval for each set of data, while in the right panel we divide the radial interval in different bins. The distribution seems to be flat in both cases.

### 2.6.1 *NGC 6121*

The procedure to estimate the average helium difference between bMS and rMS stars for NGC 6121 is illustrated in Fig. 51 and is already used in several papers by our group (Mi13, Milone et al. 2012a,d). Since we have already extracted the stellar populations in NGC 6121 using the $B$ versus $U-B$ CMD of Fig. 45, we can now follow them in any other CMD. By combining photometry in four filters, we can construct three CMDs with $I$ versus $(X-I)$, where $X=U,B,V$. The fiducial lines of bMS and rMS in these CMDs are plotted in the upper panels of Fig. 51. The rMS fiducial line is redder than the bMS fiducial line in $U-I$ color, whereas the rMS fiducial lines are bluer in $B-I$ and $V-I$ colors.

We measured the $X-I$ color distance between the two MSs at a reference magnitude ($I_{\rm CUT}$) and repeated this procedure for $I_{\rm CUT}$=17.3, 17.5, 17.7, 17.9, and 18.1 (corresponding to the magnitude interval where the two MS sep-

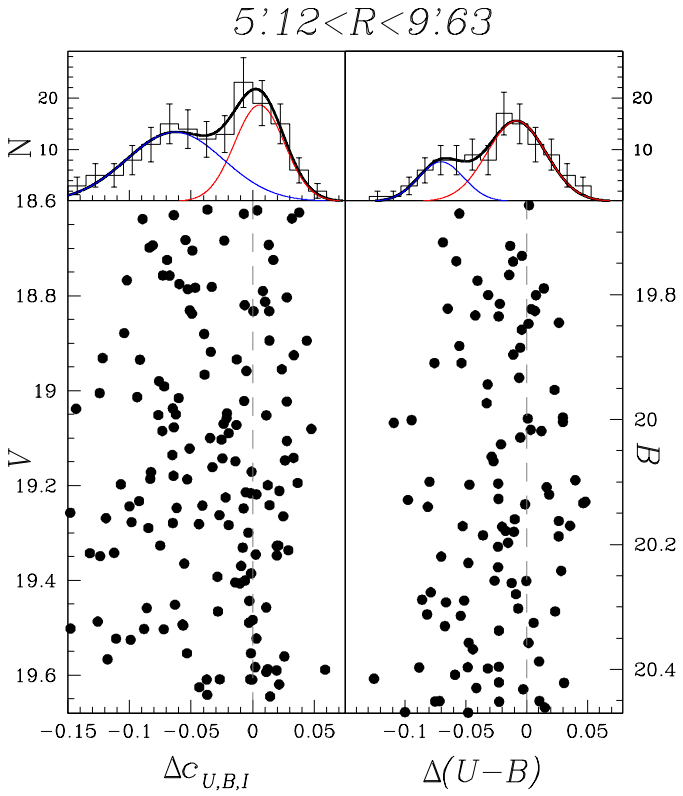


Figure 49: Color distribution analysis for the MSs stars of NGC 6121 in the inner field. We found that rMS and bMS contain $42 \pm 20$ % and $58 \pm 20$ % of MS stars, respectively, in the $V$ versus $c_{U,B,I}$ CMD, and $73 \pm 16$ % and $27 \pm 17$ % of MS stars, respectively, in the $B$ versus $(U - B)$ CMD.

arations is maximal, cf Fig. 36). The color difference $\Delta(X - I)$ is plotted in the lower panel of Fig. 51 as a function of the central wavelength of the $X$ filter (gray dots), for the case of $I_{\rm CUT}$=17.7.

We estimated effective temperatures ($T_{\rm eff}$) and gravities ($\log g$) at different $I$=$I_{\rm CUT}$ for the two MS stars and for the different helium contents using BaSTI isochrones (Pietrinferni et al. 2004, 2009).

We assumed a primordial helium abundance for the bMS, $Y = 0.248$, and used different helium content for the rMS, with $Y$ varying from 0.248 to 0.400 with steps of $\Delta Y$=0.001. To account for the appropriate chemical composition of the two stellar populations of NGC 6121, we assumed the abundances of C, N, O, Mg, Al, and Na for the bMS and the rMS as measured for first and second-generation RGB stars listed by Marino et al. (2008, see their Table 6).

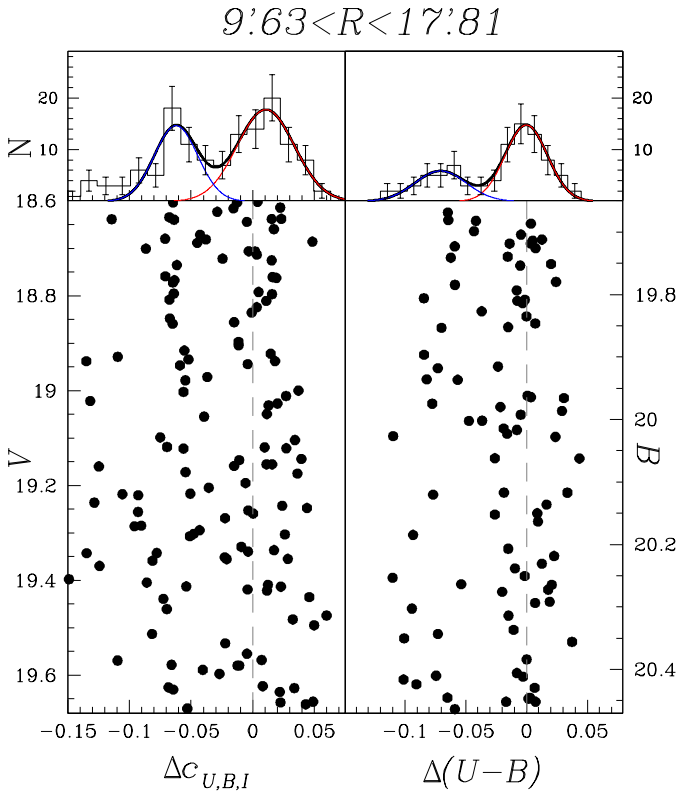


Figure 50: Color distribution analysis for the MSs stars of NGC 6121 in the outer field. We found that rMS and bMS contain $62 \pm 6$ % and $38 \pm 7$ % of MS stars, respectively, in the $V$ versus $c_{U,B,I}$ CMD, and $67 \pm 6$ % and $33 \pm 9$ % of MS stars, respectively, in the $B$ versus $(U - B)$ CMD.

We used the ATLAS12 program and the SYNTHE code (Kurucz 2005,Castelli 2005, Sbordone, Bonifacio & Castelli 2007) to generate synthetic spectra for the adopted chemical compositions, from ∼2,500 Å to ∼10,000 Å. Synthetic spectra have been integrated over the transmission curves of the $U, B, V, I$ filters, and we calculated the color difference $X - I$ for each value of helium of our grid.

The best-fitting model is determined by means of chi-square minimization. Since the $U$ magnitude is strongly affected by the abundance of light elements, we used $B - I$ and $V - I$ colors only to estimate $Y$. The helium difference corresponding to the best-fit models are listed in Table 5 for each value of $I_{\rm CUT}$.

We derived that the rMS is slightly helium enhanced with respect to the bMS (which has $Y = 0.248$), with an average helium abundance of $Y = 0.268 \pm 0.008$. This is the internal error estimated as the rms scatter of the $N = 5$ independent measurements divided by the square root of $N - 1$. Results are

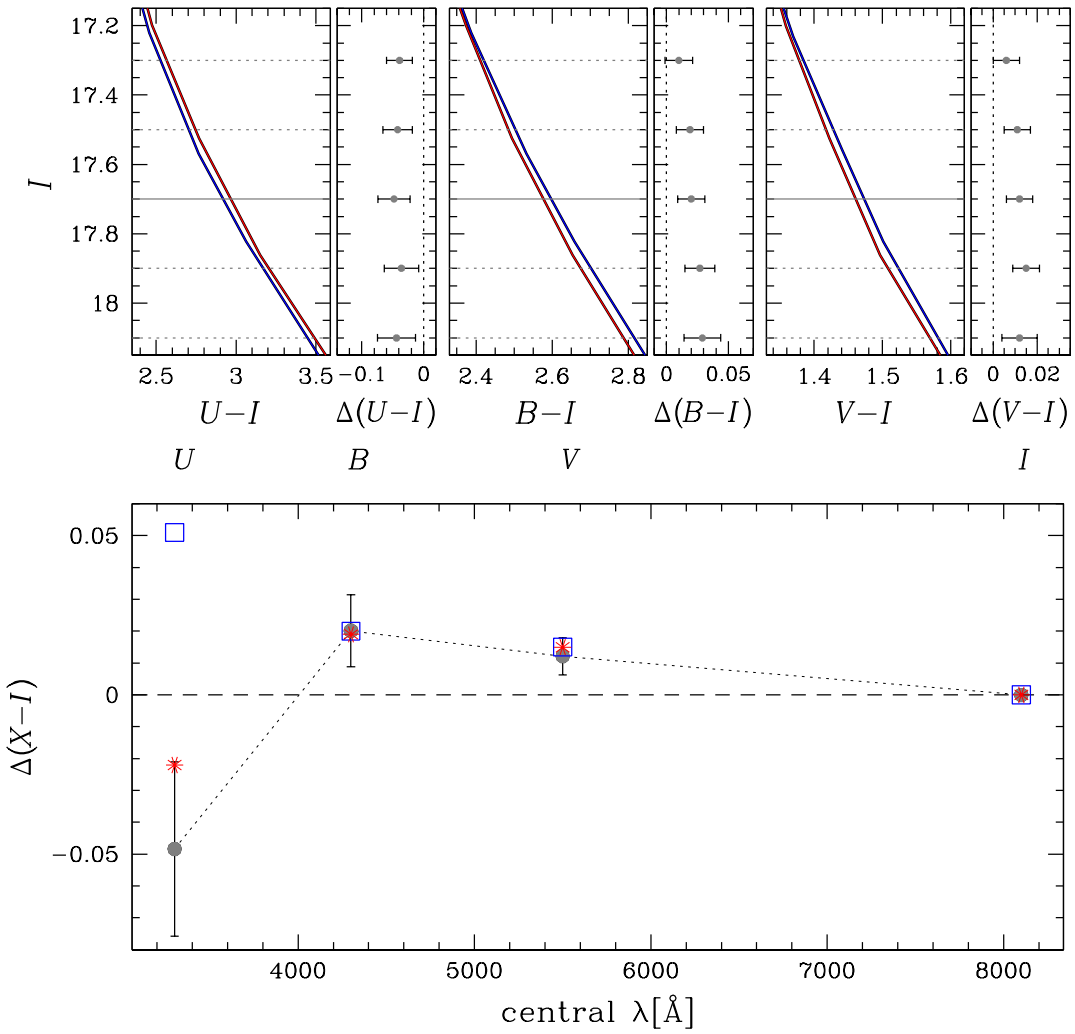


Figure 51: *Top panels:* MS fiducial in 3 $X - I$ CMDs ($X = U, B, V$ ) of NGC 6121. The horizontal lines represent the magnitudes $I_{\rm CUT}$ for which the color distance between the two MSs is calculated. For each $I_{\rm CUT}$ the error in $\Delta(X - I)$ is shown. *Bottom panel:* $X - I$ color distance between rMS and bMS at $I_{\rm CUT} = 17.7$ as a function of the central wavelength of the $X$ filter. Observations are represented with gray dots. Red asterisks are the best-fitting model, while blue squares are the results obtained calculating synthetic colors of two MS stars with the same light-element chemical composition, but different He content. The blue squares demonstrate that the abundance of light elements assumed in the model does not affect the results of the He abundance of the two MSs in the optical colors, but strongly affects the $U$ band.

shown in Fig. 51, for the case of $I_{CUT}$=17.7, where we represented the synthetic colors corresponding to the best-fitting model as red asterisks.

For completeness, we also calculated synthetic colors of two MS stars with the $I = I_{CUT}$ and the same chemical composition (same abundance of light elements). We assumed for bMS primordial helium and for rMS the helium abundance of the best-fitting model. Results are represented as blue squares in Fig. 51 and confirm that the abundance of light elements assumed in the model does not affect our conclusion on the helium abundance of the two MSs, which are based on the optical colors. Instead, the different CNO content strongly affect the *U* band.

In principle, the He content of stellar populations in GCs can also be estimated using He lines in HB star spectra (e.g., the HeI line at $\lambda = 5875.6$Àline, Villanova, Piotto & Gratton 2009; Villanova et al. 2012; Marino et al. 2014a ). However, spectroscopic measurement of He in GC stars has many limitations. First of all, He can only be measured for stars in a very limited temperature interval ($8500 < T < 11500$ K). In fact, stars with $T \leq 8500$ K are not sufficiently hot to form He lines, while stars bluer than the Grundahl jump (Grundahl et al. 1999, $T \geq 11.500$K) are affected by He sedimentation and metal levitation, which alter the original surface abundance. The HB of NGC 6121 is populated on both the red and the blue side of the RR Lyrae instability strip. Spectroscopic investigation by Marino et al. (2011c) reveals that the blue HB is made of second population Na-rich and O-poor stars, while red HB stars belong to the first population. In NGC 6121, the HB segment with $8500 < T < 11500$ K corresponds to the blue HB, and therefore it only provides partial information only. In this cluster (as in many others), it is not possible to spectroscopically measure the He content of the first population.

Villanova et al. (2012) have used the HeI line at $\lambda = 5875.6$ to estimate the helium content of six blue-HB stars in the blue HB of NGC 6121. All of them are second-population stars. They derived a mean value of $Y$=0.29$\pm$0.01 (random) $\pm$ 0.01 (systematic) and conclude that second-population stars would be enhanced in helium by $\sim$0.04-0.05 dex. This estimate of the He content has been made by assuming local thermodynamic equilibrium (LTE) approximation. However, the HeI line at $\lambda = 5875.6$ is affected by non-local thermodynamic equilibrium (NLTE) effect, which can cause an error in the $Y$ estimate as large as $\Delta Y$=0.10 (see Marino et al. 2014a for the case of NGC 2808). Appropriate

| $I_{CUT}$ | $T_{EFF,bMS}$ | $T_{EFF,rMS}$ | $\log g_{bMS}$ | $\log g_{rMS}$ | $\Delta Y$ |
|---|---|---|---|---|---|
| 17.3 | 5542 | 5571 | 4.58 | 4.57 | 0.014 |
| 17.5 | 5397 | 5444 | 4.60 | 4.60 | 0.021 |
| 17.7 | 5247 | 5297 | 4.63 | 4.63 | 0.022 |
| 17.9 | 5095 | 5149 | 4.65 | 4.65 | 0.024 |
| 18.1 | 4944 | 4989 | 4.66 | 4.66 | 0.021 |
| average | | | | | 0.020, $\sigma$ =0.008 |

Table 5: Parameters used to simulate Synthetic Spectra of rMS and bMS stars and estimation of helium difference between the two population for different $I_{CUT}$ in the case of NGC 6121

NLTE analysis is required to infer reliable He abundances from spectroscopy of HB stars in NGC 6121. In contrast, the He difference between red- and blue-MS stars in NGC 6121 comes from the colors of the fiducial lines, which have small color uncertainties.

### 2.6.2 *NGC 6752*

We followed the same procedure to estimate the average helium difference between MSa and MSbc stars. We measured the color distance between the two fiducial lines of MSa and MSbc in the $I$ versus $(X - I)$ CMDs (Fig. 52), where $X = U, B, V$, at reference magnitudes $I_{CUT} = 18.55$, 18.75, 18.95, 19.15 and 19.35. The color difference $\Delta(X - I)$ at $I_{cut} = 18.95$ is plotted in the bottom panel of Fig. 52 as a function of the central wavelength of the $X$ filter.

We used BaSTI isochrones (Pietrinferni et al. 2004, 2009) to estimate $T_{eff}$ and $\log g$ at different $I_{CUT}$.

We assumed that MSa has primordial helium abundance, $Y = 0.248$, and varied the helium content of the MSbc between 0.248 and 0.400 in steps of $\Delta Y = 0.001$. We assumed for the MSa the same C, N, O, Mg, Al, and Na abundances of the population 'a' of Mi13; for the chemical composition of the MSbc we considered the average of the abundances of the population 'b' and 'c' listed by Mi13.

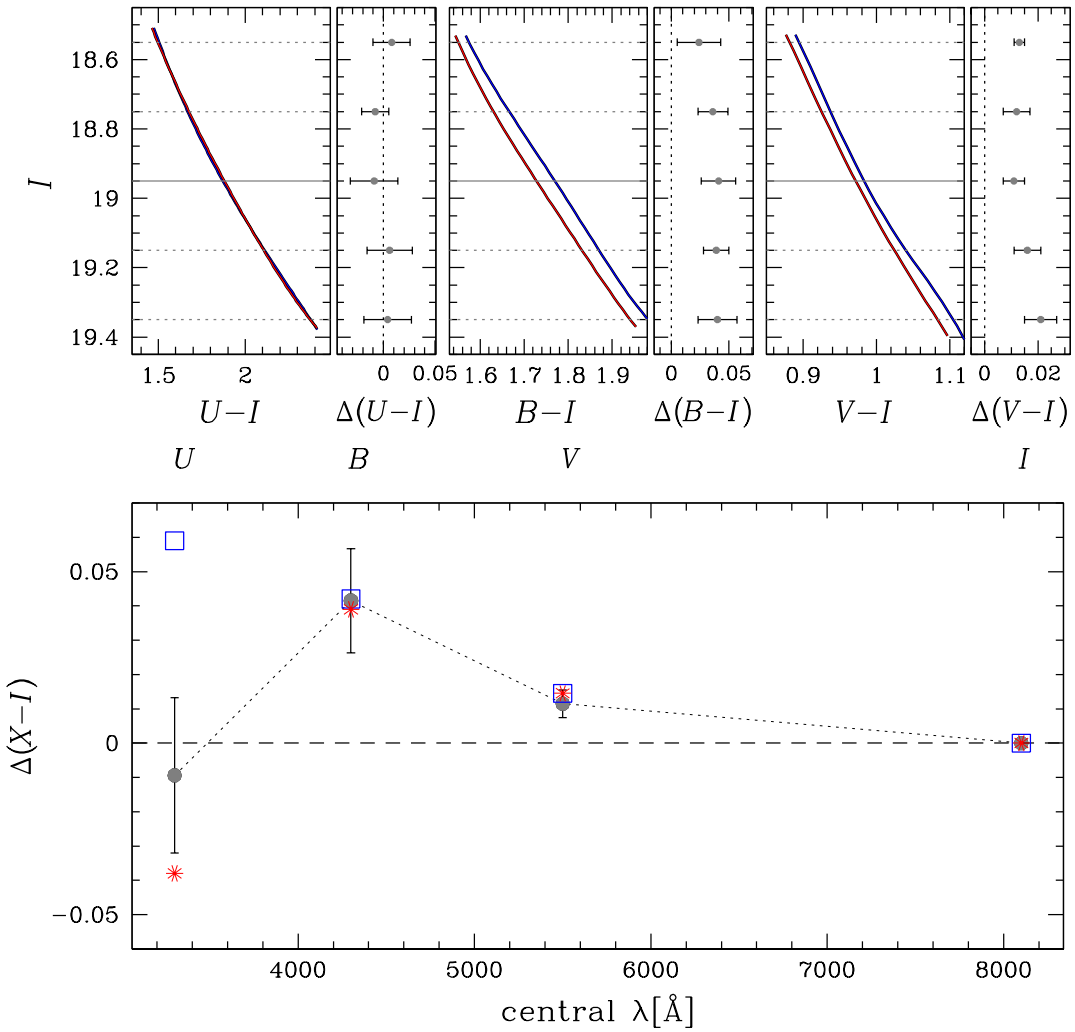


Figure 52: As in Fig. 51, in the case of NGC 6752. In the top panels, the fiducial blue is that of the MSa and the red fiducial is for MSbc.

As mentioned above, we obtained synthetic spectra for the adopted chemical compositions, integrated them over the transmission curves of the $U$, $B$, $V$, $I$ filters, and computed the helium difference using the best-fitting model.

We obtained that the MSbc is helium enhanced with respect to the MSa of $\Delta Y = 0.025 \pm 0.006$. As for NGC 6121, since the $U$ magnitude is affected by the abundance of light elements, we used $B - I$ and $V - I$ colors only to estimate $Y$. Note that the abundance of light elements assumed in the model does not affect our conclusion on the helium abundance of the two MSs, as already proven in the case of NGC 6121.

| $I_{CUT}$ | $T_{EFF,MSa}$ | $T_{EFF,MSbc}$ | $\log g_{MSa}$ | $\log g_{MSbc}$ | $\Delta Y$ |
|---|---|---|---|---|---|
| 18.55 | 5410 | 5456 | 4.65 | 4.65 | 0.021 |
| 18.75 | 5254 | 5306 | 4.67 | 4.67 | 0.023 |
| 18.95 | 5100 | 5150 | 4.69 | 4.69 | 0.023 |
| 19.15 | 4946 | 4998 | 4.70 | 4.70 | 0.025 |
| 19.35 | 4798 | 4851 | 4.72 | 4.72 | 0.026 |
| average | | | | | 0.024, $\sigma$ =0.006 |

Table 6: Parameters used to simulate Synthetic Spectra of MSa and MSbc stars and estimation of helium difference between the two population for different $I_{CUT}$ in the case of NGC 6752

### 2.6.3 *Relation between HB morphology and Helium abundance*

In their work, Milone et al. (2014b) have sought correlations between HB morphology indicators and physical and morphological GC parameters. Among these parameters there is also the maximum helium difference between stellar populations hosted by GCs.

They introduced two different parameters to describe the HB morphology: $L_1$, which is the color difference between the RGB and the coolest border the HB, and $L_2$, which is the color extension of the HB (for more details, see Fig. 1 of Milone et al. 2014b).

They divided the sample of 74 GCs in three groups: in the first group, G1, there are GCs with [Fe/H]$\geq -1.0$; the second group, G2, includes GCs with [Fe/H]$< -1.0$ and $L_1 \leq 0.4$; the third group, G3 contains GCs with $L_1 > 0.4$.

They found a tight correlation between $L_2$ and the maximum internal helium difference ($\Delta Y$, measured on the MS) for the group G2+G3 (see Fig. 8 of their paper).

We add two more points to their data set: the Helium difference between the two populations of NGC 6752 and NGC 6121, as computed in this work. In the case of NGC 6752, the added point constitutes a lower limit because the Helium difference between $Pop_a$ and $Pop_{bc}$, $\Delta Y(Pop_a\text{-}Pop_{bc})$, is the average value between $\Delta Y(Pop_a\text{-}Pop_b)$ and $\Delta Y(Pop_a\text{-}Pop_c)$.

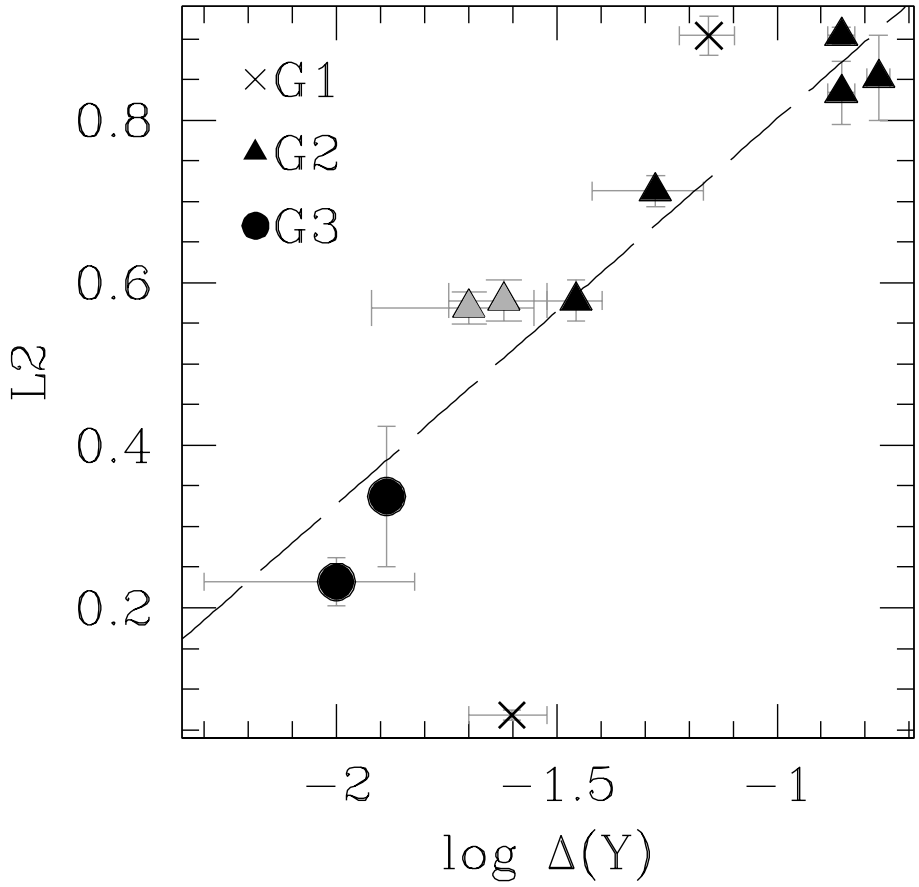


Figure 53: The HB morphological parameter $L_2$ as a function of the logarithm of the maximum helium difference among stellar populations in GCs. The black line is the best-fitting straight line for G2+G3 GCs. The data of Milone et al. (2014b) are in black, the data of this work in gray.

The result is in Fig. 53: in black there are the points of Milone et al. (2014b) and in gray the points added in this work. In analogy to the work of Milone et al. (2014b), the crosses refer to the G1 GCs, triangles to G2 group and dots to G3 clusters. Our data points confirm the tight correlation between L2 and $\Delta Y$. We found a Spearman's rank correlation coefficient $r_{G2+G3} = 0.93$ (to be compared to $r_{G2+G3} = 0.89 \pm 0.17$ found by Milone et al. 2014b), with $\sigma_{r,G2+G3} = 0.08$ (the uncertainty in $r$ is estimated by means of bootstrapping statistic, as in Milone et al. 2014b).

This result is further proof that the helium-enhanced stellar populations are likely related to the HB extension, as predicted by theory.

## 2.7 SUMMARY

The photometric analysis of ESO/FORS2 data of the external regions of the three nearby Galactic GCs NGC 6121 (M 4), NGC 6752, and NGC 6397 has confirmed that the first two GCs host multiple stellar populations. Indeed, the $B$ versus $U - B$ and $V$ versus $c_{U,B,I}$ CMDs of NGC 6752 and NGC 6121 show a split of the MS in two components. Excluding the unique case of $\omega$ Cen, this is the first time that a split of the MS is observed using ground-based facilities.

The multiple stellar populations of NGC 6397 was investigated by Milone et al. (2012a) using HST data. They found two stellar populations characterized by a modest helium variation $\Delta Y \sim 0.01$. Unfortunately, it was not possible to analyze these populations in this work, because of the size of our photometric errors is comparable to the small color separation between the MSs.

Using HST data, Mi13 have already demonstrated that NGC 6752 host three stellar populations. They computed the radial trend of the ratio between the number of stars of different populations out a radial distance from the center of 6.13 arcmin. Because of larger photometric errors, we have resolved only two MSs. Comparing them with the work of Mi13, we found that the less populous MS corresponds to their population 'a', while the most populous MS hosts both their populations 'b' and 'c'. On average, we found that the MSa contains about 26% of the total number of stars and the MSbc host about 74% of the MS stars. The most straightforward interpretation is that the MSa is formed by stars of the first generation with chemical abundances similar to that of the Galactic

halo field stars with the same metallicity; the MSbc hosts stars of second generation, formed out of material processed through first-generations stars. This population is characterized by stars enhanced in helium, with $\Delta Y = 0.025$. Our measurement of the helium enhancement is in agreement with the average $\Delta Y$ of the populations 'b' ($\Delta Y \sim 0.01$) and 'c' ($\Delta Y \sim 0.03$) obtained by Mi13. We extended the study of the radial trend of the populations of NGC 6752 to more external regions, confirming the results of Mi13, of a flat distribution. Therefore we cannot confirm the results by Kravtsov et al. (2011) and Kravtsov et al. (2014); they found that the two populations show a strong gradient at a radial distance close to the half-mass radius.

In a recent work on NGC 6121, Milone et al. (2014a) investigate the bottom of the MS of this cluster using HST near-infrared photometry. They found that the MS splits into two sequences below the MS knee. In particular they identified two MSs: a $MS_I$ that contains $\sim$ 38% of stars and $MS_{II}$ formed by the remaining 62%. They show that the split of the MS is mainly due to the effect of $H_2O$ molecules, present in the atmospheres of M-dwarfs, on their near-infrared color, and that it is possible to associate the $MS_I$ with a first generation of stars and the $MS_{II}$ to a second generation of stars. Marino et al. (2008), analyzing spectra of RGB stars, found that $\sim$ 64% of stars are Na-rich and O-poor and the remaining $\sim$ 36% have chemical abundances similar to those of Halo-field stars with the same metallicity. All these results are in agreement with what we have obtained in this work: the MS of NGC 6121 splits in the $B$ versus $(U - B)$ and $V$ versus $c_{U,B,I}$ CMDs. We found two MSs: a less populous MS that contains $\sim$ 37% of MS stars and constitutes the first generation of stars, and a more populous second generation MS that contains $\sim$ 63% of stars. Villanova et al. (2012), using spectroscopic measurements of blue HB (bHB) stars, found that the difference in helium abundance between these stars and the red HB (rHB) stars is $\Delta Y = 0.02/0.03$. A spectroscopic analysis of Marino et al. (2011c) revealed that the rHB stars have solar-scaled [Na/Fe], while bHB stars are Na enhanced. In contrast to the results of Villanova et al. (2012), a lower constraint to the level of He enhancement is set by Valcarce et al. (2014), founding a maximum $\Delta Y = 0.01$ between bHB and rHB stars. Analyzing how the two MS of NGC 6121 behave in different CMDs, we computed the helium abundance difference between them. Our result is $\Delta Y = 0.020 \pm 0.005$, in agreement with that obtained by Villanova et al. (2012). Also, in the case of NGC 6121, we did not find evidence of changes in the fraction of bMS/rMS stars in the radial range between $1.2\, r_h < R < 4.1\, r_h$.

Milone et al. (2014b) found a correlation between the HB morphological parameter $L_2$ and the maximum helium difference among stellar populations in GCs. Using the helium abundances computed in this work for NGC 6121 and NGC 6752, we confirm this correlation and the theoretical indications that helium enhanced stellar populations are responsible for the HB extension.

# 3

# HELIUM CONTENT AND RELATIVE AGE OF MULTIPLE STELLAR POPULATIONS WITHIN NGC 6352

Relative age of the different stellar populations hosted by a globular cluster is an important parameter, useful to constraint theoretical models of formation and evolution of multiple stellar populations. In this Chapter we demonstrate that is possible to put an upper limit on the relative age of the two well-separated populations of NGC 6352.

## 3.1 INTRODUCTION

The *Hubble Space Telescope* (*HST*) "UV Legacy Survey of Galactic Globular Clusters: Shedding Light on Their Populations and Formation" (GO 13297, PI Piotto) is a Treasury programme to study globular cluster (GC) stellar populations using multi-wavelength high-precision *HST* photometry and astrometry. The programme is fully described in Piotto et al. (2015, hereafter Paper I). The main purpose of this survey is to identify multiple stellar populations and study their properties, including their relative ages, chemical compositions, spatial distributions, and kinematics. Within GO 13297 we collected F275W, F336W, and F438W WFC3/UVIS images, approximately overlapping the F606W and F814W data from GO 10755 (PI Sarajedini, see Sarajedini et al. 2007).

In this work, we analyse photometry of stars in the Galactic GC NGC 6352. Our main purpose is to infer the helium content and determine the relative ages of its stellar populations. NGC 6352 is a Bulge (Galactic coordinates: $l = 341$, $b = -7.2$), metal-rich GC, located at 5.6 Kpc from the Sun [$(m - M)_V$=14.43, $E(B - V)$=0.22, Harris 1996, 2010 revision], and having luminosity $M_V = -6.47$ (Harris 1996, 2010 revision) and mass of $3.7 \times 10^4\, M_\odot$ (Marks & Kroupa 2010). From high-resolution spectroscopy of nine horizontal branch (HB) stars, Feltz-

| GO | PI | Instrument | Filter | Exposures | Epoch |
|---|---|---|---|---|---|
| 10775 | A. Sarajedini | ACS/WFC | F606W | 4×140 s, 1×7 s | 2006 Apr 10 |
| | | | F814W | 4×150 s, 1×7 s | 2006 Apr 10 |
| 12746 | A. Kong | ACS/WFC | F625W | 2×150 s | 2012 Feb 13 |
| | | | F658N | 1×650 s ,1×643 s | 2012 Feb 13 |
| 13297 | G. Piotto | WFC3/UVIS | F275W | 2×706 s, 2×800 s | 2013 Aug 13 |
| | | | | | 2014 May 27 |
| | | | F336W | 4×311 s | 2013 Aug 13 |
| | | | | | 2014 May 27 |
| | | | F438W | 1×58 s, 1×72 s | 2013 Aug 13 |
| | | | | | 2014 May 27 |

Table 7: Log of *HST* Observations for NGC 6352.

ing, Primas & Johnson (2009) confirmed the results of previous works, that this cluster has a high metallicity ([Fe/H]$\sim -0.55$) and is $\alpha-$enhanced ([$\alpha$/Fe]$\sim$0.2).

The Chapter is organized as follows. Section 2 presents the data and data analysis. Section 3 and 4 show the characteristics of the two stellar populations hosted by NGC 6352, and their properties as seen with different combinations of colours and magnitudes. In Section 5, the difference in the helium content of the two stellar populations is calculated. In Section 6, we describe the new method we developed to estimate the difference in age between the two stellar populations. In Section 7, there are the conclusions.

## 3.2 OBSERVATIONS AND DATA ANALYSIS

In order to identify the multiple stellar populations in NGC 6352 we used WFC3/UVIS images of GO 13297 and ACS/WFC data of GO 10775. The WFC3 data set consists in 2×706 s +2 × 800 s F275W, 4 × 311 s F336W, and a 58 s + 72 s F438W images. ACS data include 4 × 140 s + 7 s F606W and 4 × 150 s + 7 s F814W images, overlapped to WFC3 images. We also reduced ACS images collected in F625W and F658N bands within GO 12746 (PI Kong). Exposure times are 2×150 s in F625W and a 650 s + 643 s in F658N. Figure 54 shows the footprint of the data used and Table 7 is a detailed log of the observations.

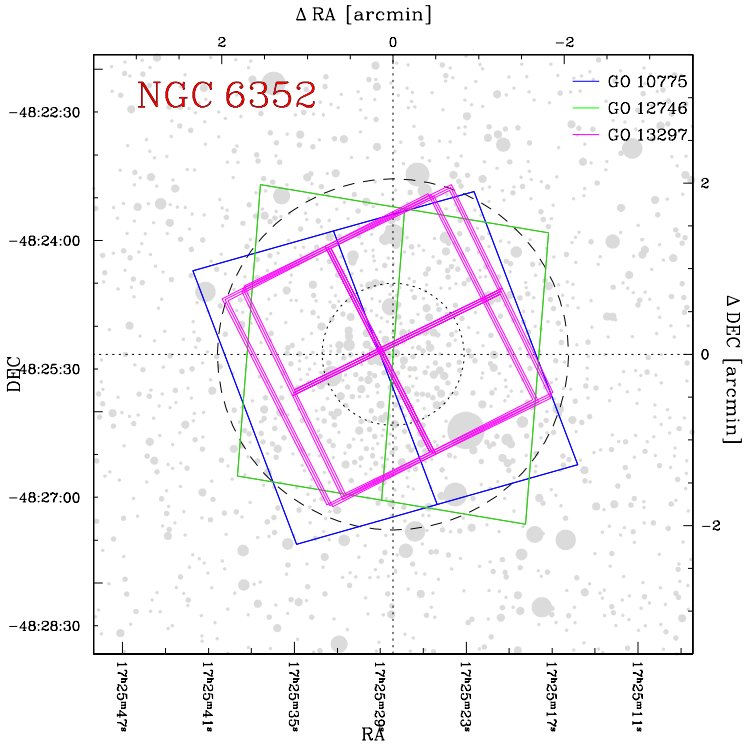


Figure 54: Footprint of the *HST* ACS/WFC (blue and green) and WFC3/UVIS (magenta) data used in this work. The dotted circle is the core radius, while the dashed circle is the half-mass radius.

A detailed description of the reduction of GO 13297 data is provided in Paper I (see their Sect. 5). We have used the photometric and astrometric catalogues published by Anderson et al. (2008) for GO 10775 data, while photometry and astrometry of archive ACS/WFC images from GO 12746 have been carried out as in Anderson et al. (2008).

## 3.3 THE COLOUR-MAGNITUDE DIAGRAMS OF NGC 6352

In Paper I (see their Fig. 2), we have shown that the colour-magnitude diagram (CMD) of NGC 6352 is not consistent with a single stellar population. The $m_{\mathrm{F814W}}$ versus $m_{\mathrm{F606W}} - m_{\mathrm{F814W}}$ CMD of the cluster members of NGC 6352 is shown in Fig. 55: in black there are the stars that, on the basis of their proper motions,

have high probability to be cluster members, in light blue the rejected stars. To derive stellar proper motions, we determined the displacement between the stellar positions in GO 10775 data set (2006.4) and in GO 13297 data set (2013.7 and 2014.5) by following the method described in detail by Piotto et al. (2012, see their Sect. 4). The maximum time baseline for the proper motion measurements is 8.1 yr.

Figure 56a shows the $m_{\rm F606W}$ versus $C_{\rm F275W,F336W,F438W}$=$(m_{\rm F275W}-m_{\rm F336W})-(m_{\rm F336W}-m_{\rm F438W})$ diagram for proper-motion-selected cluster members. Asymptotic Giant Branch (AGB), stars selected from the $m_{\rm F336W}$ versus $m_{\rm F336W}$-$m_{\rm F814W}$ CMD, are represented with starred symbols. Two distinct sequences are clearly visible and can be continuously followed from the main sequence (MS), the sub-giant branch (SGB), the red giant branch (RGB), to the HB, and the AGB. Panel (b) shows the $m_{\rm F275W}$ versus $m_{\rm F336W}$-$m_{\rm F438W}$ CMD around the region of the HB, AGB and RGB: the split of the HB is evident. Panel (c) shows the $m_{\rm F336W}$ versus $m_{\rm F275W}$-$m_{\rm F336W}$ CMD, in which the SGB splits. Panel (d) shows the double RGB in the $m_{\rm F814W}$ versus $C_{\rm F336W,F438W,F814W} = (m_{\rm F336W} - m_{\rm F438W}) - (m_{\rm F438W} - m_{\rm F814W})$ diagram. Panel (e) is the Hess diagram of the MS stars shown in panel (a) that highlights the two distinct sequences.

### 3.3.1 *Multiple stellar populations in NGC 6352*

In Fig. 57, we use the $m_{\rm F336W}$-$m_{\rm F438W}$ versus $m_{\rm F275W}$-$m_{\rm F336W}$ two-colour diagram to separate the two populations, named population-a (POPa) and population-b (POPb) hereafter. Panel (a) of Fig. 57 shows the $m_{\rm F814W}$ versus $m_{\rm F606W}$-$m_{\rm F814W}$ CMD, corrected for differential reddening and only for cluster-member stars, selected using proper motions. The green dotted lines identify the four regions in the CMD which include MS, SGB, RGB and HB stars. Again, AGB stars are plotted using starred symbols. All stars that, on the basis of their position on the CMD, are possible binaries, blue stragglers or survived field stars have been excluded from the following analysis and plotted as grey crosses.

Our recent papers demonstrated how two-colour and colour-magnitude diagrams made with appropriate combination of far-ultraviolet, ultraviolet and blue magnitudes represent a very efficient tool to identify multiple stellar populations in a GC (Milone et al. 2012a,d, 2013; Paper I). Panels (b1), (b2), (b3),

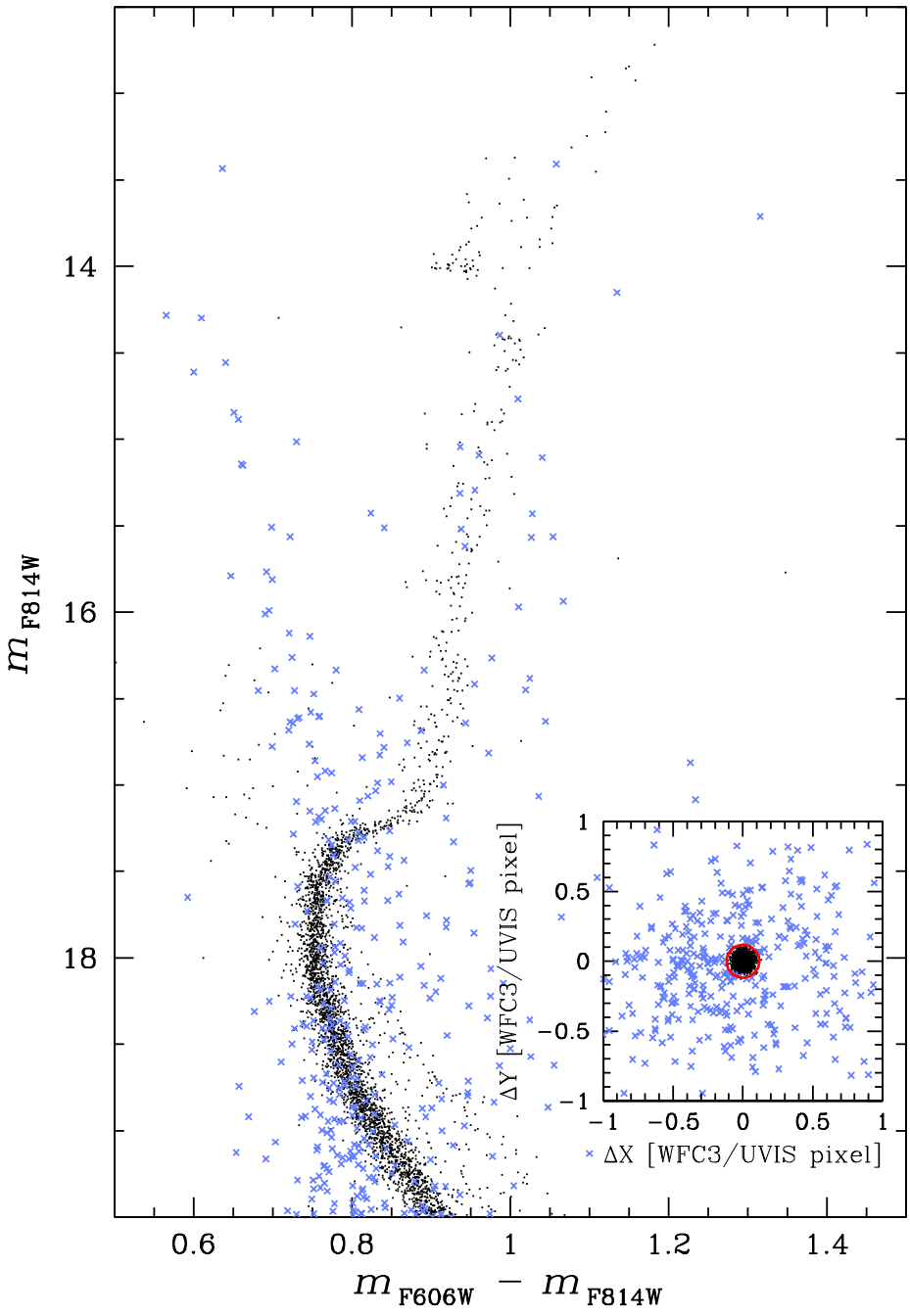


Figure 55: The $m_{F814W}$ versus $m_{F606W} - m_{F814W}$ diagram of NGC 6352. In black and in light blue are plotted cluster members and field stars, respectively. Cluster members have been selected on the basis of their proper motions. The vector-points diagram of proper motions is plotted in the inset. Black points within red circle and light blue points outside red circle indicate members and field stars, respectively.

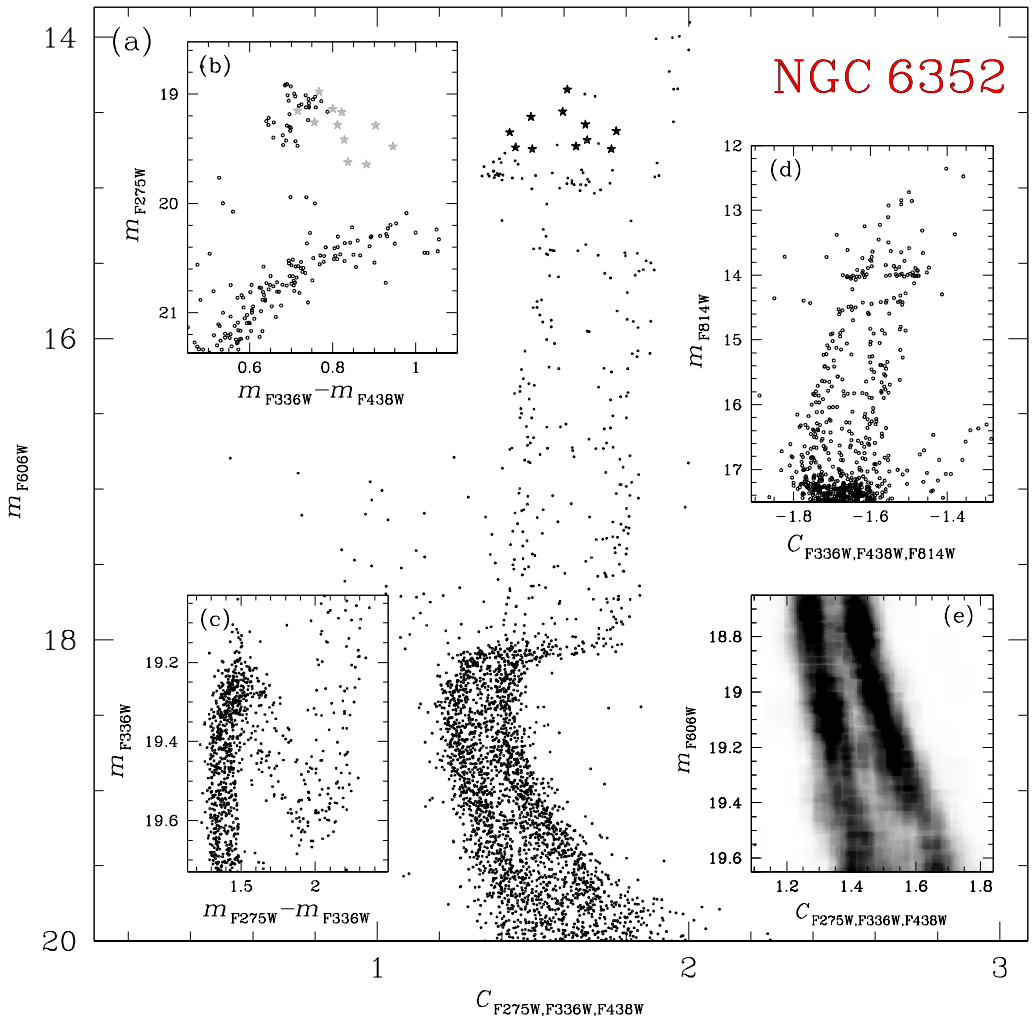


Figure 56: Overview of the main features in the CMDs of NGC 6352. Panel (a) shows the $m_{F606W}$ versus $C_{F275W,F336W,F438W}$ pseudo-CMD, in which the split of all the sequences is clear (starred points represent the AGB stars); panel (b) shows the region around the HB in the $m_{F275W}$ versus $m_{F336W} - m_{F438W}$ CMD; panel (c) highlights the SGB split in the $m_{F336W}$ versus $m_{F275W} - m_{F336W}$ diagram; panel (d) shows the RGB region in the $m_{F814W}$ versus $C_{F336W,F438W,F814W}$ pseudo-CMD. The Hess diagram of the MS stars shown in panel (a) is plotted in panel (e) and highlights the two distinct sequences.

and (b4) of Fig. 57 show the $m_{F336W}$-$m_{F438W}$ versus $m_{F275W}$-$m_{F336W}$ two-colour diagrams for the four evolutionary sequences highlighted in the left-panel CMD. Two sequences are clearly visible in each diagram. We drew by hand a straight continuous line to separate the two groups of POPa and POPb stars in the SGB, RGB + AGB, and HB, and coloured them green and magenta, respectively. The two sequences of AGBa and AGBb stars are separated by the black dashed line in panel (b2). In order to separate the two MSs we used the $m_{F814W}$ versus $C_{F275W,F336W,F438W}$ diagram plotted in panel (c1) of Fig. 57. Indeed, in this pseudo-CMD the double MS of NGC 6352 is better distinguishable than in the $m_{F336W}$-$m_{F438W}$ versus $m_{F275W}$-$m_{F336W}$ plane.

The green and the magenta fiducial lines, superimposed on the MS, are the fiducials of the MSa and the MSb, respectively, and have been obtained by using the following procedure. As a first guess, we have selected by eye a sample of MSa and MSb stars and derived for each of them a fiducial line by fitting a spline through the median values of $C_{F275W,F336W,F438W}$ obtained in successive short intervals of magnitude. We iterated this step with a sigma-clipping procedure. Then, as in Milone et al. (2015, Paper II) , we verticalized the MS in such a way that the green and magenta fiducials translate into vertical lines with abscissa $\Delta^N_{C_{F275W,F336W,F438W}}$=0 and $-1$, respectively. The histogram of the distribution in $\Delta^N_{C_{F275W,F336W,F438W}}$ plotted in panel (c2) is clearly bimodal. We considered stars with $\Delta^N_{C_{F275W,F336W,F438W}} > -0.5$ as MSa members and the remaining MS stars as MSb objects. Panel (c3) shows the $m_{F814W}$ versus $\Delta^N_{C_{F275W,F336W,F438W}}$ verticalized diagram for the MS stars. We coloured MSa and MSb stars in green and magenta, respectively. These colours will be consistently used hereafter.

### 3.3.2 *The chemical composition of the HB stars*

Typically, multiple sequences along the CMD correspond to distinct stellar populations with different content of helium and light elements (see, e.g., Marino et al. 2008; Yong & Grundahl 2008; Paper II). Feltzing, Primas & Johnson (2009) measured chemical abundances for nine HB stars of NGC 6352 from high signal-to-noise UVES@VLT spectra. They have confirmed that NGC 6352 is a metal-rich GC ([Fe/H]=$-0.55\pm0.03$), and is enhanced in $\alpha$ elements by [$\alpha$/Fe]$\sim$0.2 dex. Feltzing and collaborators also detected significant star-to-star sodium variation

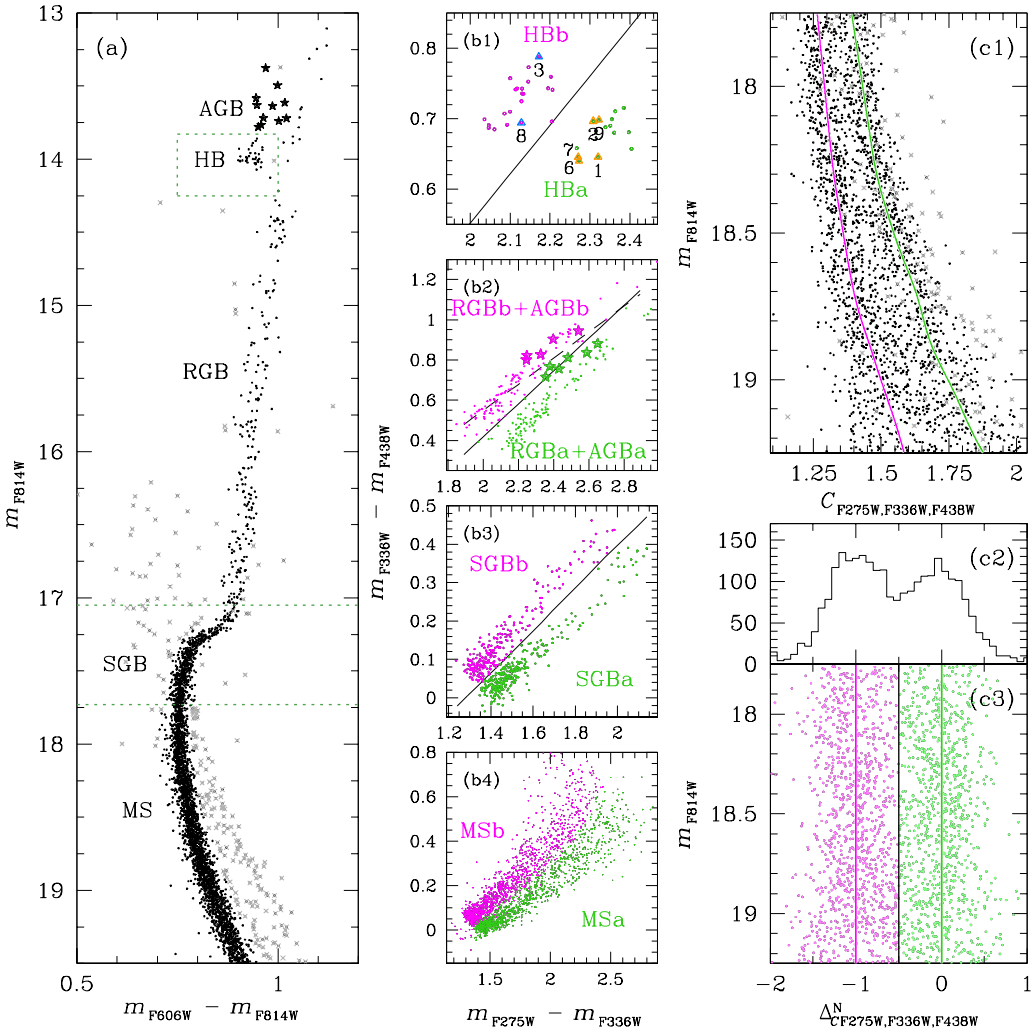


Figure 57: Procedure for the selection of POPa and POPb stars. Panel (a) shows the $m_{F814W}$ versus $m_{F606W} - m_{F814W}$ CMD of NGC 6352: grey crosses are the stars that are possible binaries and blue stragglers and that are not used in this work. Panels (b) show the $m_{F336W} - m_{F438W}$ versus $m_{F275W} - m_{F336W}$ diagrams for MS, SGB, RGB, AGB and HB stars of POPa (green) and POPb (magenta). In panel (b1) we also plot the stars in common with the spectroscopic catalogue of Feltzing, Primas & Johnson (2009). Panels (c) show the procedure used for the selection of MSa and MSb stars (see the text for details).

in close analogy with what is observed in most Milky Way GCs (e.g., Kraft et al. 1993; Gratton, Sneden & Carretta 2004).

In order to investigate the chemical content of POPa and POPb, we have exploited the spectroscopic results by Feltzing, Primas & Johnson (2009). Our photometric catalog includes seven stars studied by Feltzing, Primas & Johnson (2009). Five of them belong to the HBa and are Na-poor ([Na/H]$\leq -0.38$). The other two are Na-rich ([Na/H]$\geq -0.27$) and are HBb members. The two groups of Na-rich and Na-poor stars both have the same mean metallicity [Fe/H]$= -0.55 \pm 0.02$. In panel (b1) of Fig. 57 we plotted these HB stars as triangles with the corresponding ID number adopted by Feltzing, Primas & Johnson (2009): orange triangles are for Na-poor stars, cyan triangles show the Na-rich ones.

## 3.4 MULTI-WAVELENGTH VIEW OF MULTIPLE POPULATIONS

In the previous section we used the $m_{\rm F814W}$ versus $C_{\rm F275W,F336W,F438W}$ pseudo-CMD and the $m_{\rm F336W}$-$m_{\rm F438W}$ versus $m_{\rm F275W}$-$m_{\rm F336W}$ two-colour diagram, where multiple sequences are clearly distinguishable, in order to select the members of the two stellar populations along the MS, the SGB, the RGB, and the HB of NGC 6352. We can now combine all different bands in order to study the behaviour (e.g. colour differences) of the two populations in all possible CMDs we can construct with our data. An example is shown in Fig. 58. Note that POPa stars are redder than POPb ones in the $m_{\rm F275W}$ versus $m_{\rm F275W}$-$m_{\rm F336W}$, $m_{\rm F438W}$ versus $m_{\rm F438W}$-$m_{\rm F606W}$, and $m_{\rm F275W}$ versus $m_{\rm F275W}$-$m_{\rm F814W}$ CMDs, while they are bluer in the $m_{\rm F336W}$ versus $m_{\rm F336W}$-$m_{\rm F438W}$ CMD, as in the case of 47 Tuc (Milone et al., 2012d). The two upper panels of Fig. 59 show the $m_{\rm F814W}$ versus $m_{\rm X} - m_{\rm F814W}$ fiducial lines for the RGBs (top panels) and MSs (middle panels) of the two populations, where X=F275W, F336W, F438W, F606W, F625W, and F658N.

POPa is redder than POPb in most of the CMDs of Fig. 59, in close analogy with what is observed in most GCs (Bellini et al. 2010; Milone et al. 2012a,d, 2013). In visual and ultraviolet the $m_{\rm X} - m_{\rm F814W}$ colour separation between POPa and POPb increases with the colour baseline, and is maximum for $m_{\rm F275W} - m_{\rm F814W}$. The fiducial of the two populations are almost coincident in $m_{\rm F336W}$-$m_{\rm F814W}$, where POPa is slightly bluer than POPb.

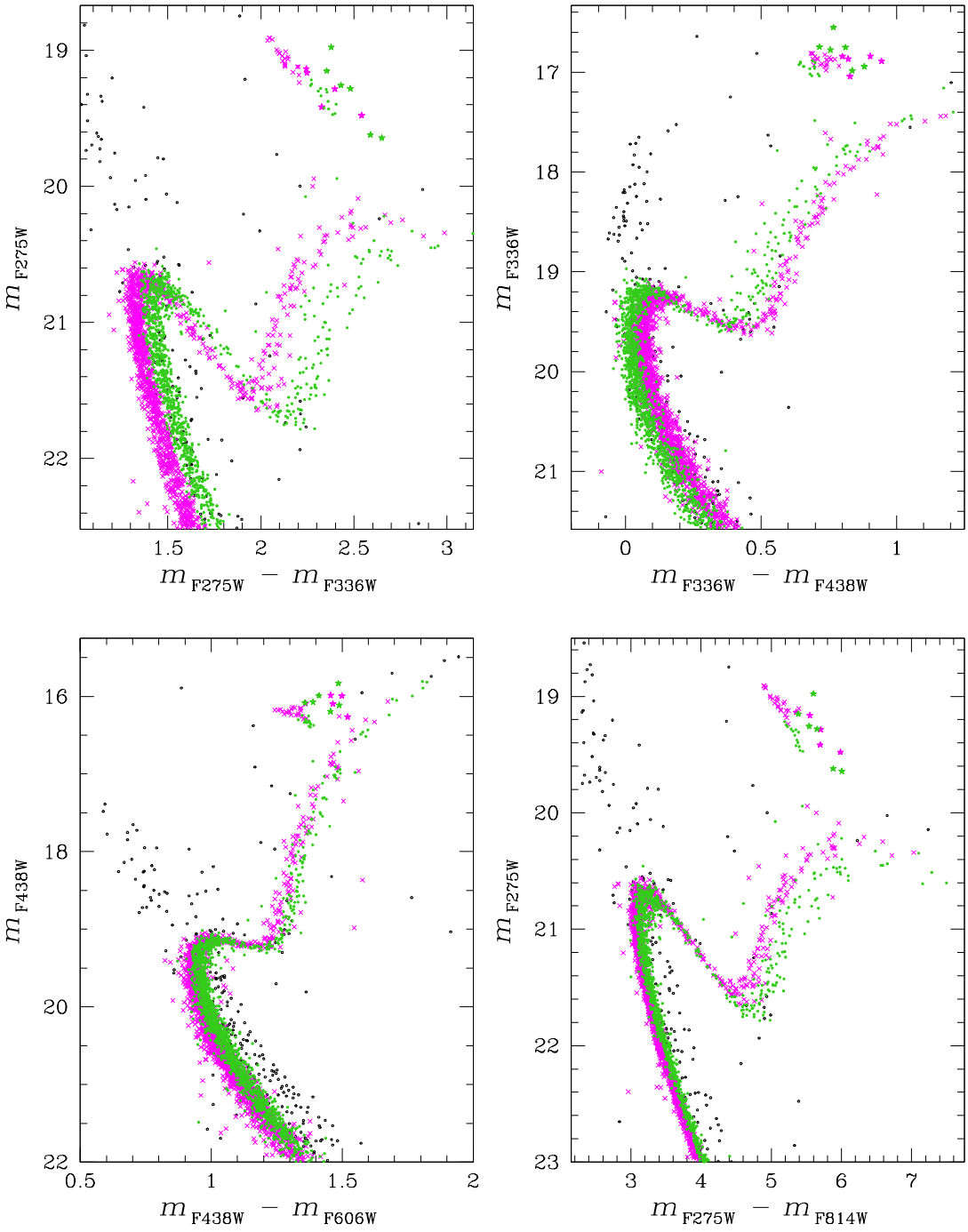


Figure 58: The $m_{F275W}$ versus $m_{F275W}$-$m_{F336W}$ (top-left panel), $m_{F336W}$ versus $m_{F336W}$-$m_{F438W}$ (top-right panel),$m_{F438W}$ versus $m_{F438W}$-$m_{F606W}$ (bottom-left panel), and $m_{F275W}$ versus $m_{F275W}$-$m_{F814W}$ (bottom-right panel) CMDs. In the first, third and fourth CMDs, POPa stars (green dots) are redder than POPb stars (magenta crosses), while in the $m_{F336W}$ versus $m_{F336W}$-$m_{F438W}$ CMD POPa stars have, on average, bluer colours than POPb stars.

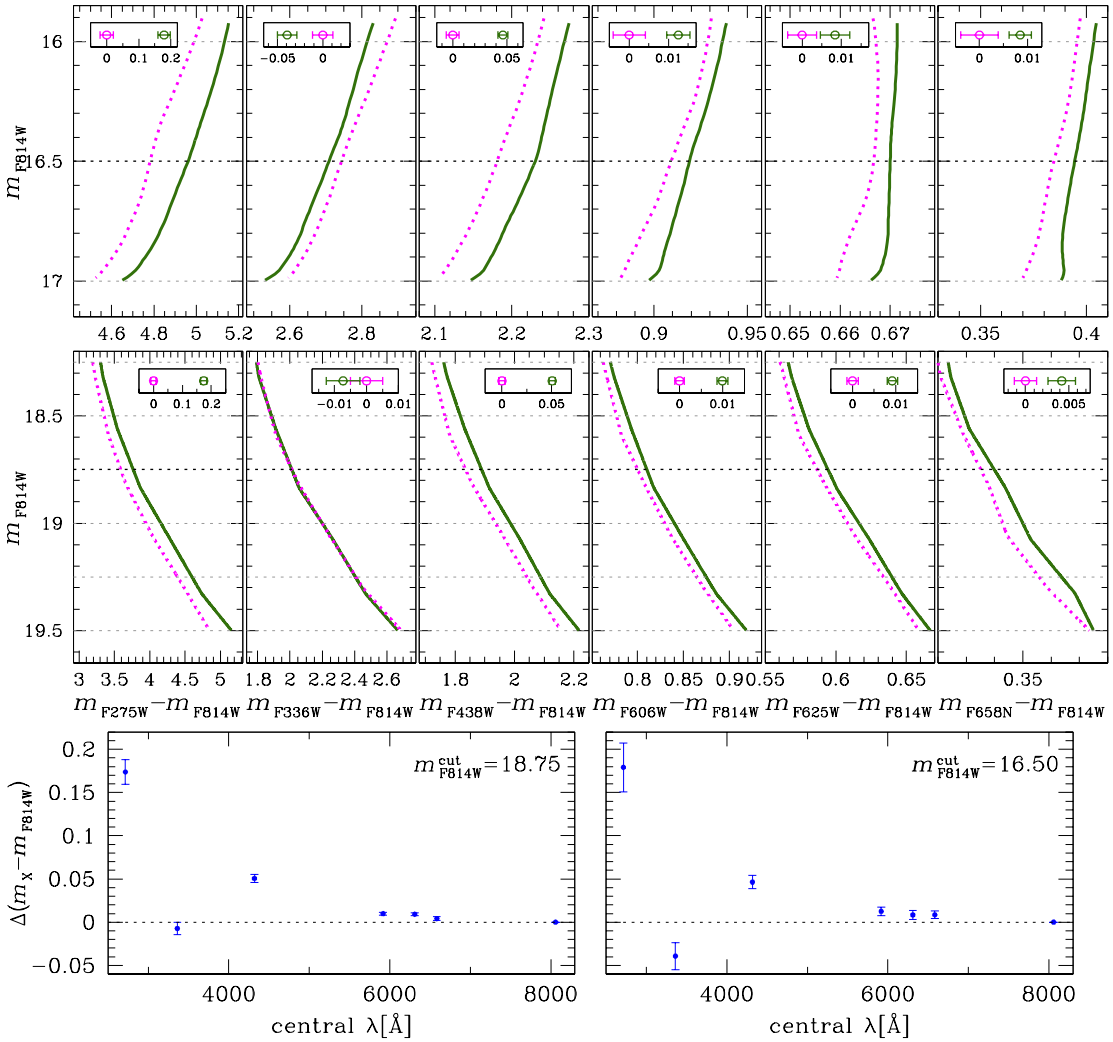


Figure 59: *Top Panels:* RGB fiducial lines for POPa (green solid lines) and POPb (magenta dotted lines) in six $m_{F814W}$ versus $m_X - m_{F814W}$ CMDs (where X=F275W, F336W, F438W, F606W, F625W, F658N); the panel insets show the colour distance between the two fiducials at $m^{CUT}_{F814W} = 16.5$. *Middle Panels:* same as top panels, but for the MS; the colour difference indicated in the inset is measured at $m^{CUT}_{F814W} = 18.75$. *Bottom panels:* $m_X - m_{F814W}$ colour distance between MSa and MSb at $m^{CUT}_{F814W} = 18.75$ (*left*) and between RGBa and RGBb at $m^{CUT}_{F814W} = 16.50$ (*right*) as a function of the central wavelength of the X filter.

The procedure used to determine each fiducial line is based on the naive estimator (Silverman, 1986). First, we defined a series of $N$ $m_{\rm F814W}$ magnitude intervals with a given width ($w$). Magnitude intervals are defined over a grid of $N$ points separated by step of fixed magnitude ($s$). We calculated the median magnitude $m_{\rm F814W,i}$ and colour $(m_{\rm X} - m_{\rm F814W})_{\rm i}$ of stars within each magnitude interval $i = 1, ..., N$. These median points have been smoothed using the smoothing technique of boxcar averaging, in which each point of a vector is replaced with the average of the $M$ adjacent points. Finally, the smoothed median points were interpolated with a cubic spline.

The choice of $w$ is the result of a compromise. On one hand, we require small magnitude intervals to account for the detailed structure of the fiducial line. On the other hand, we need a large width to include in the magnitude interval a large number of stars for a statistically significant measurement of the median colour and magnitude. We used different values of $w$ for stars with different luminosity. Specifically, we assumed $w = 0.5$ for RGB stars with $15.00 \leq m_{\rm F814W} < 17.00$, $w = 0.25$ for SGB stars with $17.00 \leq m_{\rm F814W} < 17.75$, and $w = 0.05$ for MS stars with $17.75 \leq m_{\rm F814W} < 19.00$. In all the cases we used $s = w/3$.

In order to estimate the error associated with the colours ($\sigma_{\rm fidcol}$) and magnitudes ($\sigma_{\rm fidmag}$) of each observed fiducial we used the following procedure. For each stellar population selected in Fig. 57, we assigned a subsample of artificial stars (ASs) and randomly extracted a star from it by following the recipe in Milone et al. (2009a). The AS subsample consists of all the ASs with similar magnitudes (within 0.3 $m_{\rm F814W}$ magnitudes) and radial distances (less than 100 pixels from the observed star). This method produces a catalogue of simulated stars with almost the same luminosity and radial distribution of the observed catalogue. We applied the procedure described above to estimate the fiducial line of the sample of AS stars, and calculated the difference between the fiducial of the ASs and the real stars. We repeated this step 100 times. The colour error associated with each point of the observed fiducial is calculated as the $68.27^{\rm th}$ percentile of this distribution.

## 3.5 THE HELIUM ABUNDANCE OF THE TWO STELLAR POPULATIONS

The helium abundance of a stellar population is a fundamental ingredient to understand its evolution, and to shed light on the chemical-enrichment and the star-formation history in a GC. In addition, accurate helium determination is crucial to estimate several parameters of the host star cluster, like age, mass, and mass function.

A direct spectroscopic determination of the He content in GCs is only feasible in rare cases and for a tiny subset of stars (e.g., Behr 2003; Villanova, Piotto & Gratton 2009; Dupree, Strader & Smith 2011; Pasquini et al. 2011; Marino et al. 2014a). On the other hand, the method based on multi-wavelength photometry of multiple sequences that we developed can be applied to all clusters and provides a reliable estimate of the He abundance differences among the different populations and can reach internal errors smaller then spectroscopic methods (see Milone et al. 2012d; Paper II and references therein). In the few cases where helium has been inferred from both spectroscopy of HB stars and photometry, the results from the two techniques are in fairly agreement. In the case of NGC 2808, Marino et al. (2014a) derived an helium abundance $Y = 0.34 \pm 0.01 \pm 0.05$ (internal plus systematic uncertainty) from spectroscopy of HB stars slightly bluer than the RR Lyrae instability strip. This result is consistent with the helium abundance inferred from the analysis of multiple MSs, where the middle MS (which would be associated with the stars analysed by Marino and collaborators), has $Y \sim 0.32$ (Piotto et al. 2007; Milone et al. 2012c). Similarly in the case of NGC 6397, both photometry (di Criscienzo, D'Antona & Ventura 2010; Milone et al. 2012a) and spectroscopy (Mucciarelli et al. 2014) conclude that second-population stars are slightly enhanced in $Y$ by $\Delta Y \sim 0.01$ dex. In the case of M 4, Villanova et al. (2012) found that the second population is enhanced in helium by 0.04-0.05 dex with respect to the first one. This result is in apparent disagreement with results by Nardiello et al. (2015a) who inferred an helium difference of $0.020 \pm 0.008$ dex between the two MSs of this clusters. However, it should be noted that the discrepancy could be due to Non Local Thermodynamic Equilibrium (NLTE) that affect the helium line at 5875.6 Å(see e.g. Marino et al. 2014, Sect. 4 for the case of NGC 2808).

Helium has been also inferred in RGB stars from near-infrared chromospheric transition of He I at 10 830 Åin NGC 2808 and $\omega$ Centauri. The spectra

suggest helium abundances of $Y$ <0.22 and $Y$ =0.39-0.44 ($\Delta Y \geq 0.17$) for the two analysed stars in $\omega$ Centauri (Dupree & Avrett 2013), while Na-rich and Na-poor stars of NGC 2808 analysed by Pasquini et al. (2011) differ in helium by $\Delta Y$ >0.17, with the sodium-rich star being also helium rich. Such helium variation are larger than those obtained from the analysis of multiple sequences in the CMD, that are $\sim$ 0.07 for NGC 2808 (D'Antona et al. 2005; Piotto et al. 2007; Milone et al. 2012c) and $\sim$ 0.13 for $\omega$ Centauri (King et al. 2012).

Figure 59 illustrates the procedure to infer the helium content of the stellar populations in NGC 6352. Upper panels show a collection of $m_{\rm F814W}$ versus $m_{\rm X} - m_{\rm F814W}$ fiducial lines, where X=F275W, F336W, F438W, F606W, F625W and F658N. We have used green and magenta continuous lines to plot the fiducials along the RGB (top panels) and the MS (middle panels) of the two populations. We have calculated the colour difference between the green and the magenta fiducials at the reference magnitudes indicated by the black dashed lines at $m^{\rm CUT}_{\rm F814W}$=18.75 for the MS, and $m^{\rm CUT}_{\rm F814W}$=16.50 for the RGB.

Results are shown in the lower panels of Fig. 59. We found that $\Delta(m_{\rm X} - m_{\rm F814W})$ has negative values only for X=F336W. When the other filters are used, the $m_{\rm X} - m_{\rm F814W}$ colour separation between the two RGBs and MSs is maximum for X=$m_{\rm F275W}$ and decreases towards redder wavelengths of the X filter.

In order to estimate the effective temperatures ($T_{\rm eff}$) and gravities ($\log g$) of MS and RGB stars with $m_{\rm F814W}$=$m^{\rm CUT}_{\rm F814W}$, we used the isochrones by Dotter et al. (2008) that best match the CMD.

Note that we are mainly interested in relative ages rather than in absolute ones. Indeed, as demonstrated in next section, accurate relative ages are feasible using our data set. Here, we just need reference models to calculate the colour differences of the two populations.

As discussed in Section 3.6,the best match with observations could be obtained using isochrones with [Fe/H]=$-0.67$, in fair agreement with the value inferred from high-resolution spectroscopy by Carretta & Gratton (1997), [$\alpha$/Fe]=0.4, and an age of 13.1 Gyr [adopting $(m-M)_V = 14.43$, an $E(B-V) =$ 0.22, Harris 1996, 2010 edition]. We assumed $Y = 0.256$ for POPa, and different helium abundances with $Y$ ranging from 0.256 to 0.330, in steps of 0.001, for POPb. Since there are no measurements of C, N, O abundance for NGC 6352 stars, we assumed for POPa and POPb the same C, N, O content as the two

main stellar populations of 47 Tuc. Specifically, we used for POPa [C/Fe]=-0.20, [N/Fe]=0.20, [O/Fe]=0.40, and assumed that POPb stars are depleted in carbon and oxygen by 0.20 and 0.15 dex, respectively and nitrogen enhanced by 0.7 dex with respect to POPa stars.

We used the ATLAS12 code (Kurucz 1993; Sbordone et al. 2004) to calculate atmospheric models for the MS and RGB stars with $m_{\rm F814W}$=$m^{\rm CUT}_{\rm F814W}$, while synthetic spectra have been generated with SYNTHE (Kurucz & Avrett 1981) with a resolution of $R$=600 from 2000 to 10000Å.

Synthetic spectra of POPa and POPb stars have been integrated over the transmission curves of the WFC3/UVIS and the ACS/WFC filters used in this work in order to determine synthetic colours. The colours from synthetic spectra with different $Y$ have been compared with observations in order to estimate the helium abundance of POPb.

The best fit between observed and theoretical colours at $m^{\rm CUT}_{\rm F814W}$ =18.75 can be obtained assuming POPb enhanced in helium by $\Delta$Y=0.033 dex. We have repeated this procedure for $m^{\rm CUT}_{\rm F814W}$ =18.25, 18.50, 19.00, 19.25, and 19.50 for the MS, and $m^{\rm CUT}_{\rm F814W}$ =16.00, 16.50 and 17.00 for the RGB. The results are listed in Table 8. The values of $T_{\rm eff}$, log($g$), and $\Delta$Y that provide the best fit to the observed colour differences are listed in Table 9 for each value of $m^{\rm CUT}_{\rm F814W}$. On average, we have $\Delta$Y=0.029$\pm$0.006, where the error represent the 68.27th percentile of the distribution of the sorted residuals from the mean value. To estimate $\Delta$Y we only used visual bands (F606W, F625W, F658N, and F814W), because they are not affected by light-elements variations. For this reason, the final result is not conditioned by the assumptions on the C, N, and O abundances. In the case where C, N, and O abundances were known, the final value of $\Delta Y$, obtained using all the photometric bands, would not change. As a test, we repeated the procedure described above by assuming different values of C, N, and O: we found the same result.

| $m^{\mathrm{CUT}}_{\mathrm{F814W}}$ | $\Delta m_{\mathrm{F275W,F814W}}$ | $\Delta m_{\mathrm{F336W,F814W}}$ | $\Delta m_{\mathrm{F438W,F814W}}$ | $\Delta m_{\mathrm{F606W,F814W}}$ | $\Delta m_{\mathrm{F625W,F814W}}$ | $\Delta m_{\mathrm{F658N,F814W}}$ |
|---|---|---|---|---|---|---|
| 19.50 | 0.300±0.028 | -0.016±0.017 | 0.049±0.011 | 0.012±0.003 | 0.005±0.004 | 0.001±0.004 |
| 19.25 | 0.234±0.026 | -0.009±0.012 | 0.045±0.007 | 0.011±0.002 | 0.006±0.003 | 0.005±0.003 |
| 19.00 | 0.204±0.019 | -0.003±0.009 | 0.048±0.006 | 0.012±0.002 | 0.009±0.002 | 0.005±0.003 |
| 18.75 | 0.174±0.014 | -0.007±0.007 | 0.051±0.005 | 0.010±0.002 | 0.009±0.002 | 0.004±0.002 |
| 18.50 | 0.128±0.011 | -0.011±0.006 | 0.045±0.004 | 0.007±0.002 | 0.005±0.002 | 0.001±0.002 |
| 18.25 | 0.111±0.008 | -0.008±0.004 | 0.038±0.003 | 0.008±0.001 | 0.005±0.001 | 0.001±0.002 |
| 17.00 | 0.168±0.038 | -0.056±0.030 | 0.052±0.018 | 0.016±0.008 | 0.016±0.008 | 0.022±0.009 |
| 16.50 | 0.179±0.028 | -0.039±0.016 | 0.046±0.008 | 0.013±0.005 | 0.008±0.005 | 0.009±0.005 |
| 16.00 | 0.158±0.030 | -0.033±0.020 | 0.044±0.008 | 0.011±0.005 | 0.010±0.007 | 0.010±0.006 |

Table 8: Colour difference $\Delta m_{\mathrm{X,F814W}}$ at different $m^{\mathrm{CUT}}_{\mathrm{F814W}}$.

| $m_{F814W}^{CUT}$ | $T_{EFF,POPa}$ | $T_{EFF,POPb}$ | $\log g_{POPa}$ | $\log g_{POPb}$ | $\Delta Y$ |
|---|---|---|---|---|---|
| 19.50 | 3673 | 3677 | 2.51 | 2.53 | 0.018 |
| 19.25 | 3678 | 3684 | 2.64 | 2.69 | 0.023 |
| 19.00 | 3687 | 3692 | 2.86 | 2.91 | 0.030 |
| 18.75 | 3693 | 3698 | 3.06 | 3.10 | 0.033 |
| 18.50 | 3698 | 3702 | 3.23 | 3.26 | 0.024 |
| 18.25 | 3700 | 3705 | 3.37 | 3.40 | 0.031 |
| 17.00 | 3766 | 3767 | 4.25 | 4.26 | 0.042 |
| 16.50 | 3764 | 3766 | 4.29 | 4.30 | 0.026 |
| 16.00 | 3754 | 3756 | 4.40 | 4.41 | 0.030 |
| | | | | | $0.029 \pm 0.006$ |

Table 9: Parameters used to simulate synthetic spectra of POPa and POPb stars and estimation of helium difference between the two populations for different $m_{F814W}^{CUT}$.

## 3.6 RELATIVE AGES OF THE TWO STELLAR POPULATIONS

The relative ages of the multiple stellar populations hosted by GCs is an important issue to understand how GCs formed. We can speculate that the phenomenon of multiple stellar populations in GCs is due to the presence of different generations of stars, formed in different epochs: a first stellar generation (FG) characterized by primordial helium and chemical composition similar to that of field stars with the same metallicity, and a helium-enhanced second generation (SG), characterized by stars depleted in C and O and enhanced in N and Na, born from material processed at high temperature by FG stars. If we exclude the "anomalous" GCs, such as $\omega$ Cen (Norris & Da Costa 1995), M 22 (Marino et al. 2011b), and M 2 (Yong et al. 2014, Paper II), stars of different populations in "normal" GCs show negligible differences in metallicity (Carretta et al. 2009a). Because of this, we can exclude supernova ejecta as possible polluters of the material from which SG stars formed.

Current scenarios for the formation of multiple stellar populations in GCs predict different time-scales. The AGB scenario (D'Antona et al. 2002) predicts that envelopes of intermediate mass AGB stars are the cause of pollution. In models aimed at reproducing the observed chemical patterns in "normal"

globular clusters with AGB ejecta, the second generation star formation epoch extends between about 40 and 90–100 Myr (D'Ercole et al., 2010, 2012). Another suggested mechanism is the formation of stars from material ejected by Fast-Rotating Massive Stars (FRMS) during the phase of core H-burning (Decressin et al. 2007) or massive binaries (Bastian et al. 2013; Salaris & Cassisi 2014). In these cases, the time-scale for the formation of the second generation must be of the order of a few million years or even less (Bastian et al. 2013; D'Antona et al. 2014; Salaris & Cassisi 2014).

In this work we present a method to set upper limits on the difference in age between the two populations of NGC 6352. For the first time, we estimate the relative age of two stellar populations in a normal GC, i.e. with no internal variation in [Fe/H]. Note that we are interested in measuring relative ages. The corresponding absolute ages should be only regarded as indicative (depending on the adopted distance modulus and reddening, as well as the reference model).

We consider a set of isochrones characterized by [Fe/H]= $-0.67$ and [$\alpha$/Fe]=0.4, that are the values that best fit all the stars in the $m_{\rm F814W}$ versus $m_{\rm F606W} - m_{\rm F814W}$, as explained in Sect. 3.5.

We also used the $m_{\rm F814W}$ versus $m_{\rm F606W} - m_{\rm F814W}$ CMD for computing the relative ages between the two populations, because in these filters the effect of light elements variation is not significant (Sbordone et al. 2011; Milone et al. 2012d). The MS turn-off is the classical age indicator of a simple stellar population. For this reason, we considered a region of the CMD around the MS turn-off of the two populations [panel (a) of Fig. 60]. We obtained fiducials and the associated errors in colour and magnitudes (coloured regions between dashed lines) for POPa (green) and POPb (magenta) using the same procedure described in Sect. 3.4.

In order to compute the relative age between the two populations, we treated POPa and POPb as simple stellar populations and measured their ages independently. The age of each population is estimated by comparing the observed $m_{\rm F814W}$ versus $m_{\rm F606W} - m_{\rm F814W}$ CMD with a grid of synthetic CMDs with the same [Fe/H], [$\alpha$/Fe] and $Y$, and ages that run from 12000 Myr to 15000 Myr, in step of 50 Myr.

For each isochrone a synthetic CMD was built in this way: we obtained a first guess synthetic CMD by interpolating the isochrone on the observed mag-

nitudes, in such a way that to each $m_{\mathrm{F814W}}$ magnitude in the catalogue of real stars is associated a colour $m_{\mathrm{F606W}} - m_{\mathrm{F814W}}$ on the isochrone In second step, we broadened this synthetic CMD by adding to the colour and magnitude of each synthetic star a random Gaussian error, with a dispersion equal to the error of the associated real star. The final result is a synthetic CMD, characterized by the same number of stars and a similar luminosity function to that of the observed CMD.

Panels (b) and (c) of Fig. 6o show an example of isochrones and corresponding synthetic CMDs. For each synthetic CMD, we computed the fiducial line using the same procedure as for the observed data. For each step in age, we built $N = 100$ synthetic simple stellar population CMDs, obtained the fiducial lines and computed the average of all the 1oo fiducial lines in order to obtain the final synthetic fiducial line.

We compared the observed fiducial line of each population with the synthetic ones. This method is more robust than the direct comparison between the observed CMD and the isochrones, because we compared observed and theoretical fiducial lines which were computed in the same way and are affected by the same systematic errors introduced by the method (as, e.g., the error due to the smoothing). For each step in age, we calculated the $\chi^2$ of the best fit between the synthetic and the observed fiducial, in a magnitude interval $17.00 < m_{\mathrm{F814W}} < 18.2$. We fitted the $\chi^2$ as a function of the age with a second-order polynomial, in order to find the age that minimizes the $\chi^2$. This fit was performed in two steps: first, we fitted all the points with a parabola to obtain a first-guess value of the age, $t^{\mathrm{I}}$, that minimizes the $\chi^2$ [panels ($\mathrm{d}_1$) and ($\mathrm{e}_1$) of Fig. 6o]. Then we considered only the points inside an interval between $t^{\mathrm{I}} - 500\,\mathrm{Myr}$ and $t^{\mathrm{I}} + 500\,\mathrm{Myr}$ and fitted a new second-order polynomial [panels ($\mathrm{d}_2$) and ($\mathrm{e}_2$)] to find the best value that minimizes the $\chi^2$.

We independently run this procedure for POPa and POPb. For POPa we used a set of isochrones calculated for [Fe/H]$= -0.67$, [$\alpha$/Fe]$= +0.4$ and $Y = 0.256$, while for POPb we used isochrones with the same metallicity and $\alpha$-enhancement, but enhanced in helium by $\Delta Y = 0.029$ (i.e. with $Y = 0.285$) as obtained in Section 3.5. The best fit gives an age of $(13580 \pm 80)\,\mathrm{Myr}$ for POPa and $(13570 \pm 80)\,\mathrm{Myr}$ for POPb. We want to emphasize the fact that absolute ages are not significant in this context, and that we are interested only to relative ages. For this reason, hereafter we provide only relative ages. The age error is

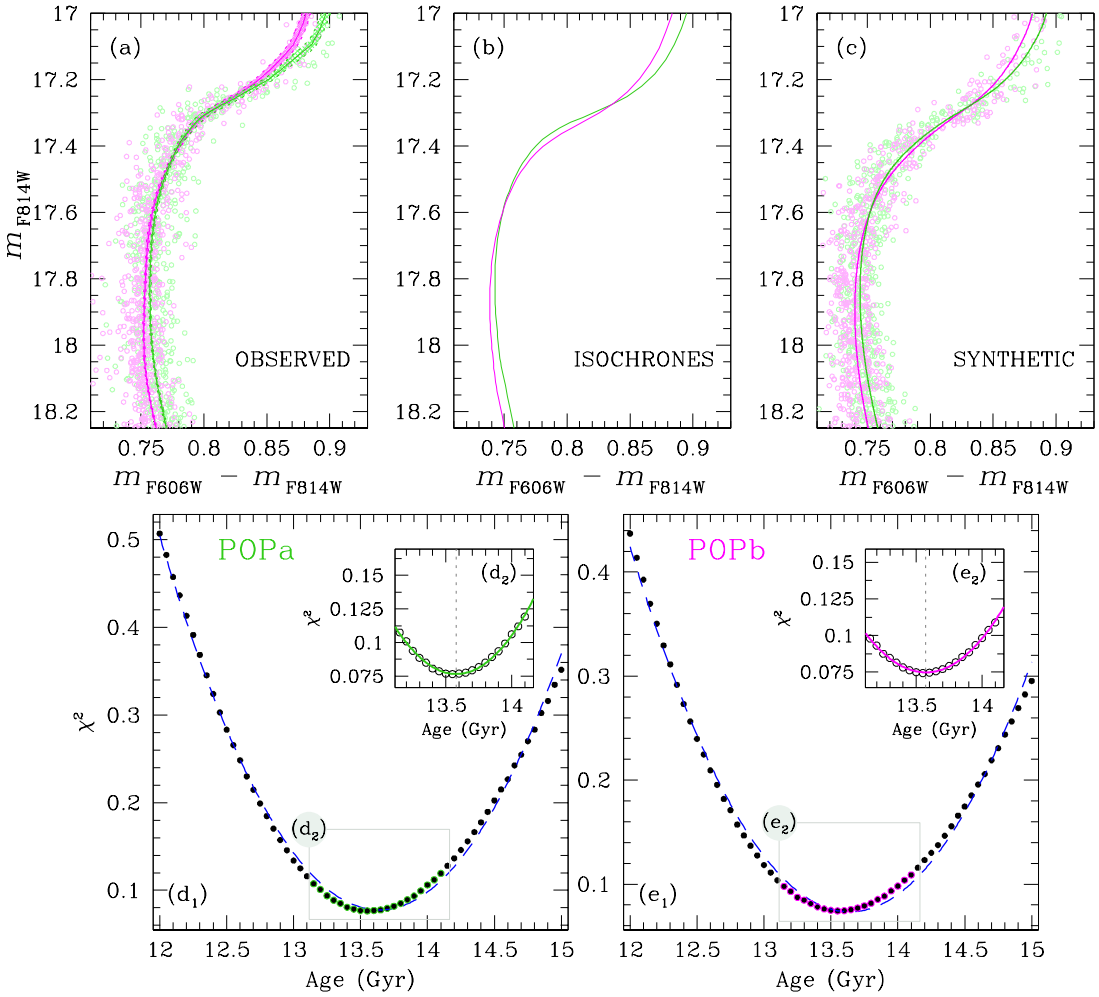


Figure 60: Procedure used to obtain the relative age of the two populations. In panel (a) the observed $m_{F814W}$ versus $m_{F606W} - m_{F814W}$ CMD is shown. In green and magenta are the fiducial lines of the POPa and POPb, respectively. Panel (b) shows the best-fitting isochrones for the two populations, while in panel (c) we plot the synthetic CMD and the fiducial lines built using the isochrones calculated for the two population. Panels (d) and (e) illustrate the procedure adopted to derive the age of POPa and POPb, respectively. In panels ($d_1$) and ($e_1$), filled circles indicate the values of $\chi^2$ for different ages while the dashed lines are the first-guess second-order polynomial fit. The insets ($d_2$) and ($e_2$) show the best-fitting second-order polynomial for POPa (green) and POPb (magenta, see text for details).

given by $\sigma = \sqrt{\sigma_{\rm PHOT}^2 + \sigma_{\rm FIT}^2}$, where $\sigma_{\rm PHOT}$ is the error due to photometric errors and $\sigma_{\rm FIT}$ is the error on the fit of the $\chi^2$ values.

The error due to photometry has been computed by performing the same analysis as described above and shifting the observed fiducial line in colour by a quantity equal to $\pm\sigma_{\rm fidcol}$ and in magnitude by a quantity equal to $\pm\sigma_{\rm fidmag}$. To estimate $\sigma_{\rm FIT}$, we used the bootstrap re-sampling of the data to generate 1000 samples randomly drawn from the original data sets; for each sample, we calculated the age that minimize the $\chi^2$ as above described. Finally we computed the mean age and its standard deviation, and adopted the latter as the uncertainty in the $\chi^2$ fit. In conclusion, the two populations have a difference in age $\Delta_{\rm AGE} = {\rm AGE}_{\rm POPa} - {\rm AGE}_{\rm POPb} = (10 \pm 110)\,{\rm Myr}$.

Figure 60 shows the whole procedure: in panel (a) we plot the CMDs of POPa and POPb (light green and magenta) and their fiducial lines. In panel (b), the best-fitting isochrones are plotted for each population; these are the isochrones for which the corresponding synthetic fiducials, shown in panel (c) with the synthetic CMDs, give the minimum $\chi^2$. Panels (d) and (e) show the procedure adopted for the fit of the $\chi^2$ for POPa and POPb respectively. In panels ($d_1$) and ($e_1$) are shown the first guess fits (blue dashed lines), while in panels ($d_2$) and ($e_2$) show the final fits (green and magenta curves for POPa and POPb respectively). The vertical dashed lines represent the value of the age that minimizes the $\chi^2$.

We performed the same analysis using CMDs with different colour bases: $m_{\rm F625W} - m_{\rm F814W}$ and $m_{\rm F658N} - m_{\rm F814W}$. These CMDs are characterized by larger photometric errors. We found $\Delta_{\rm AGE} = 80 \pm 140\,{\rm Myr}$ in the case of the $m_{\rm F814W}$ versus $m_{\rm F625W} - m_{\rm F814W}$ CMD, and $\Delta_{\rm AGE} = 220 \pm 210\,{\rm Myr}$ in the case of the $m_{\rm F814W}$ versus $m_{\rm F658N} - m_{\rm F814W}$ CMD. The results are consistent with what found using the $m_{\rm F814W}$ versus $m_{\rm F606W} - m_{\rm F814W}$, but errors due to photometric uncertainties are larger. For this reason we decided to carry out further analysis only using the $m_{\rm F814W}$ versus $m_{\rm F606W} - m_{\rm F814W}$ CMD.

We tested whether our results depend on the adopted magnitude interval for the fit. We iterated the procedure described above by changing the starting point of the magnitude interval between $m_{\rm F814W} = 17.80$ and $m_{\rm F814W} = 18.10$, and the ending point between $m_{\rm F814W} = 17.00$ and $m_{\rm F814W} = 17.30$, with steps of

0.05 mag. Within 50 Myr, we found no difference in the average age. Such age difference is consistent with zero within our measurement errors.

We tested our results using a different data set of isochrones, to prove that results are independent from adopted models. We considered BaSTI isochrones (Pietrinferni et al. 2004, 2009) and we performed the same analysis described above. We obtained a difference in age between the two populations of $(-80 \pm 110)$ Myr, in agreement with the results obtained previously.

There is some dispersion among the abundance measurements of NGC 6352 in the literature (see Feltzing, Primas & Johnson 2009 and discussion therein). Therefore, we re-iterated the same analysis using another set of isochrones with different [Fe/H] and [$\alpha$/Fe]. Following the spectroscopic results by Feltzing, Primas & Johnson (2009), we considered a set of isochrones with [Fe/H]=$-0.55$ and [$\alpha$/Fe]=+0.2 and performed the same procedure as described above. We found for the two populations a slightly different relative age ($\Delta_{\rm AGE} = 70 \pm 110$ Myr). We thus confirm that the two populations have a difference in age within $\sim$110 Myr and that the adopted values of [Fe/H] and [$\alpha$/Fe] do not change our conclusions.

In addition to the photometric error, we also considered the uncertainty in $\Delta Y$, that in the previous section we estimated to be 0.006 dex (see Table 9). In order to estimate how this error affects the measure of $\Delta_{\rm AGE}$, we iterated the same procedure previously described, using for POPa the same set of isochrones, and for POPb two additional sets of isochrones with the same [Fe/H]=$-0.67$ and [$\alpha$/Fe]=+0.4 as for POPa, but with two different helium enhancements: $\Delta Y = 0.029 + 0.006 = 0.035$ and $\Delta Y = 0.029 - 0.006 = 0.023$. We found that an error of 0.006 dex in $\Delta Y$ translates into an uncertainty in $\Delta_{\rm AGE}$ of $\sigma_{\Delta{\rm AGE}}(Y) = 40$ Myr.

The AGB and FRMS models predict that the stars of SG have the same [Fe/H] and [$\alpha$/Fe] of stars of FG, as observed in many GCs. Moreover the spectroscopic results by Feltzing, Primas & Johnson (2009) confirm that in NGC 6352 the stars of the two populations should have the same metallicity (within 0.02 dex). In any case, we also considered the cases in which POPb has different [Fe/H] or [$\alpha$/Fe] with respect to POPa, to study the impact of these variations on $\Delta_{\rm AGE}$. As first test, we considered the case in which POPb has metallicity $[{\rm Fe/H}]_{\rm POPb} = [{\rm Fe/H}]_{\rm POPa} \pm 0.02$ dex, consistent with the results by Feltzing, Primas & Johnson (2009). We performed the procedure described above us-

ing for POPa a set of isochrones with [Fe/H]=−0.67, [$\alpha$/Fe]=0.4 and primordial helium, and for POPb [Fe/H]=−0.65, [$\alpha$/Fe]=0.4, and $Y = 0.285$. We found that the relative age between the two populations is $\Delta_{\rm AGE} = 210$ Myr. In the same way, we considered for POPb a set of isochrones with the same parameters, except the metallicity that we set at [Fe/H]=−0.69. In this case we found $\Delta_{\rm AGE} = -190$ Myr Therefore, a variation on the metallicity of the second population of $\delta$[Fe/H]= $\pm$0.02 dex translates in a variation on $\Delta_{\rm AGE}$ of $\sigma_{\Delta{\rm AGE}}([{\rm Fe/H}]) = \pm 200$ Myr.

We then considered the impact of the $\alpha$-enhancement variations on the estimate of $\Delta_{\rm AGE}$. Similarly to what was done already for the variations in metallicity, we considered a set of isochrones for POPa with [Fe/H]=−0.67, [$\alpha$/Fe]=0.4 and $Y = 0.256$, and for POPb the same [Fe/H], enhanced in helium by $\Delta Y = 0.029$ and $\delta[\alpha/{\rm Fe}] = \pm 0.02$ with respect to POPa. We found that a variation of $\delta$[$\alpha$/Fe]= $\pm$0.02 dex leads to a variation on $\Delta_{\rm AGE}$ of $\sigma_{\Delta{\rm AGE}}([{\rm ff/Fe}]) = \pm 150$ Myr.

It is possible that POPa and POPb have different C+N+O abundances. Unfortunately, we are not able to directly verify the effects of C+N+O abundances variations on the estimate of $\Delta_{\rm AGE}$. Marino et al. (2012a) presented a [Fe/H]-independent relation between the C+N+O variations and the age of a population $\partial{\rm AGE}/\partial[{\rm CNO}] \sim -3.3\,{\rm Gyr\,dex^{-1}}$. If the POPb is CNO-enhanced with respect the POPa, then POPb is younger compared to the case in which both populations have the same CNO abundances, and therefore $\Delta_{\rm AGE}$ is larger. However we note that the $m_{\rm F814W}$ and $(m_{\rm F606W} - m_{\rm F814W})$ magnitude and colour on which our analysis is based are the least affected by C, N, O variations.

In Table 10, we provide a summary of all the uncertainties on $\Delta_{\rm AGE}$ introduced by the variation of the considered parameters.

## 3.7 CONCLUSIONS

In this work we have presented an analysis of the CMDs and two-colour diagrams from WFC3/UVIS F275W, F336W and F438W, and ACS/WFC F625W, F658N, F606W and F814W photometry.

We identified two stellar populations (named POPa and POPb), that, with appropriate combinations of magnitudes and colours, we could clearly dis-

| Parameter | Variation | $\sigma_{\Delta AGE}$ |
|---|---|---|
| Photometry | | $\pm$110 Myr |
| $\Delta Y$ | $\pm$0.006 | $\mp$40 Myr |
| [Fe/H] | $\pm$0.02 | $\pm$200 Myr |
| [$\alpha$/Fe] | $\pm$0.02 | $\pm$150 Myr |
| C+N+O | $\partial AGE/\partial[CNO] \sim -3.3\,Gyr\,dex^{-1}$ | |

Table 10: Summary of all the uncertainties on $\Delta_{AGE}$

tinguish on most of the evolutionary sequences of the CMD, from the MS, to the SGB, RGB, AGB, and HB.

Using a multi-colour analysis method we have already applied to half a dozen of other GCs, we estimated a $\Delta Y = 0.029 \pm 0.006$ between the two populations.

We also developed a new procedure (similar to that developed by Joo & Lee 2013) for evaluating the difference in age between the two populations hosted by NGC 6352. We considered the filter combinations that are the least affected by light-element variations. We studied the case in which POPa and POPb have the same [Fe/H], as inferred from high-resolution spectroscopy by Feltzing, Primas & Johnson (2009), but POPb has helium abundance enhanced by $\Delta Y = 0.029 \pm 0.006$. We found that the two populations have a difference in age between the POPa and POPb of $\Delta_{AGE} = 10 \pm 110$ Myr, where the error includes the photometric error and the error on the fit. The error in $\Delta Y$ leads to an error on the relative age of $\sigma_{\Delta AGE} = \pm 40$ Myr, and a total error of 120 Myr. This is the best relative ages between the two populations we can estimate assuming that the two populations have the same [Fe/H] and [$\alpha$/Fe].

In the case that POPb has a different [Fe/H] content of $\pm$0.02 dex (as suggested by high-resolution spectroscopy by Feltzing, Primas & Johnson 2009), the relative ages would change by $\pm$200 Myr. For a difference in [$\alpha$/Fe] of $\pm$0.02 dex, we found a $\Delta_{AGE}$ variation of $\pm$150 Myr. As shown by Marino et al. (2012a), if POPb is CNO-enhanced then it must be younger since the turn-off brightness is the same. Differences in metallicity between two populations hosted by a normal GC, however, are not predicted by "AGB" and "FRMS" mod-

els of formation of multiple stellar populations and are also not observed for this cluster.

In literature, there are numerous works on the relative age of multiple stellar populations hosted by anomalous GCs for which a spread in metallicity is measured. Surely, the most controversial case is represented by $\omega$ Centauri. Sollima et al. (2008) identified four coeval populations with different metallicities and helium contents, while Villanova et al. (2014) identified a large spread in age for each population and found that the most metal-rich population also is the oldest one, concluding that $\omega$ Centauri is the result of a merger of two different progenitors. Marino et al. (2012b) found that the populations of M 22, characterized by different metallicities, are almost coeval within $\sim$ 300 Myr. Lee et al. (2013) found that the GC NGC 2419 hosts two populations characterized by a large difference in [Fe/H], $Y$ and with a relative age of about 2 Gyr. Roh et al. (2011) compared models and CMDs of NGC 288 to put constraints on the second stellar population hosted by this GC. They found that, in order to properly reproduce the observed CMDs, the second generation must be moderately metal enhanced by 0.16 dex, helium-enhanced by 0.03 dex, and younger by 1.5 Gyr than the first stellar generation.

The work we present is different from previous studies on the relative ages of multiple stellar populations in GCs, in the sense that this is the first attempt to measure relative ages within a multiple population GC with no observed signature of [M/H] dispersion. Assuming no difference in [Fe/H], [$\alpha$/Fe], and C+N+O content, the two populations of NGC6352 have a 1 $\sigma$ spread in age $\sim$ 120 Myr. A combination of small differences in [Fe/H] and [$\alpha$/Fe] of 0.02 dex would rise the total uncertainty on the relative age to $\sim$280 Myr (within which the two populations are still coeval).

# 4

# CONCLUSIONS

In the last decades, many observations have demonstrated that globular clusters, the principal and oldest components of our Galaxy for which we can have a reliable age estimate, are not formed by simple stellar populations.

The presence of multiple stellar populations (MSPs) in (almost) all Galactic globular clusters (GCs) is now a certainty, suggesting that the production of multiple stellar generations is a common outcome of the formation process of all GCs.

Many spectroscopic and photometric analysis have demonstrated that the various stellar population stars have different chemical properties.

All the GCs host a first generation (FG) of stars that have a primordial chemical composition, and a second generation (SG) of stars that are C and O poor and N and Na rich and enhanced in Helium (with $\Delta Y$ that could vary from 0.01 dex to 0.15 dex). Another common feature observed in all the GCs is the anti-correlation pattern Na-O and Al-Mg. Moreover, excluding few notable exceptions (i.e., $\omega$ Cen, M22, M54, etc.), the SG stars have, within the errors, the same abundance of iron and other heavy-elements as the first generation stars, indicating that the material out of which the other generations formed, is not originated from FG supernovae, and that supernovae have played a minor role in the mechanism of formation of SG stars.

From the photometric point of view, a crucial property of MSPs is the discreteness: all the GCs show populations that are more or less separated into distinct sequences within each color-magnitude diagram (CMD) and/or appropriate two-color plots.

Photometric and spectroscopic observations suggest that the material out of which SG of stars formed was exposed to proton-capture processes at high temperatures and must have come from relatively massive stars of FG.

Many polluters have been suggested, such as intermediate-mass asymptotic giant branch stars, fast rotating massive stars, massive interacting binary stars and super-massive stars. All the scenarios linked to these polluters explain well many peculiarities of SG stars, but also have some problems in the prediction of other characteristics of SG stars.

Therefore, now we believe that the MSP phenomena is a common feature to all GCs, but we have not already realized the mechanisms of formation and evolution of MSPs in GCs.

The works presented in this Thesis, result of three years research, will give a great contribute in understanding the formation history of GCs. In the next section of this final Chapter, I summarize my main observational results and give a short description of the future research developments.

## 4.1 SUMMARY OF THESIS RESULTS AND FUTURE PROJECTS

### 4.1.1 *Radial distributions of MSPs*

The study of the radial distribution of MSPs and of the first-to-second generation global ratio ($N_{FG}/N_{SG}$) is very important to understand the formation and the dynamical evolution of the different stellar populations into a GC.

Recently, Vesperini et al. (2013) analyzed the dynamical evolution and the spatial mixing of multiple stellar populations in GCs. Theoretical models have demonstrated that SG stars were initially more concentrated in the inner regions of a GC (D'Ercole et al. 2008; Bekki 2011; Bastian et al. 2013), where previous FG stars dominated. Because of dynamical mechanisms, a great number of FG stars escape the cluster, leading to a nearly equality between FG and SG stars, and with SG stars concentrated near the center of the GC. The system evolved and FG and SG stars mix; during the mixing another loss of FG stars in the cluster's outer unmixed layers happened. Vesperini et al. (2013) found that the two body relaxation time is larger in the external regions of a GC with respect to the inner regions, and therefore the mixing occurs more efficiently in the core of a GC, resulting in a $N_{SG}/N_{FG}$ flat profile in this GC region. As the cluster evolves, and FG and SG stars mix also in the more external layers,

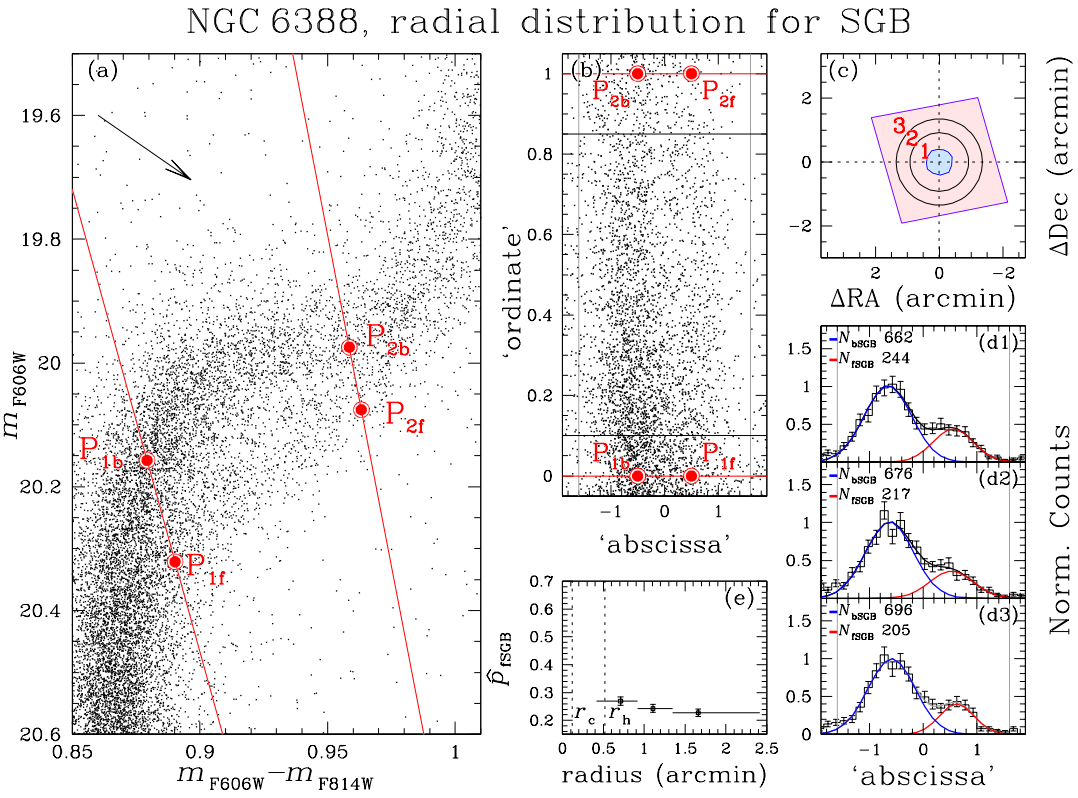


Figure 61: Procedure used to derive the radial distribution of the two stellar populations in NGC 6388 (from Bellini et al. 2013a).

the inner flat portion of $N_{SG}/N_{FG}$ profile extends toward the outer regions. A complete mixing corresponds to a flat profile extending over the entire cluster.

These theoretical predictions have been confirmed in many works, such as, for example, Nardiello et al. (2015a); Bellini et al. (2013b); Milone et al. (2012d, 2009b); Bellini et al. (2009b).

In the work by Nardiello et al. (2015a), presented in Chapter 2, we have used FORS2@VLT data to search for a split along the main sequence (MS) of the external regions of three GCs : NGC 6121 (M4), NGC 6397, and NGC 6752. Thanks to high-accuracy photometry and proper combinations of *UBVI* filters, we were able to observe MSPs in the MSs of NGC 6121 and NGC 6752.

Combining results from *Hubble Space Telescope* (*HST*) data for the inner regions of NGC 6752 (Milone et al. 2013), with the results obtained with FORS2 data for the outer regions, we found that the first-to-second generation number ratio ($N_{FG}/N_{SG}$) radial distribution is almost flat within $\sim$ 17.9 arcmin (see Fig. 48).

Also in the case of NGC 6121, we found that the radial distribution of the two stellar generations in the external regions of this GC is flat and the total ratio between $N_{FG}/N_{SG}$ is in agreement with what found by Marino et al. (2011c) and Milone et al. (2014a).

These results confirm what we expect: the two analyzed clusters are short relaxation-time systems ($\log t_{r_h} = 8.87$ for NGC 6752 and $\log t_{r_h} = 8.93$ for NGC 6121; Harris 1996, 2010 edition), and therefore it is expected that the two populations are already well-mixed at all radii and the radial distribution of $N_{FG}/N_{SG}$ is flat.

In literature there are other works on the radial profiles of $N_{FG}/N_{SG}$: Bellini et al. (2009b) found a strong radial gradient within the inner $\sim 25$ arcmin of $\omega$ Cen, a GC with a very long relaxation time ($\log t_{r_h} = 10.09$; Harris 1996, 2010 edition); by coupling *HST* and ground-based data, Milone et al. (2009b) followed the distribution of the populations in NGC 1851 from the center out the tidal radius, finding an almost flat profile for this short-relaxation time system ($\log t_{r_h} = 8.82$; Harris 1996, 2010 edition); an analysis of the radial profiles of the two populations in 47 Tuc ($\log t_{r_h} = 9.55$; Harris 1996, 2010 edition) performed by Milone et al. (2012d) has led to the conclusion that the two stellar populations are not well mixed out to $\sim$ 23 arcmin from the center of this cluster; Bellini et al. (2013a) found no significant radial gradients for the two populations in NGC 6388 ($\log t_{r_h} = 8.90$; Harris 1996, 2010 edition; see Fig. 61).

The great number of Galactic GCs with different evolutionary times, permits to explore the various possibilities in the mixing process. The observation of radial profiles of MSPs in GCs at different phases of their dynamical evolution, are a test to validate theoretical models and simulations, permits to study the mixing between the FG and SG at different evolutionary times and analyze the relationship between the global SG fraction and its local value as measured at different distances from the cluster center.

The combination of *HST* observations from the Treasury Program GO 13297 with ground-based data will permit to shed light on the dynamical evolution of MSPs in GCs. We have already demonstrated that the UV/blue *HST* filters are a good tool to disentangle the MSPs in the core of GCs, while combination of $UBVI$ ground-based data are useful to follow the MSPs in the external regions.

For these reasons, our next target is a complete analysis of first-to-second generation ratio radial profile for all the GCs in the Treasury program GO 13297, using *HST* data and, when possible, ground-based observations. Only in this way it will be possible to shed light on the mechanisms that led to the formation of GCs.

### 4.1.2 *Relative Ages of MSPs*

The relative ages of MSPs in GCs is an important topic for understanding which mechanism allowed the formation of different stellar generations.

Assuming the approximation of single stellar population and using optical data from the Treasury program GO-10775 (PI: Sarajedini), Marín-Franch et al. (2009) measured the ages of 64 GCs. But now we are able to disentangle the multiple stellar populations in these GCs, and to estimate the relative ages for the different populations.

In literature there are many works on the relative ages of MSPs hosted by 'anomalous' GCs, i.e., the clusters that show a large spread in the metallicity distribution.

Till today, the controversial case of $\omega$ Cen is subject of debate. Sollima et al. (2008) found four coeval populations with different metallicities and helium content; Villanova et al. (2014) identified a large spread in age, with the oldest population corresponding to the most metal-rich one. Marino et al. (2012a) demonstrated that the CNO abundance variations affects the determination of the relative ages of cluster sub-populations via isochrone fitting of the turn-off sub-giant branch (SGB) region, helping to reduce large age spread among the various sub-populations. Joo & Lee (2013), comparing models with observations, estimated the relative ages and metallicity of the sub-populations of $\omega$ Cen, NGC 1851, and M 22. They found that the difference in age between the most metal-rich and the most metal-poor population is $\sim 1.7$ Gyr in the case of $\omega$ Cen, and $< 1$ Gyr for the other two clusters. Also Marino et al. (2012b) found that the two populations of M 22, characterized by different metallicities, have a small difference in age, within $\sim 300$ Myr. Lee et al. (2013) found that the GC NGC 2419 hosts two populations characterized by a large spread in metallicity, different helium content and relative age of $\sim 2$ Gyr. Similar results were found

for NGC 288 by Roh et al. (2011): they found that the two populations differ in metallicity by 0.16 dex, the second generation is helium enhanced by 0.03 dex, and younger by 1.5 Gyr than the first generation.

In the work described in Chapter 3 (from Nardiello et al. 2015b), we have demonstrated that, thanks to the combination of *HST* UV/blue and optical observations, it is possible to constraint the multiple population relative ages also in 'normal' globular cluster, for which metallicity variations are not observed between stars belonging to different populations. NGC 6352 shows in UV/blue CMDs two well-splitted populations in all the evolutionary sequences (MS, SGB, RGB, and HB). This permits to obtain the fiducial lines of the two populations in a region around the MS turn-off in all the CMDs, in particular in the optical CMD $m_{\rm F814W}$ versus $m_{\rm F606W} - m_{\rm F814W}$, that is not affected by light-element variations.
Considering:

- each population of NGC 6352 as simple stellar population,
- the observed chemical abundances of the two stellar populations,
- synthetic optical CMDs, built starting from theoretical isochrones,
- all the possible sources of uncertainty, such as, the error on $\Delta Y$ or variations in [Fe/H] and [$\alpha$/Fe],

we found that the two populations of NGC 6352 are coeval within $\sim 300$ Myr.

This is an important result that permit to constrain the theoretical models of formation and evolution of MSPs in GCs. The results obtained for NGC 6352 is in agreement with the time-scales predicted by some formation scenarios. In the scenario that involves intermediate-mass asymptotic giant branch stars (D'Antona et al. 2002), the second generation star formation epoch extends between about 40 and 100 Myr (D'Ercole et al. 2010, 2012). In the fast rotating massive stars (Decressin et al. 2007) or in the massive binaries (Bastian et al. 2013) scenarios, the time scale for the formation of the second generation must be of the order of a few million years or even less.

Obviously, one only 'normal' GC is not sufficient to confirm which scenario best describes the mechanism of formation of MSPs in GCs. For this reason, our main future target is the application of the technique developed by Nardiello

et al. (2015b), to all the GCs in the Treasury program GO-13297, for which it is possible to split the various populations in the region around the MS turn-off. This will permit to confirm the proposed scenarios or will give sufficient material for the developments of new theories regarding the formation and evolution of GCs.

### 4.1.3 *The Helium content of MSPs*

The various stellar populations hosted by a GC are characterized by stars having different helium abundance. The first stellar generation have a helium abundance similar to the primordial one ($Y \simeq 0.256$); the other stellar generations are enhanced in helium by a quantity that could vary from $\Delta Y = 0.01$ to $\Delta Y = 0.15$ in the most extreme cases. The enhancement in helium is expected: helium is the main product of H-burning, and is released in the medium out of which the other stellar generations form by the stars that product also light-elements anomalies.

Direct spectroscopic determination of the He content is possible in rare cases and for a tiny subset of stars (e.g., Behr 2003; Villanova, Piotto & Gratton 2009; Dupree, Strader & Smith 2011; Pasquini et al. 2011; Marino et al. 2014a). In the case of NGC 2808, Marino et al. (2014a), using spectra of horizontal branch (HB) stars slightly bluer than the RR Lyrae instability strip, found they have an average Helium abundance of $Y = 0.34 \pm 0.01 \pm 0.05$ (internal plus systematic uncertainty). Helium could be inferred in red giant branch (RGB) stars using the near-infrared chromospheric transition of He I at 10830 Å. The spectra suggest helium abundances of $Y <$0.22 and $Y =$0.39-0.44 ($\Delta Y \geq 0.17$) for the two analyzed stars in $\omega$ Centauri (Dupree & Avrett 2013), while Na-rich and Na-poor stars of NGC 2808 analyzed by Pasquini et al. (2011) differ in helium by $\Delta Y >$0.17, with the sodium-rich star being also helium rich.

The helium content of different stellar populations can also be inferred using photometric methods. The method based on multi-wavelength photometry of multiple sequences that our group developed can be applied to all clusters and provides a reliable estimate of the He abundance differences among the different populations and can reach internal errors smaller than any spectroscopic methods (see, e.g., Milone et al. 2012d). Here some examples: the max-

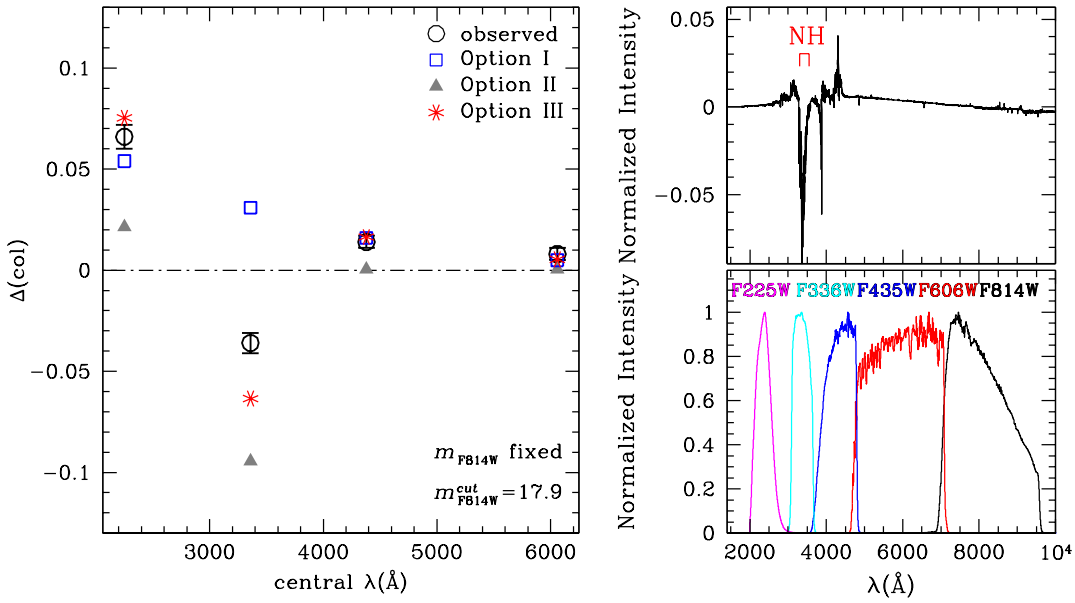


Figure 62: Procedure used to derive the helium content of the two populations in NGC 6397 (from Milone et al. 2012a).

imum helium difference for the stellar populations in 47 Tuc is $\sim$ 0.03 (Milone et al. 2012d); in NGC 288, Piotto et al. (2013) obtained $\Delta Y \simeq 0.013$; in NGC 6397 (see Fig. 62), Milone et al. (2012a) found a difference in helium of 0.01 dex; in NGC 6441 the difference in helium is $\sim$ 0.07 (Bellini et al. 2013a).

In this work we have presented the difference in helium for different stellar populations in three GCs: NGC 6752, NGC 6121, and NGC 6352. We have found that the second generation in NGC 6752 is enhanced in helium by a quantity equal to $\sim$ 0.024; similar result is in the case of NGC 6121, where the second generation is enhanced by $\sim$ 0.020 dex. We have shown that the difference in helium between the two stellar populations in NGC 6352 is $0.029 \pm 0.006$.

It is possible to note that the He-enhancement of the second generation with respect to the first generation changes from cluster to cluster. For this reason, a project that our group want to accomplish is to obtain the $\Delta Y$ for all the GCs in the Treasury program, using photometric data. This is useful to understand the chemical mechanism that have led to the formation of stellar generation enhanced in helium.

### 4.1.4 *Searching for AGB Manquè Objects*

Spectroscopic studies on asymptotic giant branch (AGB) stars have shown that some GCs host only first generation of AGB stars, and that the second generation AGB stars is missing. Indeed, many spectroscopic works that compared chemical abundances of RGB and AGB stars, have shown that CN-weak and CN-strong stars belong to the RGB, while in the AGB there are only CN-weak stars (Norris et al. 1981; Campbell et al. 2010).

This missing could be interpreted in this way: since the mass of the HB stars is correlated with their chemical composition, the He-rich, Na-rich, O-poor stars (second generation), that populate the hottest part of the HB, are less massive than first generation stars and evolve without ascending the AGB. In this way the total second-to-first generation ratio is zero.

Campbell et al. (2013) studied in detail the famous case of NGC 6752. They analyzed the spectra of RGB stars, finding a spread in [Na/Fe] of $\sim 1$ dex, while, analyzing AGB spectra, they found that all the AGB stars have an average [Na/Fe] value of $-0.07 \pm 0.10$ dex. Therefore they obtained for RGB stars a first-to-second generation ratio of about 30:70, while they found that all the AGB stars belong to the first stellar generation, obtaining a first-to-second generation ratio equals to 100:0. This means that the second generation stars must fail to enter the AGB phase. Recent studies on a sample of HB stars of NGC 6752 showed that the redder end of the blue HB contains only Na-poor stars (Villanova, Piotto & Gratton 2009), indicating that are the stars of the bluer part of the HB that fail ascending the AGB phase. Campbell et al. (2013) find that the 'ascension cut-off' corresponds to the Grundhal jump, a discontinuity in the HB morphology which is seen in all the GCs whose HB extends beyond an effective temperature of $\sim 11500$ K.

Campbell et al. (2013) used stellar models to seek an explanation of why the second generation stars fail to ascend the AGB phase after the HB phase. The models are shown in Fig. 63: in red the model representative the first stellar generation, that populate the HB before the Grundhal jump. As expected, these stars ascend the AGB. In black the stellar model track representative the He-rich second generation stars, that populate the HB after the Grundhal jump. It is possible to note that, in this case, the stars also continue to the AGB, in contrast

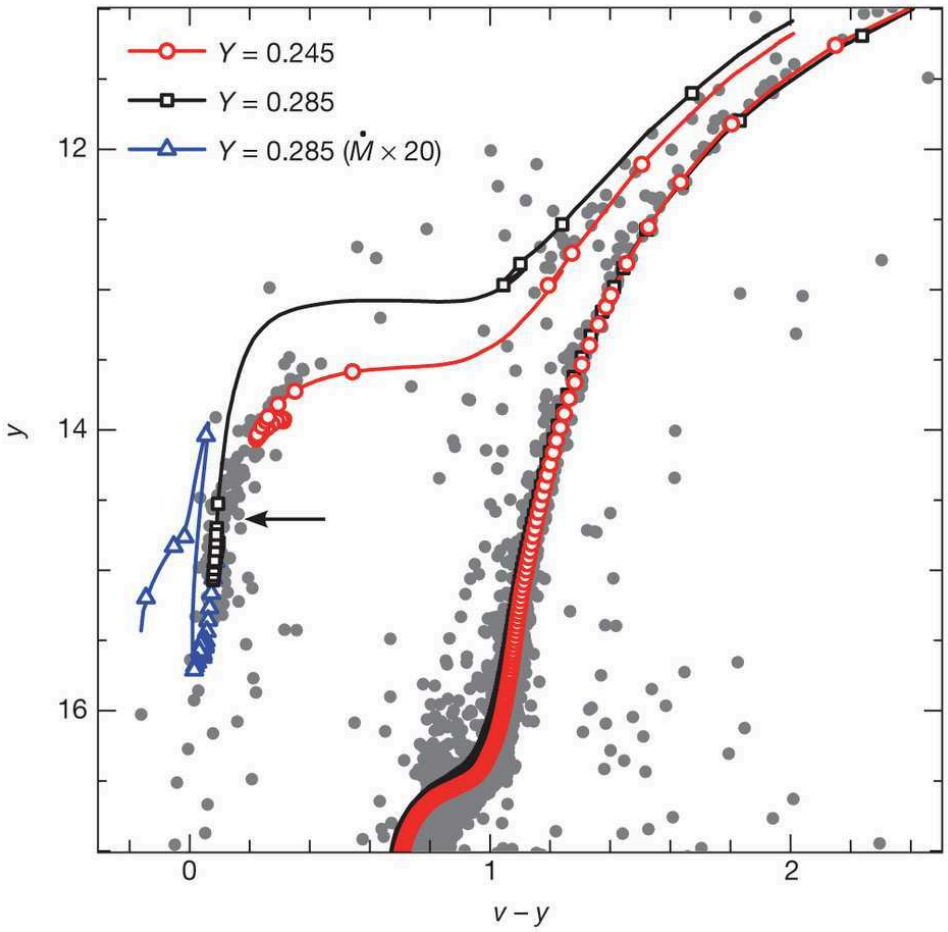


Figure 63: Theoretical stellar model tracks overlain on the Strömgren CMD of NGC 6752. The solid red line is a model with an initial mass of 0.8 $M_{\odot}$ and a helium content of $Y = 0.245$. This first-generation model does indeed spend most of its horizontal branch evolution at the redder end of the horizontal branch. The solid black line is a model with an initial mass of 0.75 $M_{\odot}$ and an enhanced helium content of Y = 0.285. This second-generation model spends its horizontal branch evolution in a bluer part of the horizontal branch, but still ascends the AGB, contrary to the observational findings. The solid blue line shows the evolution of the $Y = 0.285$ model with an ad hoc 20-fold increase in mass loss rate initiated once the star settles on the horizontal branch. This model evolves downwards along the extreme blue end of the horizontal branch and fails to ascend the AGB. The arrow indicates the location of the Grundahl jump at $y = 14.65$ (from Campbell et al. 2013).

to what is observed. In blue there is the stellar model track for which a mass loss during the HB phase increased by an *ad hoc* factor of 20 is expected. This model can populate the blue end of the HB and also fail to become an AGB star. Even if these are only hypothetical tests, these results could be a starting point to study this phenomenon.

It is clear that we already have not a real explanation for the AGB-manquè phenomenon, observed in some GCs. As future target, we plan to analyze star counts of RGB, HB, and AGB stars to further investigate the connection between multiple stellar populations and AGB-manquè objects.

# LIST OF FIGURES

# LIST OF TABLES

# BIBLIOGRAPHY


Anderson J., 1998, PhD thesis, , University of California, Berkeley, (1998)

Anderson J., Bedin L. R., Piotto G., Yadav R. S., Bellini A., 2006, A&A, 454, 1029

Anderson J. et al., 2008, AJ, 135, 2114

Bastian N., Cabrera-Ziri I., Salaris M., 2015, MNRAS, 449, 3333

Bastian N., Lamers H. J. G. L. M., de Mink S. E., Longmore S. N., Goodwin S. P., Gieles M., 2013, MNRAS, 436, 2398

Bedin L. R., King I. R., Anderson J., Piotto G., Salaris M., Cassisi S., Serenelli A., 2008, ApJ, 678, 1279

Bedin L. R., Piotto G., Anderson J., Cassisi S., King I. R., Momany Y., Carraro G., 2004, ApJ, 605, L125

Bedin L. R., Piotto G., King I. R., Anderson J., 2003, AJ, 126, 247

Bedin L. R., Piotto G., Zoccali M., Stetson P. B., Saviane I., Cassisi S., Bono G., 2000, A&A, 363, 159

Behr B. B., 2003, ApJS, 149, 67

Bekki K., 2011, MNRAS, 412, 2241

Bekki K., Norris J. E., 2006, ApJ, 637, L109

Bell R. A., Dickens R. J., Gustafsson B., 1979, ApJ, 229, 604

Bellini A., Anderson J., Salaris M., Cassisi S., Bedin L. R., Piotto G., Bergeron P., 2013a, ApJ, 769, L32

Bellini A., Bedin L. R., Piotto G., Milone A. P., Marino A. F., Villanova S., 2010, AJ, 140, 631

Bellini A. et al., 2009a, A&A, 493, 959

Bellini A., Piotto G., Bedin L. R., King I. R., Anderson J., Milone A. P., Momany Y., 2009b, A&A, 507, 1393

Bellini A. et al., 2013b, ApJ, 765, 32

Brown J. A., Wallerstein G., 1993, AJ, 106, 133

Brown J. A., Wallerstein G., Oke J. B., 1990, AJ, 100, 1561

Busso G. et al., 2007, A&A, 474, 105

Caloi V., D'Antona F., 2007, A&A, 463, 949

Campbell S. W. et al., 2013, Nature, 498, 198

Campbell S. W., Yong D., Wylie-de Boer E. C., Stancliffe R. J., Lattanzio J. C., Angelou G. C., Grundahl F., Sneden C., 2010, Mem. Soc. Astron. Italiana, 81, 1004

Carretta E., 2014, ApJ, 795, L28

Carretta E., Bragaglia A., Gratton R., D'Orazi V., Lucatello S., 2009a, A&A, 508, 695

Carretta E., Bragaglia A., Gratton R., Lucatello S., Bellazzini M., D'Orazi V., 2010a, ApJ, 712, L21

Carretta E., Bragaglia A., Gratton R. G., Leone F., Recio-Blanco A., Lucatello S., 2006, A&A, 450, 523

Carretta E. et al., 2010b, A&A, 520, A95

Carretta E. et al., 2009b, A&A, 505, 117

Carretta E., Bragaglia A., Gratton R. G., Lucatello S., D'Orazi V., 2012, ApJ, 750, L14

Carretta E., Bragaglia A., Gratton R. G., Lucatello S., Momany Y., 2007, A&A, 464, 927

Carretta E., Gratton R. G., 1997, A&AS, 121, 95

Carretta E., Gratton R. G., Bragaglia A., Bonifacio P., Pasquini L., 2004, A&A, 416, 925

Carretta E., Gratton R. G., Lucatello S., Bragaglia A., Bonifacio P., 2005, A&A, 433, 597

Cassisi S., Salaris M., Pietrinferni A., 2013, Mem. Soc. Astron. Italiana, 84, 91

Cassisi S., Salaris M., Pietrinferni A., Piotto G., Milone A. P., Bedin L. R., Anderson J., 2008, ApJ, 672, L115

Castelli F., 2005, Memorie della Societa Astronomica Italiana Supplementi, 8, 25

Cohen J. G., 1978, ApJ, 223, 487

Cottrell P. L., Da Costa G. S., 1981, ApJ, 245, L79

Da Costa G. S., Held E. V., Saviane I., 2014, MNRAS, 438, 3507

Da Costa G. S., Held E. V., Saviane I., Gullieuszik M., 2009, ApJ, 705, 1481

Dalessandro E., Salaris M., Ferraro F. R., Cassisi S., Lanzoni B., Rood R. T., Fusi Pecci F., Sabbi E., 2011, MNRAS, 410, 694

D'Antona F., Bellazzini M., Caloi V., Pecci F. F., Galleti S., Rood R. T., 2005, ApJ, 631, 868

D'Antona F., Caloi V., 2008, MNRAS, 390, 693

D'Antona F., Caloi V., Montalbán J., Ventura P., Gratton R., 2002, A&A, 395, 69

D'Antona F., Gratton R., Chieffi A., 1983, Mem. Soc. Astron. Italiana, 54, 173

D'Antona F., Ventura P., Decressin T., Vesperini E., D'Ercole A., 2014, MNRAS, 443, 3302

de Mink S. E., Pols O. R., Langer N., Izzard R. G., 2009, A&A, 507, L1

de Mink S. E., Pols O. R., Langer N., Izzard R. G., 2010, in IAU Symposium, Vol. 266, IAU Symposium, de Grijs R., Lépine J. R. D., eds., pp. 169–174

Decressin T., Baumgardt H., Charbonnel C., Kroupa P., 2010, A&A, 516, A73

Decressin T., Charbonnel C., Meynet G., 2007, A&A, 475, 859

Decressin T., Meynet G., Charbonnel C., Prantzos N., Ekström S., 2007, A&A, 464, 1029

Denissenkov P. A., Hartwick F. D. A., 2014, MNRAS, 437, L21

Denissenkov P. A., VandenBerg D. A., Hartwick F. D. A., Herwig F., Weiss A., Paxton B., 2015, MNRAS, 448, 3314

D'Ercole A., D'Antona F., Carini R., Vesperini E., Ventura P., 2012, MNRAS, 423, 1521

D'Ercole A., D'Antona F., Ventura P., Vesperini E., McMillan S. L. W., 2010, MNRAS, 407, 854

D'Ercole A., Vesperini E., D'Antona F., McMillan S. L. W., Recchi S., 2008, MNRAS, 391, 825

di Criscienzo M., D'Antona F., Ventura P., 2010, A&A, 511, A70

Dotter A., Chaboyer B., Jevremović D., Kostov V., Baron E., Ferguson J. W., 2008, ApJS, 178, 89

Drake J. J., Smith V. V., Suntzeff N. B., 1992, ApJ, 395, L95

Dupree A. K., Avrett E. H., 2013, ApJ, 773, L28

Dupree A. K., Strader J., Smith G. H., 2011, ApJ, 728, 155

Feltzing S., Primas F., Johnson R. A., 2009, A&A, 493, 913

Ferraro F. R. et al., 2009, Nature, 462, 483

Ferraro F. R., Possenti A., Lagani P., Sabbi E., D'Amico N., Rood R. T., 2003, in Astronomical Society of the Pacific Conference Series, Vol. 296, New Horizons in Globular Cluster Astronomy, Piotto G., Meylan G., Djorgovski S. G., Riello M., eds., pp. 143–5

Freudling W., Romaniello M., Patat F., Møller P., Jehin E., O'Brien K., 2007, in Astronomical Society of the Pacific Conference Series, Vol. 364, The Future of Photometric, Spectrophotometric and Polarimetric Standardization, Sterken C., ed., p. 113

Geisler D., Villanova S., Carraro G., Pilachowski C., Cummings J., Johnson C. I., Bresolin F., 2012, ApJ, 756, L40

Gratton R., Sneden C., Carretta E., 2004, ARA&A, 42, 385

Gratton R. G. et al., 2001, A&A, 369, 87

Gratton R. G., Carretta E., Bragaglia A., 2012, A&A Rev., 20, 50

Gratton R. G. et al., 2012, A&A, 539, A19

Gratton R. G., Lucatello S., Carretta E., Bragaglia A., D'Orazi V., Momany Y. A., 2011, A&A, 534, A123

Gratton R. G. et al., 2013, A&A, 549, A41

Gratton R. G., Quarta M. L., Ortolani S., 1986, A&A, 169, 208

Grundahl F., Briley M., Nissen P. E., Feltzing S., 2002, A&A, 385, L14

Grundahl F., Catelan M., Landsman W. B., Stetson P. B., Andersen M. I., 1999, ApJ, 524, 242

Han S.-I., Lee Y.-W., Joo S.-J., Sohn S. T., Yoon S.-J., Kim H.-S., Lee J.-W., 2009, ApJ, 707, L190

Harris W. E., 1996, AJ, 112, 1487

Ivans I. I., Sneden C., Kraft R. P., Suntzeff N. B., Smith V. V., Langer G. E., Fulbright J. P., 1999, AJ, 118, 1273

Johnson C. I., Pilachowski C. A., 2010, ApJ, 722, 1373

Joo S.-J., Lee Y.-W., 2013, ApJ, 762, 36

King I. R. et al., 2012, AJ, 144, 5

King I. R., Bedin L. R., Piotto G., Cassisi S., Anderson J., 2005, AJ, 130, 626

Kraft R. P., Sneden C., Langer G. E., Shetrone M. D., 1993, AJ, 106, 1490

Kravtsov V., Alcaíno G., Marconi G., Alvarado F., 2011, A&A, 527, L9

Kravtsov V., Alcaíno G., Marconi G., Alvarado F., 2014, ApJ, 783, 56

Kurucz R. L., 1993, SYNTHE spectrum synthesis programs and line data

Kurucz R. L., 2005, Memorie della Societa Astronomica Italiana Supplementi, 8, 14

Kurucz R. L., Avrett E. H., 1981, SAO Special Report, 391

Lee J.-W., Kang Y.-W., Lee J., Lee Y.-W., 2009a, Nature, 462, 480

Lee J.-W., Lee J., Kang Y.-W., Lee Y.-W., Han S.-I., Joo S.-J., Rey S.-C., Yong D., 2009b, ApJ, 695, L78

Lee Y.-W. et al., 2013, ApJ, 778, L13

Lee Y.-W., Joo J.-M., Sohn Y.-J., Rey S.-C., Lee H.-C., Walker A. R., 1999, Nature, 402, 55

Libralato M., Bellini A., Bedin L. R., Piotto G., Platais I., Kissler-Patig M., Milone A. P., 2014, A&A, 563, A80

Lim D., Han S.-I., Lee Y.-W., Roh D.-G., Sohn Y.-J., Chun S.-H., Lee J.-W., Johnson C. I., 2015, ApJS, 216, 19

Lind K., Charbonnel C., Decressin T., Primas F., Grundahl F., Asplund M., 2011, A&A, 527, A148

Maeder A., Meynet G., 2006, A&A, 448, L37

Marín-Franch A. et al., 2009, ApJ, 694, 1498

Marino A. F., Milone A. P., Lind K., 2013, ApJ, 768, 27

Marino A. F. et al., 2012a, ApJ, 746, 14

Marino A. F., Milone A. P., Piotto G., Villanova S., Bedin L. R., Bellini A., Renzini A., 2009, A&A, 505, 1099

Marino A. F. et al., 2011a, ApJ, 731, 64

Marino A. F. et al., 2014a, MNRAS, 437, 1609

Marino A. F. et al., 2012b, A&A, 541, A15

Marino A. F. et al., 2014b, MNRAS, 442, 3044

Marino A. F. et al., 2011b, A&A, 532, A8

Marino A. F., Villanova S., Milone A. P., Piotto G., Lind K., Geisler D., Stetson P. B., 2011c, ApJ, 730, L16

Marino A. F., Villanova S., Piotto G., Milone A. P., Momany Y., Bedin L. R., Medling A. M., 2008, A&A, 490, 625

Marks M., Kroupa P., 2010, MNRAS, 406, 2000

Milone A. P., Bedin L. R., Piotto G., Anderson J., 2009a, A&A, 497, 755

Milone A. P. et al., 2008, ApJ, 673, 241

Milone A. P. et al., 2014a, MNRAS, 439, 1588

Milone A. P. et al., 2014b, ApJ, 785, 21

Milone A. P. et al., 2013, ApJ, 767, 120

Milone A. P., Marino A. F., Piotto G., Bedin L. R., Anderson J., Aparicio A., Cassisi S., Rich R. M., 2012a, ApJ, 745, 27

Milone A. P. et al., 2015, MNRAS, 447, 927 (Paper II)

Milone A. P. et al., 2012b, A&A, 540, A16

Milone A. P., Piotto G., Bedin L. R., Cassisi S., Anderson J., Marino A. F., Pietrinferni A., Aparicio A., 2012c, A&A, 537, A77

Milone A. P. et al., 2012d, ApJ, 744, 58

Milone A. P. et al., 2010, ApJ, 709, 1183

Milone A. P., Stetson P. B., Piotto G., Bedin L. R., Anderson J., Cassisi S., Salaris M., 2009b, A&A, 503, 755

Milone A. P., Villanova S., Bedin L. R., Piotto G., Carraro G., Anderson J., King I. R., Zaggia S., 2006, A&A, 456, 517

Miocchi P. et al., 2013, ApJ, 774, 151

Monelli M. et al., 2013, MNRAS, 431, 2126

Mucciarelli A., Lovisi L., Lanzoni B., Ferraro F. R., 2014, ApJ, 786, 14

Nardiello D., Milone A. P., Piotto G., Marino A. F., Bellini A., Cassisi S., 2015a, A&A, 573, A70

Nardiello D. et al., 2015b, MNRAS, 451, 4831

Norris J., 1981, ApJ, 248, 177

Norris J., Cottrell P. L., Freeman K. C., Da Costa G. S., 1981, ApJ, 244, 205

Norris J. E., Da Costa G. S., 1995, ApJ, 441, L81

Osborn W., 1971, The Observatory, 91, 223

Pancino E., Rejkuba M., Zoccali M., Carrera R., 2010, A&A, 524, A44

Pasquini L., Mauas P., Käufl H. U., Cacciari C., 2011, A&A, 531, A35

Pietrinferni A., Cassisi S., Salaris M., Castelli F., 2004, ApJ, 612, 168

Pietrinferni A., Cassisi S., Salaris M., Percival S., Ferguson J. W., 2009, ApJ, 697, 275

Piotto G. et al., 2007, ApJ, 661, L53

Piotto G. et al., 2012, ApJ, 760, 39

Piotto G. et al., 2015, AJ, 149, 91 (Paper I)

Piotto G., Milone A. P., Marino A. F., Bedin L. R., Anderson J., Jerjen H., Bellini A., Cassisi S., 2013, ApJ, 775, 15

Piotto G. et al., 2005, ApJ, 621, 777

Prantzos N., Charbonnel C., 2006, A&A, 458, 135

Prantzos N., Charbonnel C., Iliadis C., 2007, A&A, 470, 179

Ramírez S. V., Cohen J. G., 2002, AJ, 123, 3277

Renzini A., 2013, Mem. Soc. Astron. Italiana, 84, 162

Renzini A., Buzzoni A., 1986, in Astrophysics and Space Science Library, Vol. 122, Spectral Evolution of Galaxies, Chiosi C., Renzini A., eds., pp. 195–231

Richer H. B. et al., 2008, AJ, 135, 2141

Roh D.-G., Lee Y.-W., Joo S.-J., Han S.-I., Sohn Y.-J., Lee J.-W., 2011, ApJ, 733, L45

Salaris M., Cassisi S., 2014, A&A, 566, A109

Sandage A., Wildey R., 1967, ApJ, 150, 469

Sarajedini A. et al., 2007, AJ, 133, 1658

Sbordone L., Bonifacio P., Castelli F., 2007, in IAU Symposium, Vol. 239, IAU Symposium, Kupka F., Roxburgh I., Chan K. L., eds., pp. 71–73

Sbordone L., Bonifacio P., Castelli F., Kurucz R. L., 2004, Memorie della Societa Astronomica Italiana Supplementi, 5, 93

Sbordone L., Salaris M., Weiss A., Cassisi S., 2011, A&A, 534, A9

Shen Z.-X., Bonifacio P., Pasquini L., Zaggia S., 2010, A&A, 524, L2

Silverman B. W., 1986, Density estimation for statistics and data analysis

Smith G. H., Briley M. M., 2005, PASP, 117, 895

Smith G. H., Norris J., 1982, ApJ, 254, 149

Sollima A., Ferraro F. R., Bellazzini M., Origlia L., Straniero O., Pancino E., 2007, ApJ, 654, 915

Sollima A., Ferraro F. R., Pancino E., Bellazzini M., 2008, Mem. Soc. Astron. Italiana, 79, 342

Sollima A., Pancino E., Ferraro F. R., Bellazzini M., Straniero O., Pasquini L., 2005, ApJ, 634, 332

Sosin C. et al., 1997, ApJ, 480, L35

Stetson P. B., 2000, PASP, 112, 925

Sweigart A. V., Mengel J. G., 1979, ApJ, 229, 624

Valcarce A. A. R., Catelan M., Alonso-García J., Cortés C., De Medeiros J. R., 2014, ApJ, 782, 85

van den Bergh S., 1967, AJ, 72, 70

van der Marel R. P., Anderson J., 2010, ApJ, 710, 1063

Vanbeveren D., Mennekens N., De Greve J. P., 2012, A&A, 543, A4

Ventura P., Caloi V., D'Antona F., Ferguson J., Milone A., Piotto G. P., 2009, MNRAS, 399, 934

Vesperini E., McMillan S. L. W., D'Antona F., D'Ercole A., 2013, MNRAS, 429, 1913

Villanova S., Geisler D., Carraro G., Moni Bidin C., Muñoz C., 2013, ApJ, 778, 186

Villanova S., Geisler D., Gratton R. G., Cassisi S., 2014, ApJ, 791, 107

Villanova S., Geisler D., Piotto G., 2010, ApJ, 722, L18

Villanova S., Geisler D., Piotto G., Gratton R. G., 2012, ApJ, 748, 62

Villanova S., Piotto G., Gratton R. G., 2009, A&A, 499, 755

Villanova S. et al., 2007, ApJ, 663, 296

Walker A. R. et al., 2011, MNRAS, 415, 643

Wallerstein G., Myckky-Leep E., Oke J. B., 1987, AJ, 94, 523

Yong D., Grundahl F., 2008, ApJ, 672, L29

Yong D., Grundahl F., Johnson J. A., Asplund M., 2008, ApJ, 684, 1159

Yong D., Grundahl F., Lambert D. L., Nissen P. E., Shetrone M. D., 2003, A&A, 402, 985

Yong D., Grundahl F., Nissen P. E., Jensen H. R., Lambert D. L., 2005, A&A, 438, 875

Yong D., Grundahl F., Norris J. E., 2015, MNRAS, 446, 3319

Yong D. et al., 2013, MNRAS, 434, 3542

Yong D. et al., 2014, MNRAS, 441, 3396